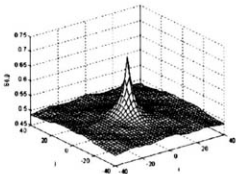


Asphalt Concrete

Simulation, Modeling, and
Experimental Characterization



Edited by

Eyad Masad
Vassilis P. Panoskaltsis
Linbing Wang

ASCE

**GEO
INSTITUTE**
of the American Society of Civil Engineers

GEOTECHNICAL SPECIAL PUBLICATION NO. 146

ASPHALT CONCRETE

SIMULATION, MODELING, AND EXPERIMENTAL CHARACTERIZATION

PROCEEDINGS OF THE R. LYTTON SYMPOSIUM ON
MECHANICS OF FLEXIBLE PAVEMENTS

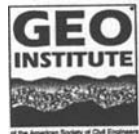
June 1-3, 2005
Baton Rouge, Louisiana

SPONSORED BY
Pavements Committee of The Geo-Institute of the
American Society of Civil Engineers

Inelastic Committee of the Engineering Mechanics Division of the
American Society of Civil Engineers

EDITED BY
Eyad Masad
Vassilis P. Panoskaltzis
Linbing Wang

ASCE



Published by the American Society of Civil Engineers

Cataloging-in-Publication Data on file with the Library of Congress.

American Society of Civil Engineers
1801 Alexander Bell Drive
Reston, Virginia, 20191-4400

www.pubs.asce.org

Any statements expressed in these materials are those of the individual authors and do not necessarily represent the views of ASCE, which takes no responsibility for any statement made herein. No reference made in this publication to any specific method, product, process, or service constitutes or implies an endorsement, recommendation, or warranty thereof by ASCE. The materials are for general information only and do not represent a standard of ASCE, nor are they intended as a reference in purchase specifications, contracts, regulations, statutes, or any other legal document. ASCE makes no representation or warranty of any kind, whether express or implied, concerning the accuracy, completeness, suitability, or utility of any information, apparatus, product, or process discussed in this publication, and assumes no liability therefore. This information should not be used without first securing competent advice with respect to its suitability for any general or specific application. Anyone utilizing this information assumes all liability arising from such use, including but not limited to infringement of any patent or patents.

ASCE and American Society of Civil Engineers—Registered in U.S. Patent and Trademark Office.

Photocopies: Authorization to photocopy material for internal or personal use under circumstances not falling within the fair use provisions of the Copyright Act is granted by ASCE to libraries and other users registered with the Copyright Clearance Center (CCC) Transactional Reporting Service, provided that the base fee of \$25.00 per article is paid directly to CCC, 222 Rosewood Drive, Danvers, MA 01923. The identification for this book is 0-7844-0825-4/06/ \$25.00. Requests for special permission or bulk copying should be addressed to Permissions & Copyright Dept., ASCE.

Copyright © 2006 by the American Society of Civil Engineers.
All Rights Reserved.
ISBN 0-7844-0825-4
Manufactured in the United States of America.

Geotechnical Special Publications

- 1 *Terzaghi Lectures*
- 2 *Geotechnical Aspects of Stiff and Hard Clays*
- 3 *Landslide Dams: Processes, Risk, and Mitigation*
- 7 *Timber Bulkheads*
- 9 *Foundations & Excavations in Decomposed Rock of the Piedmont Province*
- 11 *Dynamic Response of Pile Foundations – Experiment, Analysis and Observation*
- 14 *Geotechnical Aspects of Karst Terrains*
- 15 *Measured Performance Shallow Foundations*
- 16 *Special Topics in Foundations*
- 17 *Soil Properties Evaluation from Centrifugal Models*
- 18 *Geosynthetics for Soil Improvement*
- 19 *Mine Induced Subsidence: Effects on Engineered Structures*
- 21 *Hydraulic Fill Structures*
- 22 *Foundation Engineering*
- 23 *Predicted and Observed Axial Behavior of Piles*
- 24 *Resilient Moduli of Soils: Laboratory Conditions*
- 25 *Design and Performance of Earth Retaining Structures*
- 27 *Geotechnical Engineering Congress*
- 28 *Detection of and Construction at the Soil/Rock Interface*
- 29 *Recent Advances in Instrumentation, Data Acquisition and Testing in Soil Dynamics*
- 32 *Embankment of Dams – James L. Sherard Contributions*
- 33 *Excavation and Support for the Urban Infrastructure*
- 34 *Piles Under Dynamic Loads*
- 35 *Geotechnical Practice in Dam Rehabilitation*
- 37 *Advances in Site Characterization: Data Acquisition, Data Management and Data Interpretation*
- 39 *Unsaturated Soils*
- 40 *Vertical and Horizontal Deformations of Foundations and Embankments*
- 41 *Predicted and Measured Behavior of Five Spread Footings on Sand*
- 42 *Serviceability of Earth Retaining Structures*
- 43 *Fracture Mechanics Applied to Geotechnical Engineering*
- 44 *Ground Failures Under Seismic Conditions*
- 45 *In Situ Deep Soil Improvement*
- 46 *Geo-environment 2000*
- 47 *Geo-Environmental Issues Facing the Americas*
- 48 *Soil Suction Applications in Geotechnical Engineering*
- 49 *Soil Improvement for Earthquake Hazard Mitigation*
- 50 *Foundation Upgrading and Repair for Infrastructure Improvement*
- 51 *Performance of Deep Foundations Under Seismic Loading*
- 52 *Landslides Under Static and Dynamic Conditions – Analysis, Monitoring, and Mitigation*
- 53 *Landfill Closures – Environmental Protection and Land Recovery*
- 54 *Earthquake Design and Performance of Solid Waste Landfills*
- 55 *Earthquake-Induced Movements and Seismic Remediation of Existing Foundations and Abutments*
- 56 *Static and Dynamic Properties of Gravelly Soils*
- 57 *Verification of Geotechnical Grouting*
- 58 *Uncertainty in the Geologic Environment*
- 59 *Engineered Contaminated Soils and Interaction of Soil Geomembranes*
- 60 *Analysis and Design of Retaining Structures Against Earthquakes*
- 61 *Measuring and Modeling Time Dependent Soil Behavior*
- 62 *Case Histories of Geophysics Applied to Civil Engineering and Public Policy*
- 63 *Design with Residual Materials: Geotechnical and Construction Considerations*
- 64 *Observation and Modeling in Numerical Analysis and Model Tests in Dynamic Soil-Structure Interaction Problems*
- 65 *Dredging and Management of Dredged Material*
- 66 *Grouting: Compaction, Remediation and Testing*
- 67 *Spatial Analysis in Soil Dynamics and Earthquake Engineering*
- 68 *Unsaturated Soil Engineering Practice*
- 69 *Ground Improvement, Ground Reinforcement, Ground Treatment: Developments 1987-1997*
- 70 *Seismic Analysis and Design for Soil-Pile-Structure Interactions*
- 71 *In Situ Remediation of the Geo-environment*
- 72 *Degradation of Natural Building Stone*
- 73 *Innovative Design and Construction for Foundations and Substructures Subject to Freezing and Frost*

- 74 *Guidelines of Engineering Practice for Braced and Tied-Back Excavations*
- 75 *Geotechnical Earthquake Engineering and Soil Dynamics III*
- 76 *Geosynthetics in Foundation Reinforcement and Erosion Control Systems*
- 77 *Stability of Natural Slopes in the Coastal Plain*
- 78 *Filtration and Drainage in Geotechnical/Geoenvironmental Engineering*
- 79 *Recycled Materials in Geotechnical Applications*
- 80 *Grouts and Grouting: A Potpourri of Projects*
- 81 *Soil Improvement for Big Digs*
- 82 *Risk-Based Corrective Action and Brownfields Restorations*
- 83 *Design and Construction of Earth Retaining Systems*
- 84 *Effects of Construction on Structures*
- 85 *Application of Geotechnical Principles in Pavement Engineering*
- 86 *Big Digs Around the World*
- 87 *Jacked Tunnel Design and Construction*
- 88 *Analysis, Design, Construction, and Testing of Deep Foundations*
- 89 *Recent Advances in the Characterization of Transportation Geo-Materials*
- 90 *Geo-Engineering for Underground Facilities*
- 91 *Special Geotechnical Testing: Central Artery/Tunnel Project in Boston, Massachusetts*
- 94 *Performance Confirmation of Constructed Geotechnical Facilities*
- 95 *Soil-Cement and Other Construction Practices in Geotechnical Engineering*
- 96 *Numerical Methods in Geotechnical Engineering: Recent Developments*
- 97 *Innovations and Applications in Geotechnical Site Characterization*
- 98 *Pavement Subgrade, Unbound Materials, and Nondestructive Testing*
- 99 *Advances in Unsaturated Geotechnics*
- 100 *New Technological and Design Developments in Deep Foundations*
- 101 *Slope Stability 2000*
- 102 *Trends in Rock Mechanics*
- 103 *Advances in Transportation and Geoenvironmental Systems Using Geosynthetics*
- 104 *Advances in Grouting and Ground Modification*
- 105 *Environmental Geotechnics*
- 106 *Geotechnical Measurements: Lab & Field*
- 107 *Soil Dynamics and Liquefaction 2000*
- 108 *Use of Geophysical Methods in Construction*
- 109 *Educational Issues in Geotechnical Engineering*
- 110 *Computer Simulation of Earthquake Effects*
- 111 *Judgment and Innovation: The Heritage and Future of the Geotechnical Engineering Profession*
- 112 *Soft Ground Technology*
- 114 *Soils Magic*
- 115 *Expansive Clay Soils and Vegetative Influence on Shallow Foundations*
- 116 *Deep Foundations 2002: An International Perspective on Theory, Design, Construction, and Performance*
- 117 *Discrete Element Methods: Numerical Modeling of Discontinua*
- 118 *A History of Progress: Selected U.S. Papers in Geotechnical Engineering*
- 119 *Soil Behavior and Soft Ground Construction*
- 120 *Grouting and Ground Treatment*
- 121 *Probabilistic Site Characterization at the National Geotechnical Experimentation Sites*
- 122 *Sinkholes and the Engineering and Environmental Impacts of Karst*
- 123 *Recent Advances in Materials Characterization and Modeling of Pavement Systems*
- 124 *GeoSupport 2004: Drilled Shafts, Micropiling, Deep Mixing, Remedial and Specialty Foundation Systems*
- 125 *Current Practices and Future Trends in Deep Foundations*
- 126 *Geotechnical Engineering for Transportation Projects*
- 127 *Recycled Materials in Geotechnics*
- 128 *Soil Constitutive Models: Evaluation, Selection, and Calibration*
- 129 *Advances in Designing and Testing Deep Foundations*
- 130 *Advances in Pavement Engineering*
- 131 *Contemporary Issues in Foundation Engineering*
- 132 *Advances in Deep Foundations: In Memory of Michael W. O'Neill*
- 133 *Earthquake Engineering and Soil Dynamics*
- 134 *Soil Dynamics Symposium in Honor of Professor Richard D. Woods*
- 135 *Erosion of Soils and Scour of Foundations*
- 136 *Innovations in Grouting and Soil Improvement*

- 137 *Legal and Liability Issues in Geotechnical Engineering***
- 138 *Site Characterization and Modeling***
- 139 *Calibration of Constitutive Models***
- 140 *Slopes and Retaining Structures Under Seismic and Static Conditions***
- 141 *International Perspectives on Soil Reinforcement Applications***
- 142 *Waste Containment and Remediation***
- 143 *Geomechanics: Testing, Modeling, and Simulation***
- 144 *Sinkholes and the Engineering and Environmental Impacts of Karst***
- 145 *Seismic Performance and Simulation of Pile Foundations in Liquefied and Laterally Spreading Ground***

This page intentionally left blank

Preface

This special publication includes papers on simulation, modeling and experimental characterization of asphalt concrete. A number of papers report on micromechanical finite element analysis of asphalt concrete with the purpose of establishing the linkage between the properties of asphalt concrete constituents, microstructure distribution and macroscopic properties and response. In these micromechanical models, asphalt concrete constituents are modeled using elastic, viscoelastic, and/or plastic properties. Also, the discrete element method was used to analyze the micromechanical behavior of asphalt concrete under different loading conditions. A number of papers report on the development and numerical implementation of elasto-visco-plastic constitutive models that address the cyclic response, anisotropic behavior, and permanent deformation of asphalt concrete. Finite element results are also presented in these papers to demonstrate the efficacy of the models in predicting permanent deformation in asphalt pavements. Fatigue behavior of asphalt concrete is addressed in this special publication through the development of a calibrated mechanistic approach that includes the effect of aging. This approach was used to analyze the fatigue life of different asphalt concrete mixtures. On a closely related subject, three papers focus on the mathematical representation of viscoelastic properties of asphalt concrete at a wide range of temperatures and frequencies, and on experimental characterization of healing. Characterization of moisture damage is addressed in this volume through the development of a test protocol that accounts for the interaction of repeated loading with moisture. One of the papers deals with the sensitivity of low temperature cracking models to changes in the coefficient of thermal contraction. Finally, the last paper models the response of asphalt pavements to a slow moving truck while taken into consideration the time-dependent behavior of asphalt concrete, and the non-uniform stress distribution at the tire-pavement interface.

Each paper published in this ASCE Geotechnical Special Publication (GSP) was evaluated by peer reviewers and the editors. The papers that received at least one positive review were sent to the authors to address the review comments. The authors of the papers published here addressed all of the reviewers' comments to the satisfaction of the editors. The ASCE Geo-Institute Pavements Committee acknowledges with appreciation the reviewers' dedication and contribution of their time and effort.

The papers found in this special publication were presented during the two-day R. Lytton Symposium on Mechanics of Flexible Pavements, which was organized as part of the 2005 Joint ASME/ASCE/SES Conference on Mechanics and Materials in Baton Rouge-Louisiana on June 1-3, 2005. The symposium was sponsored by the Inelastic Committee of the Engineering Mechanics Division of ASCE and the

Pavements Committee of the ASCE Geo-Institute. Dr. Robert L. Lytton gave the symposium opening address on the role of mechanics in reducing variability in material characterization and performance prediction. The presentation of Dr. Lytton was followed by a discussion among the symposium participants on the applications of mechanics principles in asphalt pavements.

The editors of this volume would like to thank the Board of Governors of the Geo-Institute for their approval of the symposium and this special publication.

Eyad Masad, Texas A&M University
Vassilis P. Panoskaltsis, Case Western Reserve University
Linbing Wang, Virginia Tech
August 10, 2005

Contents

Micromechanical Simulation of Asphaltic Materials Using the Discrete Element Method	1
A. R. Abbas, A. T. Papagiannakis, and E. A. Masad	
A Micromechanical Viscoelasto-Plastic Model for Asphalt Mixture	12
Qingli Dai, Zhanping You, and Martin H. Sadd	
Development and Implementation of a Finite Element Model for Asphalt Mixture to Predict Compressive Complex Moduli at Low and Intermediate Temperatures	21
Zhanping You, Qingli Dai, and Bardan Gurung	
An Evaluation of the Stress Non-Uniformity due to the Heterogeneity of AC in the Indirect Tensile Test	29
Bing Zhang, Linbing Wang, and Mehmet T. Tumay	
The Development of a Microstructural-Based Continuum Model for Hot Mix Asphalt	44
Samer H. Dessouky and Eyad A. Masad	
Development of a Computational Model for Asphaltic Concrete Response under Cyclic Loading	53
Edwin Swart, Tom Scarpas, and Xueyan Liu	
Numerical Implementation of a Hyperelastic-Viscoplastic Damage Model for Asphalt Concrete Materials and Pavements	61
Dinesh Panneerselvam and Vassilis P. Panoskaltzis	
The Huet-Sayegh Model: A Simple and Excellent Rheological Model for Master Curves of Asphaltic Mixes	73
Adriaan C. Pronk	
Partial Healing: A New Approach for the Damage Process during Fatigue Testing of Asphalt Specimen	83
Adriaan C. Pronk	
Laboratory Investigation on Healing of Sand Asphalt Mixtures	95
Venkaiah Chowdary, J. Murali Krishnan, and V. R. Rengaraju	
Fatigue Characterization of HMAC Mixtures Using Mechanistic Empirical and Calibrated Mechanistic Approaches Including the Effects of Aging	103
Lubinda F. Walubita, Amy Epps Martin, Charles Glover, Sung Hoon Jung, Gregory Cleveland, and Robert L. Lytton	
A Case Study: Assessing the Sensitivity of the Coefficient of Thermal Contraction of AC Mixtures on Thermal Crack Prediction	115
Hao Yin, Ghassan R. Chehab, and Shelley M. Stoffels	
Evaluation of Moisture Sensitivity of Hot Mix Asphalt by Flexural Beam Fatigue Test	124
Qing Lu and John T. Harvey	

Response of an Asphalt Pavement Mixture under a Slow Moving Truck.....	134
Elie Y. Hajj, Peter E. Sebaaly, and Raj V. Siddharthan	
Subject Index.....	147
Author Index	149

MICROMECHANICAL SIMULATION OF ASPHALTIC MATERIALS USING THE DISCRETE ELEMENT METHOD

A.R.Abbas¹, Geo-Institute Member, A.T.Papagiannakis², Geo-Institute Member,
E.A.Masad³, Geo-Institute Member

ABSTRACT

This paper summarizes the findings of modeling the micromechanical behavior of asphalt mastics and asphalt mixtures under various loading conditions. A commercial discrete element code called *Particle Flow Code in 2-Dimensions* (PFC2D) is used for this purpose.

Asphalt mastics are simulated using an assembly of stiff particles randomly dispersed in a medium of soft particles, representing the aggregate fillers and the asphalt binder, respectively. The stiffening effect of the aggregate fillers on the micromechanical behavior of asphalt mastics is investigated at different filler volume fractions. These results are compared to Dynamic Shear Rheometer (DSR) measurements on actual mastics. These mastic models are used to simulate the micromechanical behavior of hot mix asphalt (HMA) concretes. The behavior of these HMA models was investigated at high and low temperatures under loading conditions similar to those applied in the Simple Performance Test (SPT) and the Indirect Tension Test (IDT), respectively.

KEYWORDS: asphalt, mastic, mixture, simulation, discrete element, simple performance test, indirect tension test.

1. INTRODUCTION-OBJECTIVE

This paper describes a novel approach for modeling the micromechanical behavior of asphalt mastics and hot mix asphalt (HMA) concretes. Asphalt mastics are defined as dispersions of aggregate fillers within a medium of asphalt binder, while asphalt mixtures are defined as composites of aggregate particles of various sizes combined with asphalt mastics and air voids. The discrete element method (DEM) is used in simulating the stress-strain behavior of these composites. A commercial DEM code called *Particle Flow Code in 2-Dimensions* (PFC2D) is used for this purpose. The formulation of this approach is given in detail by Abbas (2004). The objective of this paper is to present some of the results of this analysis in addressing two issues, namely the effect of fillers in stiffening mastics and the effect of binder type on the

¹Highway Research Engineer, Turner-Fairbank Highway Research Center, Pavement Materials & Construction Team, McLean VA 22101 ala.abbas@fhwa.dot.gov

²Prof. Dept. of Civil & Enviro. Eng., Washington State University, Pullman WA 99164 pappa@wsu.edu

³Assoc. Prof. Dept. of Civil Eng., Texas A&M University, College Station TX 77843 emasad@civil.tamu.edu

viscoelastic and tensile properties of HMAs. The mastic simulation results were compared to Dynamic Shear Rheometer (DSR) measurements. On the other hand, the viscoelastic response of these HMA models at high temperatures and their tensile properties at low temperatures were investigated under loading conditions similar to those applied in the Simple Performance Test (SPT) and the Indirect Tension Test (IDT), respectively.

2. MODELING ASPHALT MASTICS

The stiffening effect of the aggregate fillers on the macromechanical behavior of asphalt mastics is studied through the generation of discrete element models that contain different filler volume fractions. The temperature dependency of the asphalt binder is included in the analysis through the modification of the stiffness of the soft particles. The numerical results are compared to experimental measurements on mastics using different fine aggregate-binder combinations and filler volume fractions.

2.1 Experimental Data

Three asphalt binders, (referred to as ABD-1, AAM-1, and ABM-1) and four aggregates (glacial gravel, granite, limestone, and greywacke, referred to as RF, RA, RD, and RH, respectively) were used in this study. Binders and aggregates were obtained from the Strategic Highway Research Program (SHRP) materials reference library (MRL). Aggregates were ground and the material passing sieve No. 200 was used as a mineral filler. Asphalt mastic specimens were fabricated by mixing each binder type with each of the four mineral fillers, resulting in twelve asphalt-filler combinations. The amount of fillers, to be added to the binder, was controlled in order to attain nine filler to binder concentration ratios, namely 0%, 6%, 11%, 17%, 21%, 25%, 27%, 29%, and 31%. To produce representative specimens, the asphalt binder, in its unaged state, and the mineral fillers were both heated to a temperature of 165°C, followed by mixing and stirring as the blend cooled down. The resulting asphalt mastic was then poured into silicone rubber molds to make pellets for testing in the dynamic shear rheometer (DSR). Strain sweep data was obtained using a *Rheometrics RDA II* DSR at a temperature of 25°C using plates of 8mm diameter. All tests were performed within the linear viscoelastic range. Interested readers are referred to references (Shashidhar et al. 1999; Shashidhar and Shenoy 2002) for more information on the specimen fabrication and testing.

2.2 Simulation of Asphalt Mastics

Asphalt mastics were simulated using a combination of stiff and soft particles, representing the aggregate fillers and the asphalt binder, respectively. The rationale for using discrete particles to simulate asphalt binder follows from the concepts of the DEM, whereby a continuum is discretized and the deformational behavior of the

assembly is characterized through the continuous update of the particles' locations and contact forces.

The model geometry of the asphalt mastics was input in PFC2D using an arrangement of in-plane circular particles generated using a built-in random particle-generation algorithm. Each particle was defined by a unique identification number, the Cartesian coordinates of the center, a radius, and a thickness (i.e., 3-D cylinders of unit thickness). As shown in Figure 1, a total of about 7800 cylindrical particles, measuring $100\mu\text{m}$ in diameter and a thickness of unity, were randomly generated within four walls separated by a horizontal distance of 6mm and a vertical distance of 12mm. A height/diameter ratio greater than or equal to 2 was selected in the analysis to minimize the boundary effects on the model predictions. In addition, the particle size (i.e., $100\mu\text{m}$) was varied until no significant differences in predictions were noticed. The selection of such particle size was also suggested by the need to conduct the analysis in a reasonable length of time, (i.e., within three to four hours). The analysis was repeated at different filler volume fractions ranging from 0 to 52% by using appropriate proportions of binder and filler particles. The target filler volume fraction was calculated by dividing the filler volume by the total volume (i.e., binder, fillers, and voids). Care was taken to ensure the randomness of the filler phase within the assembly in these simulations.

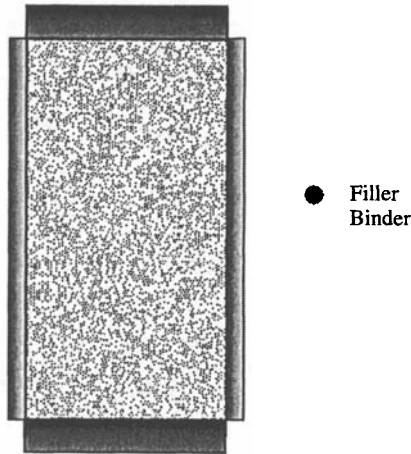


FIG. 1. Example of a DEM Mastic Model Consisting of 52% Fillers by Volume

Interaction among the particles was simulated using the linear contact model. This model is defined using two parameters, namely the normal and shear stiffness parameter. For each contact, an effective normal and shear contact stiffness is calculated from the particles' stiffnesses assuming that they act in series,

$$K^n = \frac{K_n^{(1)}K_n^{(2)}}{K_n^{(1)} + K_n^{(2)}} \quad (1)$$

$$K^s = \frac{K_s^{(1)}K_s^{(2)}}{K_s^{(1)} + K_s^{(2)}} \quad (2)$$

where,

K^n and K^s = effective normal and shear contact stiffnesses, respectively,

$K_n^{(1)}$ and $K_n^{(2)}$ = normal stiffnesses of particles 1 and 2, respectively, and

$K_s^{(1)}$ and $K_s^{(2)}$ = shear stiffnesses of particles 1 and 2, respectively.

Contact bonds, defined by normal and shear strength constants, were also used between the particles. These values serve as threshold for contact breakage, (i.e., the contact breaks where the magnitude of the tensile or shear force exceeds the respective strength parameters defined for that contact). Since the analysis in this part of the study was limited to linear response, where no contact breakage was expected, very high contact bonds were included between the model particles. The reader is referred to (Abbas et al. 2005) for more information about the contact stiffness and contact bond models.

Finally, loading was accomplished in two stages, namely the compaction stage and the loading stage. In the compaction stage, all four walls were controlled using a numerical “servo-control” mechanism, whereby the location of these walls was updated within each calculation cycle enough to maintain a target confining stress level of 0.1MPa. This step was necessary to ensure an initial uniform stress-state. In the loading stage, the same level of confinement was applied through the side walls, while the upper and lower walls were freed from the servo-control mechanism. Loading was achieved by vertically displacing the upper and lower platens inward. Horizontal and vertical stresses were calculated by dividing the average reaction forces on the side walls and the upper and lower walls, respectively, by the area of the corresponding pair of walls. The deviatoric stress was calculated as the difference between the vertical and the horizontal stress. Axial strain was calculated by dividing the change in the model height by its initial height at the beginning of the loading stage. The elastic modulus of the mastic was calculated by dividing the deviatoric stress by the axial strain. The corresponding shear modulus was calculated by dividing the normal modulus by $2(1+\nu)$, where ν is an assumed Poisson’s ratio of 0.45 for the composite. Figures 2 through 4 present the quality of fit of the model predictions to the viscoelastic mastic measurements. As can be noticed in these figures, the mastic/binder stiffness ratio is dependent on the binder stiffness. A gradual increase in the stiffness ratio is attained at low filler volume fractions followed by a sudden increase at high filler concentrations.

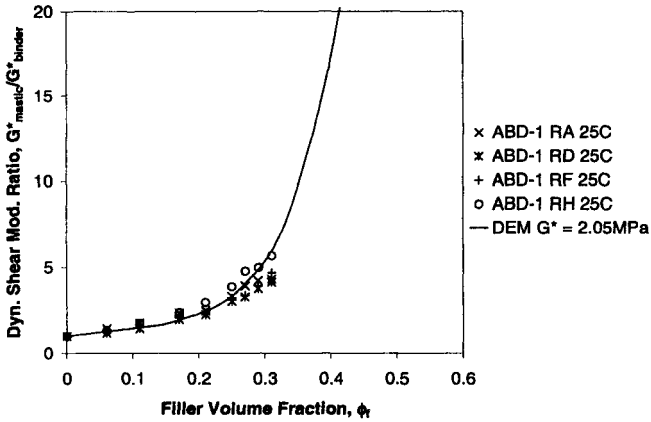


FIG. 2. Mastic to Binder Stiffness Ratios ($G^*_{mastic}/G^*_{binder}$) Measured Using the DSR and Predicted Using the DEM; Unaged ABD-1 Binder and Four Aggregate Fillers

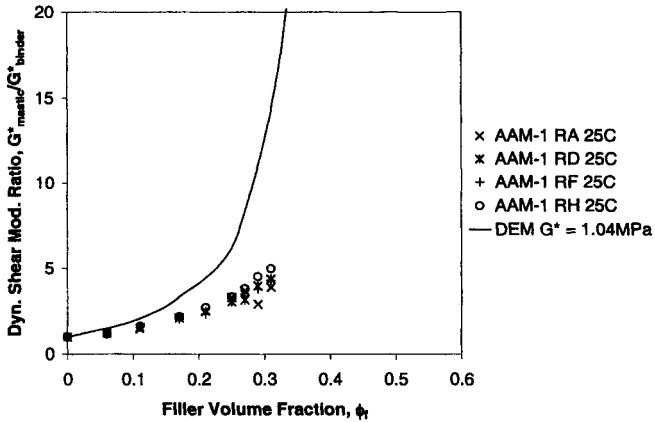


FIG. 3. Mastic to Binder Stiffness Ratios ($G^*_{mastic}/G^*_{binder}$) Measured Using the DSR and Predicted Using the DEM; Unaged AAM-1 Binder and Four Aggregate Fillers

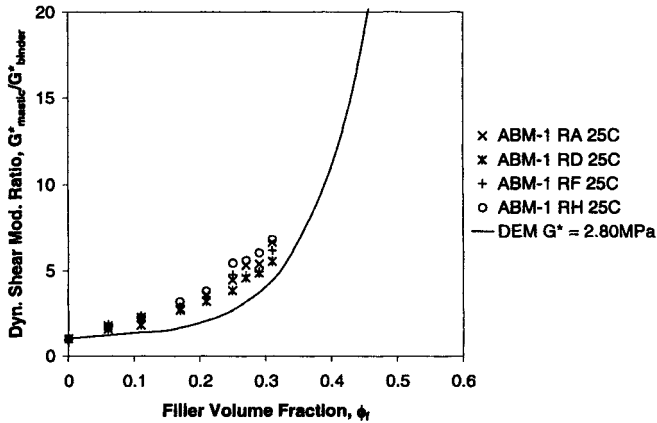


FIG. 4. Mastic to Binder Stiffness Ratios ($G^*_{mastic}/G^*_{binder}$) Measured Using the DSR and Predicted Using the DEM; Unaged ABM-1 Binder and Four Aggregate Fillers

3. MODELING ASPHALT MIXTURES

The viscoelastic response and the fracture mechanism of asphalt mixtures are investigated at high and low pavement service temperatures, respectively. At high temperatures, discrete element models are analyzed under dynamic loading conditions similar to those applied in the simple performance test (SPT). Aggregates are assumed to be rigid and the viscoelastic interaction among the mix constituents is described using the Burger model. The DEM results are compared to experimental measurements of viscoelastic properties on materials of one aggregate gradation using aggregates from the same source and nine different binders. At low temperatures, the indirect tension test (IDT) is simulated and the effect of the asphalt binder film thickness on the tensile strength and the failure strain is examined. Three types of bonds are incorporated in the HMA model describing the cohesion within the asphalt binder, the cohesion within the aggregate particle, and the adhesion between the aggregate and the binder.

3.1 Viscoelastic Behavior of HMA Concretes at High Temperatures

The analysis of the mastic behavior described above suggests that fillers result in mastic stiffnesses significantly higher than binder stiffnesses. This finding was incorporated into the models of the HMA behavior. The asphalt mastic was modeled in the pursuing analysis using a viscoelastic model, the Burger model, fitted to experimental binder data multiplied by a factor of 30. This was rationalized based on the combined effect of the presence of fines in the binder, the thickness of the binder film in the images investigated, and analyzing a 3-D problem through a 2-D model,

(i.e., ignoring aggregate particle interlock in the third dimension). As mentioned previously, nine asphalt mixes containing unmodified and modified asphalt binders were analyzed in this study. The description of these binders is given in Table 1. The asphalt mixtures were prepared by mixing these binders with diabase aggregates from the same source using the same aggregate gradation. The aggregate gradation met the requirements of the Virginia Department of Transportation (VDOT) SM-3 surface mixture gradation, with a nominal maximum aggregate size (NMAS) of 19mm. The resulting mixtures were tested using the SPT at a temperature of 50°C and a range of frequencies (0.1, 0.5, 1, 5, 10 and 25Hz) in order to characterize their viscoelastic behavior. After being tested, the HMA specimens were vertically sliced into two halves to allow imaging of the material microstructure. Imaging techniques were utilized to capture and translate the HMA microstructure into a binary text format based on the light intensity of each pixel within the image, (i.e., 0 for mastic and 255 for aggregate). An image resolution of 360 μ m/pixel was used. Image processing followed the methodology described by Papagiannakis et al. (2002). The HMA model geometry was defined using these light intensities, whereby discrete particles were generated corresponding to each of the 0s and the 255s, while maintaining their order of presence within the assembly. Appropriate material properties were incorporated to describe the interaction among the discrete particles. Aggregate particles were assumed rigid, while the time-dependent deformation within the viscoelastic mastic phase was defined using the Burger model. This was justified based on the significant difference in stiffness between aggregate and mastic, which entails high deformation within the mastic phase compared to that within the aggregate phase. Dynamic loading conditions similar to those applied in the SPT device were used in the analysis. Finally, model predictions of the dynamic modulus and the phase angle were compared to experimental data at several loading frequencies. Interested readers are referred to Abbas (2004) for further information.

Table 1. Descriptions of the Asphalt Binders

Name of Asphalt	Percent Polymer	PG of Base Asphalt	Description Provided by the Source	Trade Name	Source
Unmodified Asphalts	0	Not Applicable	PG 52-34, PG 64-28, and PG 70-22	Not Applicable	Citgo Asphalt Refining Co.
Terpolymer	2.2	50% 52-34 50% 64-28	Ethylene Terpolymer	<i>Elvaloy</i>	DuPont
SBS Linear	3.75	58.9% 52-34 41.1% 64-28	Styrene-Butadiene-Styrene	<i>Dexco Vector 2518</i>	TexPar Labs and Johns
SBS Linear Grafted	3.75	58.9% 52-34 41.1% 64-28	Styrene-Butadiene-Styrene and 0.05% Additive	<i>Dexco Vector 2518</i>	TexPar Labs and Johns
SBS Radial Grafted	3.25	58.9% 52-34 41.1% 64-28	Styrene-Butadiene-Styrene and 0.05% Additive	<i>Shell 1184</i>	TexPar Labs and Johns
EVA	5.5	52-34	Ethylene Vinyl Acetate	<i>Exxon Polybilt 152</i>	TexPar Labs and Johns
EVA Grafted	5.5	52-34	Ethylene Vinyl Acetate and 1.35% Additive	<i>Exxon Polybilt 152</i>	TexPar Labs and Johns
CRA	5.0	64-28	Chemically Modified Crumb Rubber Asphalt	<i>CMCRA</i>	FHWA

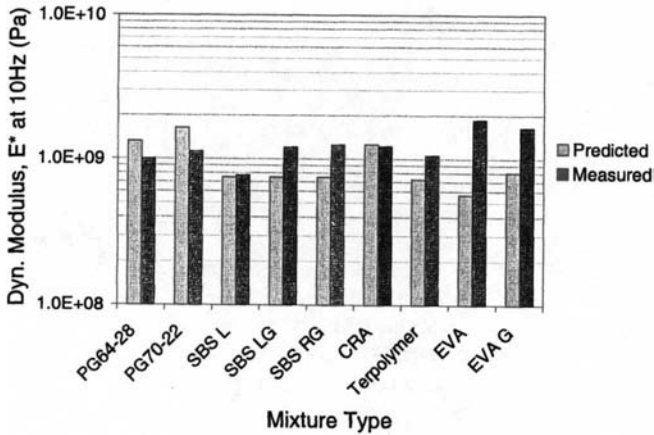


FIG. 5. Measured and Predicted Dynamic Moduli at a Loading Frequency of 10Hz

A comparison between predicted and measured dynamic moduli at a loading frequency of 10Hz is shown in Figure 5 for all nine mixes analyzed. As can be noticed, model predictions exceeded the actual measurements for the asphalt mixtures prepared using unmodified asphalt binders, while they under-predicted the dynamic modulus of those prepared using modified asphalt binders. This could be attributed to limitations imposed by the use of the simple Burger model that could not capture the wide time relaxation spectrum of these complex binders. On the other hand, the predicted phase angles were higher than experimentally measured. This was attributed to the relatively low resolution used in the model and the incorporation of 2-D rather than 3-D analyses.

3.2 Fracture Mechanism of HMA Concretes at Low Temperatures

The fracture mechanism of HMA concretes at low temperatures as tested in the IDT was simulated using the DEM approach. Two models were artificially generated consisting of the same volumetric concentration of aggregates, but different film thicknesses (Figure 6). Each model consisted of about 36,250 cylindrical particles, out of which almost 21,000 were aggregate. The discrete particles within these models were arranged using hexagonal packing, whereby each particle was initially in contact with six neighboring particles prior to loading. Both aggregate and binder particles were defined using linear elastic particles connected with contact bonds of varying strengths. An elastic modulus of 35GPa was assumed for the aggregate and an elastic modulus of 3GPa was assumed for the asphalt binder. The latter is a value that was experimentally established for most asphalt binders at extremely low temperatures (Christensen and Anderson, 1992).

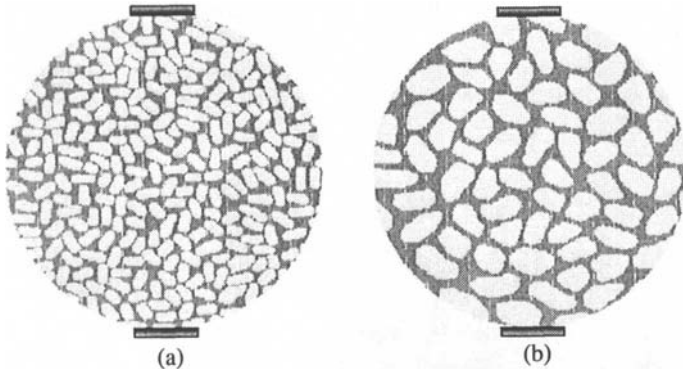


FIG. 6. Discrete Element IDT Models Containing (a) Small-Sized Aggregates; Thin Films of Binder (b) Large-Sized Aggregates; Thick Films of Binder

Three types of bonds were included in these simulations in order to account for the cohesion within the asphalt binder, the cohesion within each aggregate particle, and the adhesion between the aggregate and the binder. For modeling purposes, a strength value of 2.8MPa that is quite common for the asphalt binder was used in the simulation to describe the cohesive failure within that phase. Adhesive failure, on the other hand, was defined using two strength values of 2.8MPa and 8.4MPa in order to simulate weak and strong systems, respectively. A rather high strength value of 24MPa was used for the fracture within the aggregate cluster. Loading was achieved via the upper and lower platens. The deformation rate was gradually increased from zero at the beginning of the simulation to 50mm/sec using an analysis time step of 10^{-7} seconds. Higher deformation rate was applied in the simulation than what is used in the actual test in order to reduce the computation time. The simulation lasted for about 8 hours using 200,000 time steps. The deformation rate was selected, however, small enough to ensure that the model remains in quasi-static equilibrium. The adequacy of the deformation rate was verified by stopping the analysis within the linear region (i.e., before cracking), and monitoring the load level at the platens. A constant load was attained, which indicates that the deformation rate was low enough not to produce large acceleration and thus, high inertia forces that might result in premature damage to the specimen.

The stress-strain behavior of the abovementioned models is presented in Figure (7) for the two cases of weak and strong adhesive bonding. The vertical load was calculated by taking the average of the reaction forces on the upper and lower loading platens and the vertical displacement was taken as the change in the model height along the loading axis. In this figure, it can be seen that the model containing thin films of binder is more sensitive to the adhesive bond strength than that containing the thick films of binder. In the case of the thin films, the tensile strength increased from 1.87 to 2.35MPa (i.e., 26% increase) and failure strain increased from 0.08% to 0.11%. Meanwhile, in the case of the thick films the tensile strength increased from 1.93 to 2.16MPa (i.e., 12% increase) and failure strain increased from 0.07% to 0.08%. This

implies that fracture is mainly dominated by the adhesive failure in the case of the thin films, while it is controlled by the cohesive failure in the case of the thick films. As expected, a sharp drop in load level is noticed after failure in the case of the thin film model, which is an indication of a brittle material, while the load level gradually decreased after failure in the case of the thick film model, which is an indication of a ductile material.

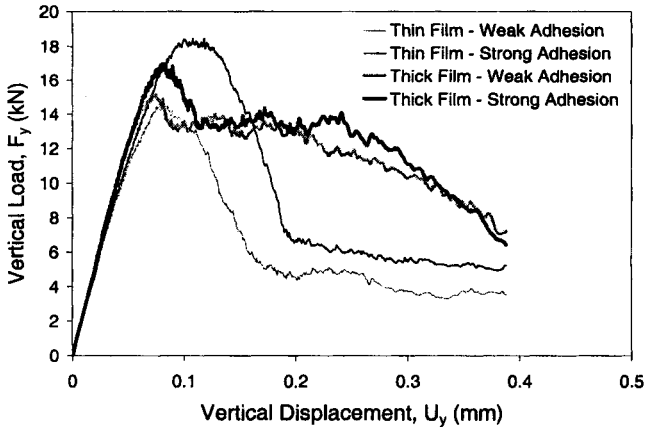


FIG. 7. Resulting Response of Two Models Containing Thin and Thick Films of Asphalt Binder Using Strong and Weak Adhesion Bonds

A closer look at the fracture mechanism revealed that cracking had the tendency to occur at the interface between the aggregate and the binder (i.e., adhesive failure) due to the high stress concentration. The increase in the adhesive bond strength with regard to the cohesive bond strength resulted in cracks within the weaker region, and this fracture was dominated by the cohesive failure mode. This behavior is consistent with what was found by Lytton (2004), who compared analytical solutions of the tensile strength of asphalt cement as a function of the binder film thickness to experimental data obtained by Marek and Herrin (1968).

4. CONCLUSIONS

The following conclusions are drawn from the DEM simulations described above:

- The DEM approach captured the exponential effect of the aggregate filler volume fraction on the mastic stiffness as experimentally observed. The predicted dynamic shear modulus of the mastic was shown to be highly dependent on the dynamic shear modulus of the binder, which is in agreement with experimental data.
- In order to obtain reasonable E^* predictions, the binder stiffness was multiplied by a factor of 30. This was rationalized based on the combined effect of the presence

of fines in the binder, the thickness of the binder film in the images investigated, and analyzing a 3-D problem through a 2-D model. These factors suggest larger strain predictions within the mastic phase and hence, are accounted for through the 30 multiplier. The predicted HMA dynamic moduli compared well with the experimentally measured values for all mixes except those prepared with the EVA and the EVA grafted binders. This was referred to the complex nature of these binders, which were prepared by adding a plastomer modifier to the base asphalt binder. The mix phase angles, however, were over-predicted for all mixtures. This was attributed to limitations imposed by the low resolution used in the models and the incorporation of 2-D rather than 3-D analyses.

- Two systems of weak and strong adhesive bonds along with thin and thick films of binders were analyzed. It was noticed that the models containing thin films of binder were more sensitive to the adhesive bond strength than those containing thick films of binder. Furthermore, it was observed that cracking has the tendency to occur at the interface between the aggregate and the binder (cohesive failure) due to the high concentration of stresses. Failure mode was dependent on the binder film thickness; thin binder films implied adhesion failure, whereas thick films implied cohesive failure.

5. REFERENCES

- Abbas, A. (2004). Simulation of the Micromechanical Behavior of Asphalt Mixtures using the Discrete Element Method. Ph.D. Dissertation, Department of Civil and Environmental Engineering, Washington State University, Pullman, WA.
- Abbas, A., Masad, E., Papagiannakis, T., and Shenoy, A. (2005). Modeling Asphalt Mastic Stiffness Using Discrete Element Analysis and Micromechanics-Based Models. *The International Journal of Pavement Engineering*, Vol. 6, No. 2, pp. 137-146.
- Lytton, R.L (2004). Adhesive Fracture in Asphalt Concrete Mixtures. Course Notes.
- Marek, C.R. and Herrin, M. (1968). Tensile Behavior and Failure Characteristics of Asphalt Cements in Thin Films. *Journal of the Association of Asphalt Paving Technologists*, AAPT, Vol. 37, pp. 386-421.
- Papagiannakis, A.T., Abbas, A., and Masad, E. (2002). Micromechanical analysis of viscoelastic properties of asphalt concretes. *Transportation Research Record 1789, TRB*, National Research Council, Washington, D.C., pp. 113-120.
- PFC2D (2003). Particle Flow Code in 2-Dimensions. Version 3-163. Itasca Consulting Group.
- Shashidhar, N., Needham, S.P., Chollar, B.H. and Romero, P. (1999). Prediction of the Performance of Mineral Fillers in SMA. *Proceedings of the Association of Asphalt Paving Technologists*, Vol. 68, pp. 222-251.
- Shashidhar, N. and Shenoy, A. (2002). On Using Micromechanical Models to Describe Dynamic Mechanical Behavior of Asphalt Mastics. *Mechanics of Materials*, Vol. 34, Issue 10, pp. 657-669.

A MICROMECHANICAL VISCOELASTO-PLASTIC MODEL FOR ASPHALT MIXTURE

Qingli Dai¹, Zhanping You², and Martin H. Sadd³

ABSTRACT

This paper presents a finite element (FE) micromechanical model for viscoelasto-plastic behavior of asphalt mixtures. Asphalt mixture is composed of highly irregular aggregates, mastic (asphalt plus fine aggregate and fines), and air voids. In this paper, the microstructural model of particulate asphalt materials incorporates an equivalent lattice network structure whereby intergranular load transfer is simulated through an effective asphalt mastic zone. The finite element model integrates the ABAQUS user material subroutine with continuum elements for the effective asphalt mastic and rigid body elements for each aggregate. A FE incremental algorithm with a recursive relationship for three-dimensional (3D) viscoelastic behavior was developed. Chaboche's plastic model was applied, and the constitutive equations were solved using a predictor-corrector scheme. These algorithms were defined in a 3D user material model for the asphalt mastic to predict global rate-independent permanent deformation of asphalt materials. The effect of loading rates on the material viscoelastic and viscoelasto-plastic behavior was investigated using FE numerical simulations for an ideal asphalt mixture specimen.

INTRODUCTION

Asphalt mixtures are complex composite materials of graded aggregates bound with the mastic. The mastic itself consists of fine aggregate, sand, and fines embedded in a matrix of asphalt binder. The physical properties and performance of HMA is governed by the properties of the aggregate (shape, surface texture, gradation, skeletal structure, modulus, etc.), properties of the asphalt binder (grade, complex modulus, relaxation characteristics, cohesion, etc.), and asphalt-aggregate

¹ Research Associate, Dept. of Environmental and Civil Engineering, Texas A&M University- Kingsville, Kingsville, TX 78363, mecdql@yahoo.com

² Assistant Professor, Dept. of Environmental and Civil Engineering, Texas A&M University- Kingsville, Kingsville, TX 78363, zhanping.you@tamuk.edu

³ Professor, Dept. of Mechanical Engineering and Applied Mechanics, University of Rhode Island, Kingston, RI 02881, sadd@egr.uri.edu

interactions (adhesion, absorption, physio-chemical interactions, etc.). In addition, aggregate particles in the mixture have different shapes, surface texture and friction, and orientations, which make the aggregate contact more complicated. Asphalt mastic has complex constitutive properties including inelastic, viscoelastic and plastic/viscoplastic behaviors. The load carrying behavior and resulting failure of such materials depends on many phenomena that occur at the aggregate/mastic level. Thus the overall macro behavior is determined by the micromechanics within the cemented particulate system. Because of the heterogeneous multiphase nature of asphalt material, it appears that a micromechanical model would be best suited to properly simulate such material.

A number of researchers have developed micromechanical models to predict the fundamental properties of the mixture based upon those of the phase constituents. You and Buttlar (2004) employed discrete element to characterize the properties of asphalt mixture. Sadd et al. (2004a,b) employed a micro-frame network model to investigate the damage behavior of asphalt mixture.

Dai and Sadd (2004) investigated linear and damage-coupled viscoelastic behavior of asphalt mixture based on a generalized Maxwell viscoelastic model and Schapery's nonlinear viscoelastic model. Following these studies, this paper presents a micromechanical-modeling scheme for the viscoelasto-plastic behavior of asphalt mixtures by using finite element methods. Maxwell-type viscoelastic model and Chaboche's plastic model (Chaboche and Cailletaud (1986), Chaboche (1989)) were combined to investigate viscoelasto-plastic behavior of asphalt mixtures. Finite element analysis was conducted with a displacement-based incremental formulation for the viscoelastic part and an elastic predictor-plastic corrector algorithm for elastoplastic behavior.

VISCOELASTO-PLASTIC MODEL FOR ASPHALT MASTIC

A viscoelasto-plastic model is proposed for the study of rate independent permanent deformation in asphalt mastic. This model includes the Maxwell-type viscoelastic elements and an elastoplastic part in parallel as shown in Fig. 1.

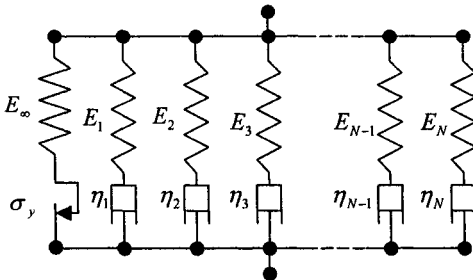


Fig. 1. Viscoelasto-plastic mastic model

Maxwell-Type Viscoelastic Model

The generalized Maxwell model was used to simulate the linear and damage-coupled viscoelastic behavior of asphalt mixture by Dai and Sadd (2004). The linear constitutive behavior for this Maxwell-type model can be expressed as a hereditary integral

$$\sigma = \int_0^t E_i \frac{d\varepsilon(\tau)}{d\tau} d\tau \quad (1)$$

where E_i is expressed with a Prony series

$$E_i = \sum_{m=1}^M E_m e^{-\frac{(t-\tau)}{\rho_m}}, \text{ and } \rho_m = \frac{\eta_m}{E_m} \quad (2)$$

In these equations, E_i is the transient modulus as a function of the time, E_m , η_m and ρ_m are the spring constant, dashpot viscosity and relaxation time respectively for the m^{th} Maxwell element.

The reduced time (effective time) is defined by using time-temperature superposition principle as

$$\xi(t) = \int_0^t \frac{1}{\alpha_\tau} d\tau \quad (3)$$

where the term $\alpha_\tau = \alpha_\tau(T(\tau))$ is a temperature-dependent time-scale shift factor.

Three-dimensional behavior can be formulated with uncoupled volumetric and deviatoric stress-strain relations. A displacement based incremental finite element modeling scheme with constant strain rate over each increment has been developed.

The volumetric constitutive relationship is expressed with the volumetric stress σ_{kk} and strain ε_{kk} in the general form

$$\sigma_{kk}(\xi) = \int_0^\xi 3K_i(\xi - \xi') \frac{d\varepsilon_{kk}(\xi')}{d\xi'} d\xi' \quad (4)$$

where $K_i(\xi - \xi') = \sum_{m=1}^M K_m e^{-\frac{(\xi - \xi')}{\rho_m}}$ is the transient bulk modulus. The incremental formulation of the volumetric behavior is obtained with constant volumetric strain rate $R_{kk} = \frac{\Delta\varepsilon_{kk}}{\Delta\xi}$,

$$\Delta\sigma_{kk} = 3 \left[\sum_{m=1}^N \frac{K_m \rho_m}{\Delta\xi} \left(1 - e^{-\frac{\Delta\xi}{\rho_m}} \right) \right] \Delta\varepsilon_{kk} + \Delta\sigma_{kk}^R \quad (5)$$

and the residual part $\Delta\sigma_{kk}^R$ can be expressed in a recursive relation with the history variable S_m ,

$$\Delta\sigma_{kk}^R = \sum_{m=1}^M \left(1 - e^{-\frac{\Delta\xi}{\rho_m}} \right) S_m(\xi_n), \text{ and } S_m(\xi_n) = 3K_m R_{kk} \rho_m \left(1 - e^{-\frac{\Delta\xi}{\rho_m}} \right) + S_m(\xi_{n-1}) e^{-\frac{\Delta\xi}{\rho_m}} \quad (6)$$

For the initial increment, the history variable $S_m(\xi_1)$ equals to $3K_m R_{kk} \rho_m \left(1 - e^{-\frac{\Delta\xi}{\rho_m}} \right)$.

For the deviatoric behavior, the constitutive relationship is written using deviatoric stress $s_{ij} = \sigma_{ij} - \frac{1}{3}\sigma_{kk}\delta_{ij}$ and deviatoric strain $\hat{\varepsilon}_{ij} = \varepsilon_{ij} - \frac{1}{3}\varepsilon_{kk}\delta_{ij}$,

$$s_{ij}(\xi) = \int_0^{\xi} 2G_i(\xi - \xi') \frac{d\hat{\varepsilon}_{ij}(\xi')}{d\xi'} d\xi' \quad (7)$$

where $G_i(\xi - \xi') = \sum_{m=1}^N G_m e^{-\frac{(\xi - \xi')}{\rho_m}}$ is the transient shear modulus. The formulation of

the deviatoric behavior is obtained with constant deviatoric strain rate $\hat{R}_{ij} = \frac{\Delta\hat{\varepsilon}_{ij}}{\Delta\xi}$,

$$\Delta s_{ij} = 2 \left[\sum_{m=1}^N \frac{G_m \rho_m}{\Delta\xi} \left(1 - e^{-\frac{\Delta\xi}{\rho_m}} \right) \right] \Delta\hat{\varepsilon}_{ij} + \Delta s_{ij}^R \quad (8)$$

and the residual part Δs_{ij}^R can be expressed in the recursive relation

$$\Delta s_{ij}^R = \sum_{m=1}^N \left(1 - e^{-\frac{\Delta\xi}{\rho_m}} \right) S_m(\xi_n), \text{ and } S_m(\xi_n) = 2G_m \hat{R}_{ij} \rho_m \left(1 - e^{-\frac{\Delta\xi}{\rho_m}} \right) + S_m(\xi_{n-1}) e^{-\frac{\Delta\xi}{\rho_m}} \quad (9)$$

For the initial increment, the history variable $S_m(\xi_1)$ equals to $2G_m \hat{R}_{ij} \rho_m \left(1 - e^{-\frac{\Delta\xi}{\rho_m}} \right)$.

Chaboche's Plastic Model

Chaboche and Cailletaud (1986) extended the nonlinear hardening plasticity model proposed by Mróz et al. (1975) for cyclic loading. The yield function with nonlinear isotropic and kinematic hardening was defined with the von Mises criteria,

$$f = L(\boldsymbol{\sigma} - \mathbf{x}) - \sigma_y \quad (10)$$

where,

$$L(\boldsymbol{\sigma} - \mathbf{x}) = \sqrt{\frac{3}{2}(s_{ij} - \alpha_{ij})(s_{ij} - \alpha_{ij})} \quad \text{and} \quad \sigma_y = \sigma_0 + \sigma_s(1 - e^{-b\lambda}) \quad (11)$$

In these equations, $L(\boldsymbol{\sigma} - \mathbf{x})$ is the von Mises equivalent stress, $\boldsymbol{\sigma}$ and s_{ij} are Cauchy and deviatoric stress tensors, \mathbf{x} is back stress tensor related to nonlinear kinematic hardening and α_{ij} is its deviatoric tensor with $\alpha_{ij} = x_{ij} - \frac{1}{3}x_{kk}\delta_{ij}$, σ_y and σ_0 are the evolving and initial yield stresses, σ_s and b are the two parameters for nonlinear isotropic hardening, and λ is the accumulated plastic strain.

The nonlinear kinematic hardening which introduces a dynamic recovery effect is described as,

$$d\alpha_{ij} = \frac{2}{3}C d\varepsilon_{ij}^p - \gamma\alpha_{ij}d\varepsilon_e^p \quad (12)$$

with a particular solution,

$$d\alpha_{ij} = \frac{2}{3}H'_\alpha(\varepsilon_e^p)d\varepsilon_{ij}^p \quad \text{and} \quad H'_\alpha(\varepsilon_e^p) = Ce^{-\gamma\varepsilon_e^p} \quad (13)$$

$$\alpha_{ij} = \sqrt{\frac{2}{3}}H_\alpha(\varepsilon_e^p)\mathbf{n} = \sqrt{\frac{2}{3}}\frac{C}{\gamma}(1 - e^{-\gamma\varepsilon_e^p})n_{ij}, \quad \text{and} \quad n_{ij} = \frac{s_{ij} - \alpha_{ij}}{|s_{ij} - \alpha_{ij}|} \quad (14)$$

In these equations, C and γ are the two parameters for nonlinear kinematic hardening, ε_{ij}^p is the plastic strain tensor, ε_e^p is the equivalent plastic strain with $\varepsilon_e^p = \left(\frac{2}{3}\varepsilon_{ij}^p\varepsilon_{ij}^p\right)^{1/2}$, $H_\alpha(\varepsilon_e^p)$ is a scalar variable of ε_e^p , and \mathbf{n} is the unit normal to the yield surface and indicates the plastic strain direction for associated flow.

Assuming the associated flow rule applies, the incremental plastic strain is formulated as,

$$d\varepsilon_{ij}^p = \frac{1}{K_p}(\mathbf{n} : \boldsymbol{\sigma})\mathbf{n} = \frac{1}{K_p}(n_{kl}d\sigma_{kl})n_{ij} = d\beta(s_{ij} - \alpha_{ij}) = d\beta r_{ij}, \quad \text{and} \quad r_{ij} = s_{ij} - \alpha_{ij} \quad (15)$$

where K_p is a scalar parameter, and $d\beta$ is an incremental scalar variable. The incremental back stress is also given as,

$$d\alpha_{ij} = \frac{2}{3}H'_\alpha(\varepsilon_e^p)d\varepsilon_{ij}^p = \frac{2}{3}Ce^{-\gamma\varepsilon_e^p}d\varepsilon_{ij}^p = d\beta h_{ij}, \quad \text{and} \quad h_{ij} = \frac{2}{3}Ce^{-\gamma\varepsilon_e^p}r_{ij} \quad (16)$$

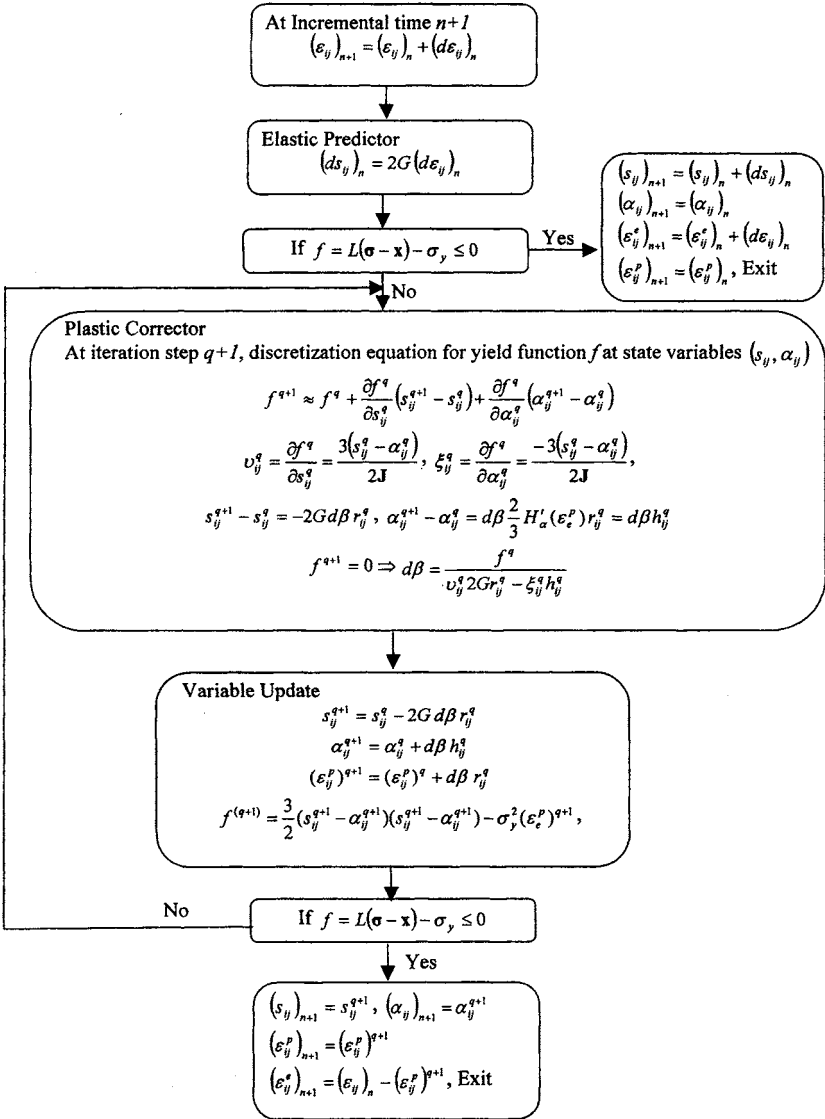


Fig. 2. Elastic predictor – plastic corrector algorithm

FINITE ELEMENT ANALYSIS

The proposed viscoelasto-plastic mastic model has been incorporated into a finite element framework for the behavior of asphalt mixtures. The ABAQUS finite element package and its user subroutine UMAT were used. A displacement-based incremental formulation for the viscoelastic analysis was described previously. For the elastoplastic element, a return mapping method was employed within the framework of elastic predictor and plastic corrector algorithm (Simo and Ortiz (1985), and Ortiz and Simo (1986)). The constitutive equations will be discretized with backward Euler method, which is unconditionally stable. The detailed predictor – corrector algorithm is shown in Fig. 2.

MICROSTRUCTURAL MODEL

The microstructural model incorporates an equivalent lattice network structure whereby intergranular load transfer is simulated through an effective asphalt mastic zone. The ABAQUS finite element model combines the user-defined material subroutine with continuum elements for the effective asphalt mastic and rigid body defined with rigid elements for each aggregate. The continuum elements and rigid elements shear the nodes along the aggregate boundary. Detailed information on micromechanical finite element model can be found in Dai and Sadd (2004).

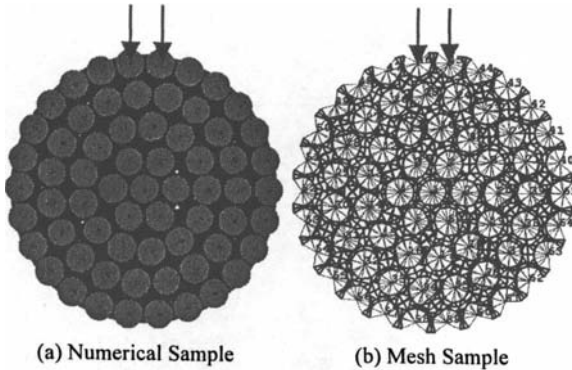


Fig. 3. Indirect tension numerical sample

A MATLAB code was developed to generate two-dimensional numerical asphalt specimens, and the element geometry properties and connectivity were created and saved in input files for ABAQUS modeling and analysis. A two-dimensional indirect tension specimen has been generated with MATLAB code as shown in Fig. 3(a), and its mesh figure was modeled by using ABAQUS elements as shown in Fig. 3(b). This particular model has 65 aggregate particles (in four particle size groupings), 195 effective mastic zones, 7.6% porosity and an approximate overall diameter of 102 mm (4 in). This microgeometry results in a total of 780 deforming mastic elements and 1170 rigid aggregate elements with connectivity as shown.

MODEL SIMULATION

Step Loading With Different Loading Rates

The step loading responses of viscoelastic and viscoelasto-plastic mastic models were investigated with indirect tension simulations on the numerical specimen (shown in Fig. 3). The mastic elements had 3-parameter viscoelastic constitutive properties with relaxed elastic moduli $E_{\infty} = 412.8$ MPa and one Maxwell element of spring constant $E_1 = 1232$ MPa and relaxation time $\rho_1 = 6.5$ s. These constitutive properties were selected from asphalt mixture characterization testing by Gibson et al. (2003). It was assumed that Poisson's ratio ν did not change with time and was given as 0.3. The initial yield stress σ_0 was chosen as 40 MPa, the nonlinear isotropic hardening parameters σ_s and b were 40 MPa and 0.3, and the nonlinear kinematic hardening parameters C and γ were also 40 MPa and 0.3. For the displacement-controlled step-loading simulation, the x- and y- displacements of the particles on the bottom layer and the x- displacements of the particles on the top layer were constrained, while the top particle pair accept the applied vertical displacement loading.

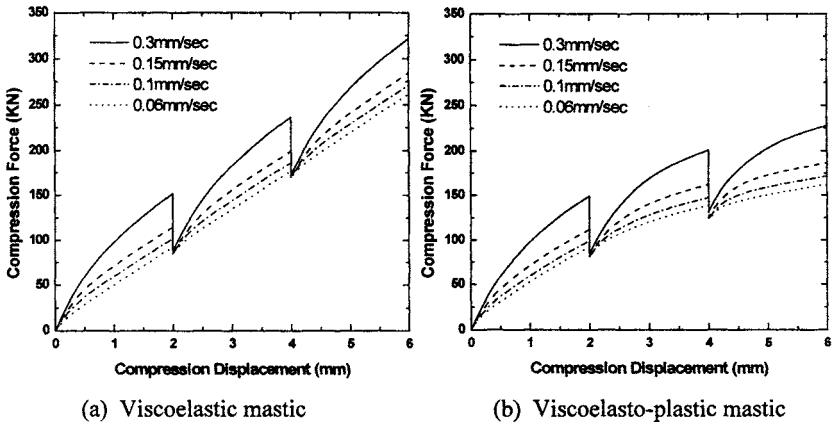


Fig. 4. Step loading simulation with different loading rates

Viscoelastic and viscoelasto-plastic simulation under different loading rates were compared in Fig. 4. Results indicate that viscoelastic behavior returns to a linear response after enough recovery time, while viscoelasto-plastic behavior maintains a nonlinear trend. Comparing these two responses, it is observed that the viscoelasto-plastic model carries lower loading due to the additional plastic behavior for the displacement-controlled boundary conditions. Both behaviors show that higher loading rates generate larger specimen stiffness with less relaxation time.

CONCLUSIONS

A micromechanical constitutive model was formulated and used to simulate the viscoelasto-plastic behavior of asphalt mixture. The aggregate-mastic microstructure was simulated by incorporating the user material subroutine with continuum elements for asphalt mastic and rigid body elements for each aggregate. Maxwell-type viscoelastic and Chaboche's plastic modes were combined to investigate the asphalt viscoelasto-plastic behavior. Finite element analysis incorporated the displacement-based incremental algorithm for viscoelastic part and predictor-correct scheme for elastoplastic element. This behavior was defined in the ABAQUS user material subroutine for the asphalt mastic to predict global viscoelasto-plastic behavior of asphalt mixture. Model prediction on the image sample will be compared with laboratory specimen test data. Future modeling efforts will be extended to rate-dependent permanent deformation behavior, and this work is underway.

REFERENCES

- Chaboche, J. L. (1989). "Constitutive Equations for Cyclic Plasticity and Cyclic Viscoplasticity," *Int. J. of Plasticity*, 5, 247-302.
- Chaboche, J. L., and Cailletaud, G. (1986). "On the Calculation of Structures in Cyclic Plasticity or Viscoplasticity," *Computers and Structures*, 23(1), 23-31.
- Dai, Q. L., and Sadd, M.H. (2004). "Micromechanical Modeling of Damage-coupled Viscoelastic Behavior of Asphalt Materials," *Proc. of 17th ASCE Engineering Mechanics Division Conference (CD-Rom)*, Delaware, USA, June 13-16.
- Gibson, N. H., Schwartz, C. W., Schapery, R. A., and Witzczak, M.W. (2003). "Viscoelastic, viscoplastic, and Damage Modeling of Asphalt Concrete in Unconfined Compression," *Proc. of 82nd Transportation Research Board Annual Meeting*, Washington, D. C.
- Mróz, Z., Shrivastava, H. P., Nubey, R. N. (1976). "A Non-linear Hardening Model and Its Application to Cyclic Loading," *Acta Mech.*, 25, 51-61.
- Ortiz, M., and Simo, J.C. (1986). "An Analysis of a New Class of Integration Algorithms for Elastoplastic Constitutive Relations," *Int. J. Numer. Methods Engng.*, 23, 353-366.
- Sadd, M.H., Dai, Q.L., Parameswaran, V., Shukla, A. (2004a). "Microstructural Simulation of Asphalt Materials: Modeling and Experimental Studies", *J. Matl. in Civil Engng.*, ASCE 16(2), 107-115.
- Sadd, M.H., Dai, Q.L., Parameswaran, V., and Shukla, A. (2004b). "Simulation of Asphalt Materials Using a Finite Element Micromechanical Model and Damage Mechanics", *J. Trans. Res. Record*, No. 1832, 86-94.
- Simo, J.C., and Ortiz, M. (1985). "A Unified Approach to Finite Deformation Elastoplastic Analysis Based on the Use of Hyperelastic Constitutive Equations," *Comput. Meths. Appl. Mech. Engrg.*, 49, 221-245.
- You, Z. and Buttlar, W.G. (2004). "Discrete Element Modeling to Predict the Modulus of Asphalt Concrete Mixtures," *Journal of Materials in Civil Engineering*, ASCE, Vol. 16, Issue 2, pp. 140-146.

DEVELOPMENT AND IMPLEMENTATION OF A FINITE ELEMENT MODEL FOR ASPHALT MIXTURE TO PREDICT COMPRESSIVE COMPLEX MODULI AT LOW AND INTERMEDIATE TEMPERATURES

Zhanping You¹, Qingli Dai², and Bardan Gurung³

ABSTRACTS: Many researchers recognized that micromechanical models have tremendous potential in the field of asphalt technology, for reducing or eliminating costly tests to characterize asphalt-aggregate mixtures for the design and control of flexible pavement structures and materials. The objective of this study is to develop micromechanical based finite element (FE) model to capture the microstructure of asphalt mixture and to predict mixture properties. In this approach, various material phases (aggregates and mastic) are modeled with a number of fine finite elements. Aggregate geometry, shape, orientation, and gradation are considered in the modeling. Furthermore, high-resolution images are used to study the microstructure of asphalt mixture and to prepare geometry input for the FE model. In addition, the complex modulus (E^*) of the sand mastic (asphalt plus fine aggregate) are measured by an experimental program and used to compare the prediction of FE model. The E^* of the asphalt mixture are measured and used to compare the prediction of FE model. The developed FE approach has the ability to predict asphalt mixture complex moduli in compression across a range of loading frequencies at low and intermediate temperatures (-20 , -10 , and 0°C).

INTRODUCTION

Asphalt mixture is a composite material including mastic and aggregate as well as air voids. This multiphase material has different properties from the original components—aggregate and mastic. Because of the heterogeneous multiphase nature of asphalt material, it appears that a micromechanical model would be best suited to properly simulate such a material. Buttlar and You (2001) summarized work by a number of researchers in the development of micromechanical models to predict the

¹ Assistant Professor, Ph.D., P.E., Dept. of Environmental and Civil Engineering, Texas A&M University- Kingsville, Kingsville, TX 78363, zyou@tamuk.edu

² Research Associate, Ph.D., Dept. of Environmental and Civil Engineering, Texas A&M University- Kingsville, Kingsville, TX 78363, qingli.dai@tamuk.edu

³ Graduate student, Dept. of Environmental and Civil Engineering, Texas A&M University- Kingsville, Kingsville, TX 78363

fundamental properties of the mixture based upon those of the phase constituents. Finite element modeling of asphalt concrete microstructure potentially allows accurate modeling of aggregate and mastic microstructure geometry. In addition, Stankowski (1990) applied finite element techniques to model cemented particulate composites. Some research work was conducted using finite element techniques, such as the work by Sepehr et al. (1994), Bazant, et al. (1990), Mora (1992), Sadd et al. (2004), Budhu et al. (1997), Guddati et al. (2002), Bahia et al. (2002), Papagiannakis, et al. (2002), Mustoe and Griffiths (1998), Kose et al. (1999), Masad and Bahia (2002), Masad et al. (2001a, 2001b, and 2002), Dai and Saad (2005), Dai et al. (2004), and Dai (2004).

Other than finite element methods, researchers employed discrete element and boundary element approach in the modeling of asphalt mixture. Birgisson et al. (2002) applied a displacement discontinuity boundary element approach to model the fracture behavior of asphalt mixtures. Discrete element method (DEM) was applied on cemented particulate materials in recent years, including the contribution by Rothenburg et al. (1992), Trent and Margolin (1994), Chang and Meegoda (1997, 1999), Ullidtz (2001), Sadd et al. (1997,1998), Buttlar and You (2001), and You (2003). You and Buttlar (2004, 2005) employed DEM to characterize the properties of asphalt mixture.

Most recently, some researchers conducted study on the three dimensional microstructure of asphalt mixture using x-ray computerized tomography (Wang et al., 2004 and Masad et al., 2002). These investigations will help three-dimensional modeling of the microstructure of asphalt mixture.

In this paper, the finite element method will be employed to characterize the stiffness of asphalt mixture. Herein we use the term 'stiffness' in a general sense to refer to any of a number of stress/strain moduli that can be measured and/or predicted, such as complex modulus, dynamic modulus, relaxation modulus, or creep stiffness (inverse of creep compliance). This study will focus on the finite element model for asphalt mixture to predict mixture complex moduli in compression at low and intermediate temperatures.

ASPHALT MIXTURE SPECIMENS PREPARATION AND LABORATORY TESTS

The asphalt mixture properties were from a study at the University of Illinois at Urbana-Champaign (You, 2003; You and Buttlar, 2004 & 2005). The aggregate gradation for the mixture and sand mastic is in Table 1. The grade of asphalt used is superpave performance grade PG 64-22 binder. The sand mastic comprised of the portion of the aggregate gradation finer than 2.36 mm combined with the volume of binder normally used in the entire asphalt concrete mixture. The asphalt content in sand mastic is around 14.4 % by weight of mixture. The aggregate size ranges from 0.075 to 19 mm nominal diameter. The final dimension of cylindrical specimen is 75mm in diameter and 150 mm in height. The complex moduli of both the sand mastic and mixture were tested across a range of loading frequencies (0.1, 1, 5, and 10 Hz) and low and intermediate test temperatures (0, -10, and -20°C).

Table 1: Aggregate gradation

Sieve Size (mm.)	% Passing	
	19 mm mixture	Sand mastic
25	100	100
19	98.9	100
12.5	77.5	100
9.5	68.4	100
4.75	56.2	100
2.36	46.2	46.2
1.18	31.7	31.7
0.6	20.8	20.8
0.3	12.6	12.6
0.15	8.3	8.3
0.075	5.6	5.6

Aggregate moduli were measured in laboratory and a typical modulus of 55.5GPa for limestone was used in the FE models in this study. Asphalt mastic complex moduli across a range of loading frequencies (0.1, 1, 5, and 10 Hz) and test temperatures (0, -10, and -20°C) were used as input parameters in the FE models.

MICROSTRUCTURE MODELING OF THE MIXTURE

Image analysis was used in this study to capture the microstructure of the mixture. The microstructure of asphalt mixture was generated from the 2D image of a cross section of mixture specimen. Figure 1 shows the FE meshes of the aggregate skeleton of a piece of asphalt mixture, where the sand mastic comprised of the portion of the aggregate gradation finer than 2.36 mm combined with the volume of binder. A total number of 319,458 elements were used in this specific mixture microstructure. Multiphase asphalt materials including very irregular aggregates and complex distributed mastic were divided into different subdomains. Finite element mesh was generated within subdomains (aggregates and mastic) and along the subdomain boundaries. Finite elements in the neighboring domains share the nodes on irregular boundaries, thus the displacements of neighboring subdomains were connected through the shared nodes. Figure 1 also shows the fine finite element meshes in the aggregates and mastic. The density of the meshes in aggregates and mastic is optimized to reduce the total element numbers and computation speed.

Uniaxial compression test simulations were conducted on the finite element model shown in Figure 1. Asphalt mastic complex moduli at different loading frequencies and test temperatures were used as input parameters in the FE models. The specimen responses including uniaxial stress and strain were recorded in order to compute the mixture moduli during compressive loading. Therefore, this FE approach was used to predict asphalt mixture complex modulus in compression at different of loading frequencies and temperatures.

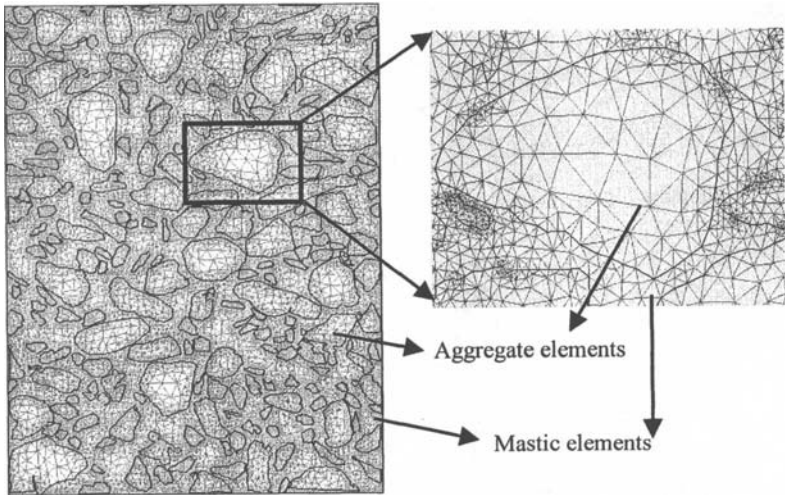


Figure 1. FE meshes of the aggregate skeleton of asphalt mixture (aggregate size are larger than 2.36 mm)

MODULUS PREDICTION OF THE MIXTURE COMPARED WITH MEASUREMENTS

It should be noted that, this study is to compare the mixture moduli from laboratory measurements and FE prediction at several pre-selected temperatures and loading frequencies, similar as the work done by You and Buttlar (2004). In addition, the mastic moduli measured from laboratory material testing are used as input parameters for the FE simulation. The moduli measurements of viscoelastic mastic material vary with loading frequencies and temperatures. Thus the mixture moduli prediction with the calibrated mastic properties will also include the frequency-temperature dependent viscoelastic properties. Therefore the correspondence principle will bridge between the elastic simulation and viscoelastic response through the calibrated viscoelastic mastic moduli. The veracity of this approach was indirectly validated by the favorable match between simulation results and predictions, as discussed by You and Buttlar (2004 and 2005).

Figure 2 shows the mixture complex modulus prediction from FE models with consideration of the microstructure. The figure also shows the measurement of mixture stiffness across a range of loading frequencies and temperatures. Figure 2a shows the prediction and measurement comparison of -20°C , 2b for -10°C , and 2c for 0°C . These three figures show that mastic and mixture complex moduli increase with loading frequencies for a given temperature. Comparing these three figures, it also shows that higher temperatures result in lower complex moduli of mastic as well as the mixture for a given loading frequencies. The comparison between the numerical simulation and lab measurements indicates that the FE predictions are very

reasonable and accurate for the loading frequencies ranges from 0.1, 1, 5, to 10 Hz and test temperatures from 0, -10, to -20 °C.

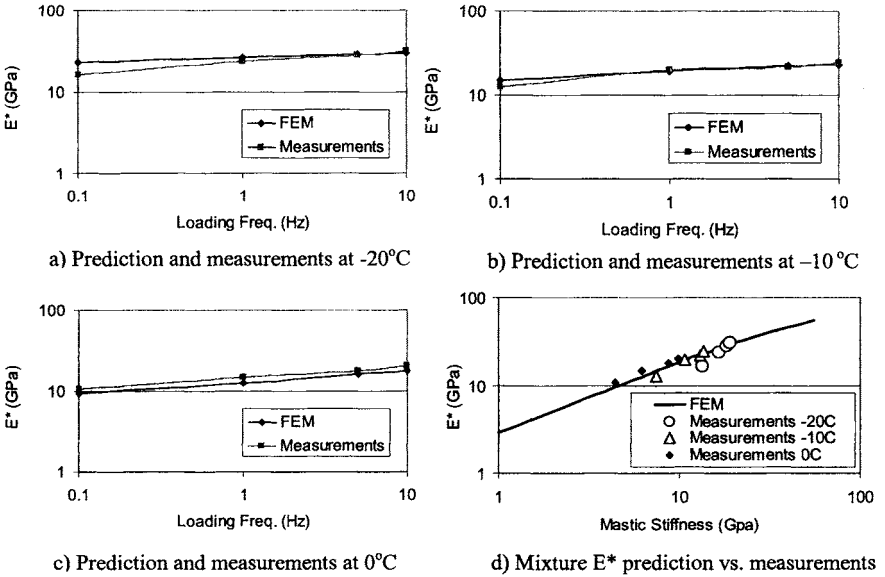


Figure 2. Mixture complex modulus prediction from FE models with consideration of the microstructure compared with test measurement across a range of loading frequencies and temperatures

Figure 2d shows the mixture complex modulus prediction compared with all the mixture stiffness measurement across a range of loading frequencies (0.1, 1, 5, and 10 Hz) and test temperatures (0, -10, and -20 °C). Different temperature responses were indicated with the different makers as shown in figure. In general, viscoelastic mastic stiffness increases with the loading frequency and deceases with temperatures. Mixture modulus varies with the mastic modulus. This figure shows that the prediction line (solid line) is very close to the measurement points of mixture stiffness. There are many data points in the solid line, which correspond to different input mastic modulus. It can be observed that the FE model also predicts the mixture moduli when the mastic moduli are extremely low and high (at extreme high and low temperatures, respectively), even though this kind of laboratory data is not available at this time. As mentioned previously, the FE prediction of mixture moduli has the viscoelastic properties through elastic simulation. The reason is that the viscoelastic modulus of asphalt mastic at the pre-selected temperatures and loading frequencies was measured and taken as input of the FE models.

Aggregate modulus sensitivity analysis (effect to the mixture modulus) is investigated by a number of additional FE computations. A stiffer mixture is expected and observed with stiffer aggregate.

In general, by comparing the numerical simulation and laboratory measurements, it appears that this FE model has satisfactory predictions of the moduli of mixture for the different loading frequencies and test temperatures. Different slices of mixture cross sections were also analyzed. The FE prediction results show that there is no significant difference for many cross sections of this type of mixture, which was discussed in the work by You (2003).

SUMMARY

In this paper, the microstructure of asphalt mixture was generated from the 2D image of a cross section of mixture specimen. Multiphase asphalt materials including aggregates and mastic were divided into different subdomains. Finite element mesh was generated within each selected aggregate or mastic subdomain. Uniaxial compressive FE simulation was conducted on the model. The comparison between the FE prediction and laboratory measurement indicates that the FE predictions of complex moduli of mixture are accurate under the different loading frequencies and test temperatures (low and intermediate temperatures). In the future study, the viscoelastic and viscoplastic material models will be employed in three-dimensional microstructure to predict asphalt mixture properties.

ACKNOWLEDGMENTS

The authors acknowledge the support of Dr. William Buttlar in the laboratory tests at the University of Illinois at Urbana-Champaign.

REFERENCES

- Bahia, H., H. Zhai, K. Bonnetti and S. Kose. (1999). "Nonlinear Viscoelastic and Fatigue Properties of Asphalt Binders," *J. Assoc. Asphalt Paving Tech.*, Vol. 68, pp. 1-34.
- Bazant, Z.P., Tabbara, M.R., Kazemi, Y., and Pijaudier-Cabot, G. (1990). "Random particle simulation of damage and fracture in particulate or fiber-reinforced composites", *Damage Mechanics in Engineering Materials*, Trans. ASME, AMD 109, 41-55.
- Birgisson, B., C. Soranakom, J.A.L. Napier and R. Roque. (2002). "Simulation of the Cracking Behavior of Asphalt Mixtures Using Random Assemblies of Displacement Discontinuity Boundary Elements," *Proc. 15th ASCE Eng. Mechanics Conf.*, Columbia University.
- Budhu, M., S. Ramakrishnan and G. Frantziskonis (1997). "Modeling of Granular Materials: A Numerical Model Using Lattices," *Mechanics of Deformation and Flow of Particulate Materials*, Ed. C.S. Chang, A. Misra, R.Y. Liang and M. Babic, Proc. McNu Conference, Trans. ASCE, Northwestern Univ.

- Buttler, W.G., and You, Z. (2001). "Discrete Element Modeling of Asphalt Concrete: A Micro-Fabric Approach," J. Trans. Res. Record, National Research Council, Washington, D.C., No. 1757, *Geomaterials 2001*, 111-118.
- Chang, G. K. and Meegoda, J. N. (1997). "Micromechanical Simulation of Hot Mixture Asphalt," *ASCE J. Engng. Mech.*, 123(5), 495-503.
- Chang, G. K. and Meegoda, J. N. (1999). "Micro-mechanic Model For Temperature Effects of Hot Mixture Asphalt Concrete," J. Trans. Res. Record, No. 1687, National Research Council, Washington, D.C., 95-103.
- Dai, Q. L. (2004). "Micromechanical Modeling of Constitutive and Damage Behavior of Heterogeneous Asphalt Materials", PhD Dissertation, Mechanical Engineering And Applied Mechanics, University of Rhode Island.
- Dai, Q.L., Sadd, M.H., Parameswaran, V. and Shukla, A. (2005). "Prediction of Damage Behaviors in Asphalt Materials using a Finite Element Micromechanical Model and Image Analysis", *Journal of Engineering Mechanics*, ASCE, to be appear.
- Dai, Q.L., and Sadd, M.H. (2004). "Parametric Model Study of Microstructure Effects On Damage Behavior of Asphalt Samples", *International Journal of Pavement Engineering*, Vol. 5(1), pp. 19-30.
- Guddati, M.N., Z. Feng and Y.R. Kim. (2002). "Towards a Micromechanics-Based Procedure to Characterize Fatigue Performance of Asphalt Concrete," Proc. 81st Transportation Research Board Annual Meeting, Washington.
- Kose, S., Guler, M., Bahia, H.U., and Masad, E. (2000). "Distribution of Strains within Asphalt Binders in HMA Using Image and Finite Element Techniques," J. Trans. Res. Record, No. 1728, National Research Council, Washington, D.C., 21-27.
- Masad, E. and Bahia, H. (2002). "Effect of Loading Configuration and Material Properties on Nonlinear Response of Asphalt Mixtures," *Journal of the Association of the Asphalt Paving Technologists*.
- Masad, E. Somadevan, N., Bahia, H.U., and Kose, S. (2001). "Modeling And Experimental Measurements of Strain Distribution in Asphalt Mixes," *Journal of Transportation Engineering*, 127(6), 477-485.
- Masad, E., Jandhyala, V.K., Dasgupta, N., Somadevan, N., Shashidhar, N. (2002). "Characterization of Air Void Distribution in Asphalt Mixes Using X-Ray Computed Tomography," *Journal of Materials in Civil Engineering*, Vol. 14, No. 2., pp 122-129.
- Masad, E., N. Somadevan, H.U. Bahia HU, and S. Kose (2001). "Modeling And Experimental Measurements of Strain Distribution In Asphalt Mixes," J. Trans. Res. Record, Vol 127, No. 6, National Research Council, Washington, D.C.
- Mora, P. (1992). "A Lattice Solid Model for Rock Rheology and Tectonics," *The Seismic Simulation Project Tech. Rep.*, Vol. 4, pp.3-28, Institut de Physique du Globe, Paris.
- Mustoe, G.G.W. and D.V. Griffiths (1998). "An Equivalent Model Using Discrete Element Method (DEM)," Proc. 12th ASCE Engineering Mechanics Conf., La Jolla, CA.

Papagiannakis, A.T., A. Abbas and E. Masad (2002). "Micromechanical Analysis of the Viscoelastic Properties of Asphalt Concretes," Proc. 81st Transportation Research Board Annual Meeting, Washington, D.C.

Rothenburg, L., Bogobowicz, A., and Hass, R. (1992). "Micromechanical Modelling of Asphalt Concrete in Connection with Pavement Rutting Problems," 7th International Conference on Asphalt Pavements, Vol. 1, pp. 230-245.

Sadd, M.H. and J.Y. Gao (1997). "The Effect of Particle Damage on Wave Propagation in Granular Materials," *Mechanics of Deformation and Flow of Particulate Materials*, Ed. C.S. Chang, A. Misra, R.Y. Liang and M. Babic, Proc. McNu Conference, Trans. ASCE, Northwestern Univ., pp.159-173.

Sadd, M.H., and J.Y. Gao (1998). "Contact Micromechanics Modeling of the Acoustic Behavior of Cemented Particulate Marine Sediments," Proc. 12th ASCE Engineering Mechanics Conf., La Jolla, CA.

Sadd, M.H., Dai, Q.L., Parameswaran, V., Shukla, A. (2004). "Microstructural Simulation of Asphalt Materials: Modeling and Experimental Studies," J. Matl. in Civil Engng., ASCE 16(2), 107-115.

Sepehr, K., O.J. Harvey, Z.Q. Yue and H.M. El Husswin. (1994) "Finite Element Modeling of Asphalt Concrete Microstructure, Proc. 3rd Intl. Conf. Computer-Aided Assessment and Control Localized Damage," Udine, Italy.

Stankowski, T. (1990). "Numerical Simulation of Progressive Failure in Particle Composites", Ph.D. Thesis, Univserity of Colorado.

Ullidtz, P. (2001). "A Study of Failure in Cohesive Particulate Media Using the Discrete Element Method," Proc. 80th Transportation Research Board Meeting, Washington, D.C.

Wang, L., H. Paul, T. Harman, J. D'Angelo, (2004). "Characterization of Aggregates and Asphalt Concrete Using X-ray Computerized Tomography," J. Assoc. Asphalt Paving Tech., Vol. 73, pp. 467-500.

You, Z. (2003). "Development of a Micromechanical Modeling Approach to Predict Asphalt Mixture Stiffness Using Discrete Element Method," Ph.D. dissertation of Department of Civil and Environmental Engineering at the University of Illinois at Urbana-Champaign, 512 pages, published by UMI, a Bell & Howell Information Company, Ann Arbor, MI, 2004.

You, Z. and Buttlar, W.G. (2002). "Stiffness Prediction of Hot Mixture Asphalt (HMA) Based upon Microfabric Discrete Element Modeling (MDEM)," Proc. of the 4th International Conference on Road & Airfield Pavement Technology, Vol. 1, pp. 409-417, People's Communications Publishing House, China.

You, Z. and Buttlar, W.G. (2004). "Discrete Element Modeling to Predict the Modulus of Asphalt Concrete Mixtures," Journal of Materials in Civil Engineering, ASCE, Vol. 16, Issue 2, pp. 140-146.

You, Z. and Buttlar, W.G. (2005). "Application of the Complex Modulus Measurements of Sand Mastic and Mixture," Journal of the Transportation Research Board, National Research Council, Washington, D.C.

AN EVALUATION OF THE STRESS NON-UNIFORMITY DUE TO THE HETEROGENEITY OF AC IN THE INDIRECT TENSILE TEST

Bing Zhang¹, Linbing Wang² and Mehmet T. Tumay³

ABSTRACT: Simple Performance Tests (SPT) including Indirect Tensile (IDT) Test and Dynamic Modulus Test have been widely used in the evaluation of the performance of asphalt concrete. The so-called SPT tests typically apply uniform stresses on the boundary and therefore obtain the stress-strain relation with convenience. Nevertheless, asphalt concrete is a heterogeneous material composed of asphalt binder, aggregates and air voids. The three constituents have drastically different stiffness. Even under a uniform boundary stress, the internal stress and strain distributions are not uniform. This paper presents a comparison between the stress distribution based on heterogeneous material properties and that based on homogeneous material properties using X-ray Computed Tomography (XCT) and Finite Element (FE) simulation. The comparison indicates that material heterogeneity is an important factor that must be considered in the characterization of asphalt concrete.

INTRODUCTION

Indirect Tensile (IDT) Test has been widely used to predict the fatigue performance of asphalt concrete. However the interpretation of the test is based on homogeneous elasticity. Historically the microstructure or the heterogeneity of the sample is not adequately reflected in detail for numerical simulation.

Various material models have been introduced to predict the behavior of asphalt concrete under both monotonic loading and cyclic loading. Schapery (1984) introduced a model by replacing physical strains with pseudo strains so that a viscoelastic problem can be transformed into an elastic problem through the correspondence principle. Work potential theory (Schapery 1990) was used in constitutive and evolution description based on pseudo stresses and strains. The change of stiffness of the material due to accumulative damage or healing was also taken into account. Both monotonic loading and cyclic loading were investigated using this theory by Park et al (1996), Lee (1998) and Zhang et al. (1997). Viscoplastic models were also introduced recently to describe the rate dependent plastic stress-strain relations of asphalt concrete. Collop et al (2003) implemented an elasto-viscoplastic constitutive model with damage for asphalt. It was formulated based on the generalized Burger's model: an elastic element in series with a viscoelastic element (linear Voigt) and a viscoplastic element (nonlinear). A power law function was assumed for the viscoplastic strain rate-stress relationship. Damage was accounted for by introducing parameters that modify the viscosity. Tashman et al

¹ Research Assistant, Louisiana State Univ., Dept. Civil and Environmental Engrg., Baton Rouge, LA 70803.

² Assistant Professor, Louisiana State Univ., Dept. Civil and Environmental Engrg., Baton Rouge, LA 70803, lwang@lsu.edu.

³ Georgia Gulf Distinguished Professor, Louisiana State Univ., Dept. Civil and Environmental Engrg., Baton Rouge, LA 70803.

(2005) developed a microstructural viscoplastic continuum model for asphalt concrete. The viscoplastic strain rate was defined using Perzyna (1966) flow rule and the linear Drucker-Prager yield function. The aggregate anisotropy was accounted for by introducing a microstructure tensor reflecting the orientation of nonspherical particles. Seibi et al (2001) used a Perzyna type viscoplastic constitutive model with isotropic hardening and Drucker-Prager yield criterion. Schwartz et al (2002) developed a model based on the extended viscoplastic Schapery continuum damage model. The model compared favorably with experimental measurements and it was concluded that the assumption of time-temperature superposition is valid for both viscoelastic and viscoplastic strain responses.

The literature indicates that asphalt concrete is controlled by viscoplastic response and dominated by plasticity that can be defined by Drucker-Prager criterion. However, these continuum models are based on homogeneous material properties derived from various experimental data on representative volumes or specimens. The microstructure is not considered in these models. In this study, the x-ray tomography technology was used to obtain the internal microstructure of the specimens. Image analysis method was developed to translate the acquired gray images into binary images to reconstruct the three dimensional (3D) microstructure that reflect the geometric configuration of voids, aggregates, and binder of the asphalt concrete specimens. This method can effectively reflect the discontinuous distribution of stresses, which is critical for damage incurrence.

This paper compares the theoretical solution for the IDT test with Finite Element Method (FEM) simulations, and evaluates whether a parameter, the stress concentration factor (Wang 2003) could capture the essential performance of asphalt concrete in terms of fatigue properties.

X-RAY TOMOGRAPHY IMAGING, ANALYSIS AND MICROSTRUCTURE MODEL

X-ray Tomography is a valid tool for quantifying the microstructure of asphalt concrete (Wang et al 2001; Masad et al 2002; Wang et al 2004). In this study, the asphalt concrete sample was scanned using x-ray tomography to obtain a series of gray image slices that reflect density variation of the major constituents such as asphalt binder, aggregates and voids (Figure 1). Calibration was carried out according to the density of the material the size of the sample. It is very important to obtain good images in the scanning process so that accuracy can be established from the very beginning. When multiple slices are stacked together they created a 3D visualization of the internal structure of the specimen. Several computer codes, using IDL (Interactive Data Language), were written to carry out the 3D reconstruction and quantification (illustrated in Figure 2). Through image processing, the series of images were transformed into a 3D data array that can be mapped into FEM elements. Voids and aggregates were identified by setting proper thresholds in the data array. The threshold values play a critical role in this process. The proper threshold value can be obtained through comparison between image measurements and the actual void content and/or aggregate volume fractions. After identification of the material components, proper material properties (such as elastic modulus and Poisson's ratio) can be assigned to the corresponding components. A FORTRAN program was written

to automatically generate the simulation model to implement this methodology. Three constituents, namely asphalt binder, aggregates and voids with different material properties were considered in the simulation to account for the different mechanical properties of them. With this method, only the binder is considered as a rate and temperature dependent material. Its characterization is simpler and requires much less time and effort. A statistical study with elastic material model for small strains was conducted here to study the relative effect of mix properties on the performance of asphalt concrete and validate whether the simulation method can capture the essential data to represent performance.

THEORETICAL SOLUTION FOR INDIRECT TENSILE TEST

Due to the geometry of the specimen and the loading characteristics of IDT, the stress and strain in the specimen during loading are complicated. The simplified theoretical solution for the plane stress condition along the horizontal and the vertical diameter is formulated as follows (Hondros, 1959):

Along the horizontal diameter:

$$\sigma_{11} = \frac{2P}{\pi aL} \left[\frac{\left(1 - \frac{x^2}{R^2}\right) \sin 2\alpha}{1 + 2\frac{x^2}{R^2} \cos 2\alpha + \frac{x^4}{R^4}} - \tan^{-1} \left(\frac{1 - \frac{x^2}{R^2}}{1 + \frac{x^2}{R^2}} \tan \alpha \right) \right]$$

$$\sigma_{22} = -\frac{2P}{\pi aL} \left[\frac{\left(1 - \frac{x^2}{R^2}\right) \sin 2\alpha}{1 + 2\frac{x^2}{R^2} \cos 2\alpha + \frac{x^4}{R^4}} + \tan^{-1} \left(\frac{1 - \frac{x^2}{R^2}}{1 + \frac{x^2}{R^2}} \tan \alpha \right) \right]$$

Along the vertical diameter:

$$\sigma_{11} = \frac{2P}{\pi aL} \left[\frac{\left(1 - \frac{y^2}{R^2}\right) \sin 2\alpha}{1 - 2\frac{y^2}{R^2} \cos 2\alpha + \frac{y^4}{R^4}} - \tan^{-1} \left(\frac{1 + \frac{y^2}{R^2}}{1 - \frac{y^2}{R^2}} \tan \alpha \right) \right]$$

$$\sigma_{22} = -\frac{2P}{\pi aL} \left[\frac{\left(1 - \frac{y^2}{R^2}\right) \sin 2\alpha}{1 - 2\frac{y^2}{R^2} \cos 2\alpha + \frac{y^4}{R^4}} + \tan^{-1} \left(\frac{1 + \frac{y^2}{R^2}}{1 - \frac{y^2}{R^2}} \tan \alpha \right) \right]$$

Where P is the magnitude of the applied force, a is the width of the loading plate, L and R are the length and radius of the cylinder, respectively, and σ_{11} and σ_{22} are the direct stresses in the horizontal and vertical directions, respectively.

The 3D solution was formulated with a potential function by Wijk (1978). However, it is more complicated and is close to the plane stress solution. The influence of the loading plate stiffness and geometry is in the vicinity of the plate only (Zhang, 1997). For our case, the thickness of the model was very small. Therefore the above

equations were used to draw the stress distribution of the specimen for the purpose of comparison.

FEM MODEL CONSTRUCTION

A FEM model geometry (Figure 3) was built to reflect the actual microstructure of specimens from the WesTrack project (Epps et. al, 1997). By importing the three dimensional data obtained from image analysis and reconstruction, the elements representing aggregates and voids were grouped and separated from the elements representing binder or mastics. Element groups representing aggregates and asphalt binders were assigned different elastic material properties while the element group for voids was removed during the loading steps. In this study, all the non-voids components were assigned elastic properties that may represent the behavior of the binder at low temperature and small loading magnitude. The result of the FEM simulation was compared with the analytical elastic solution to verify the accuracy of FEM simulation so that proper mesh size could be determined. Due to the large memory and disk space requirement of the simulation, all the images with 512×512 resolution were transformed into 100×100 resolution and the volume fractions of the constituents were maintained. In addition to stresses, strains, and displacements that result from the FEM simulation, the stress concentration factor (the ratio between the largest tensile stress and that of the elastic solution assuming homogeneity) was also computed. The stress concentration factor is a comprehensive indicator of the rationality of the material structure. To validate these concepts, the three mixtures of the WesTrack project (the fine mix, the fine plus mix, and the coarse mix) were evaluated using the procedure developed.

RESULTS AND DISCUSSIONS

Due to the existence of aggregates and voids in the mixture, the stress distribution no longer follows that of either the theoretical elastic solution or the FEM solution assuming homogeneity of the material.

The typical stress distributions along vertical and horizontal diameter for these three samples are plotted in Figure 4 through Figure 6. It can be seen that the coarse mix had the largest stress variations, followed by the fine plus mix and the fine mix. It should be noted that the performance of the mixes followed the same order (from poor to good).

The analytical solution for the IDT test model used in the FEM simulation was calculated and illustrated in Figure 7. While assigning the same property for aggregate and asphalt binder, the two-constituent FEM model yields a solution that agrees well with the analytical elastic solution in the average sense.

By comparing the stress distributions of the FEM simulations that include voids, aggregates and binder and those of the analytical solution, one can obtain the stress concentration factor conveniently. It is found that the fine mix sample had the least stress concentration while the coarse mix showed the largest stress concentration (See Figure 8). However, the stress concentrations are similar if voids were not removed, indicating the importance of void structure on the behavior of the mixture. In the calculation of the average stress (needed for calculating the stress concentration factor), the stresses along the 20mm and the 80 mm position (with a height of 60mm)

were averaged to avoid the local effect in the vicinity of the loading plate. The results are tabulated in Table 1. The result may imply that the fine mix will have the best performance, which was observed in the field experiment.

The simulations are for thin disks. Generally, the stress distribution for all fine mix specimens (thin disks) is consistent. The same is true for the coarse mix specimens and the fine plus mix specimens, indicating that thin disks may be used for simulations to reduce memory and time requirements. In order to verify the statistical consistency of the simulations, simulations for ten different pieces were performed for each mixture. The average stress and its standard deviations were collected for every simulation. The results (Table 2 to Table 4) show that for every sample (a mix), the consistency is good and therefore the solutions were distinguishable among the three mixtures of the WesTrack project.

The variation of stress distribution due to the different ratios between the elastic modulus of aggregates and that of asphalt binder was also studied by comparing simulation results of samples with 1:1 ratio (aggregate modulus to binder or mastic modulus) up to 100:1 ratio. The results were plotted in Figure 9 for stresses along vertical and horizontal diameters respectively. It can be seen that large difference in constituent properties will lead to significant stress concentration even if there were no voids presented. This indicates that the relative stiffness between aggregates and the asphalt binder (or mastics) plays an important role in the mixture performance. It also implies that the damage may become more significant due to a softer binder or mastics. It should be noted that for the simulations with E ratio of 20:1 and 100:1, a more refined mesh might be needed to catch the accurate stress distribution and hence stress concentration.

CONCLUSIONS

This paper presents an evaluation of the non-uniform stress distribution effect on IDT test. The stress concentration varies significantly with the void distribution and the relative stiffness between aggregate and binder. IDT test should be combined with FEM simulation to offer better interpretation of the test results. The stress concentration factor may serve as a good simple performance indicator.

ACKNOWLEDGEMENT

This study is based upon work supported by the National Science Foundation under Partnership for Innovation Grant No. 0438480. Any opinions, findings, and conclusions or recommendations expressed in this material are those of the authors and do not necessarily reflect the views of the National Science Foundation

REFERENCES

- Collop, A. C., Scarpas, A., Kasbergen, C, and Bondt A. (2003). "Development and finite element implementation of a stress dependent elasto-visco-plastic constitutive model with Damage for Asphalt." *TRB 2003 Annual Meeting CD-ROM*.
- Epps, J., Monismith, C.L, Alavi, S.H, Mitchell, T.M. (1997). WesTrack Full-Scale Test Track: Interim Findings. http://www.westrack.com/wt_04.htm

- Hondros, G. (1959). "Evaluation of Poisson's Ratio and the Modulus of Materials of a Low Tensile Resistance by the Brazilian (Indirect Tensile) Test with Particular Reference to Concrete." *Australia Journal of Applied Science*, 10(3), 243-268.
- Lee, H.J. and Y.R. Kim (1998a). "A Uniaxial Viscoelastic Constitutive Model for Asphalt Concrete under Cyclic Loading." *ASCE J. Engrg. Mech.*, 124(11), 1224-1232.
- Lee, H.J. and Y.R. Kim (1998b). "A Viscoelastic Continuum Damage Model of Asphalt Concrete with Healing." *ASCE J. Engrg. Mech.*, 124(11), 1-9.
- Masad, E; Jandhyala, VK; Dasgupta, N; Somadevan, N; Shashidhar, N (2002). "Characterization of Air Void Distribution in Asphalt Mixes Using X-Ray Computed Tomography." *J. Mat. Civil Engrg.*, 14(2), 122-129.
- Park, S.W. Y.R. Kim, and R.A. Schapery (1996). "A Viscoelastic Continuum Damage Model and Its Application to Uniaxial Behavior of Asphalt Concrete." *Mechanics of Materials*, 24(4), 241-257.
- Perzyna, P. (1966). "Fundamental problems in viscoplasticity." *Advances in Applied Mechanics*, 9, 243-377.
- Schapery, R.A. (1984). "Correspondence principles and a generalized J-integral for large deformation and fracture analysis of viscoelastic media." *Int. J. Fract.*, 25, 195-223.
- Schapery, R.A. (1990). "A Theory of Mechanical Behavior of Elastic Media with Growing Damage and Other Changes in Structure." *J. Mech. Phys. Solids*, 38, 215-253.
- Schwartz, C.W., Gibson, N.H., Schapery, R.A., and Witczak, M.W. "Viscoplasticity Modeling of Asphalt Concrete Behavior." Recent Advances in Material Characterization and Modeling of Pavement Systems (Tutumluer, E., Masad, E., and Najjar, Y., ed.), *Geotechnical Special Publication 123*, ASCE, 144-159.
- Seibi, A. C., Sharma, M. G., Ali, G. A., and Kenis, W. J. (2001). "Constitutive relations for asphalt concrete under high rates of loading." *Transportation Research Record*, 1767, 111-119.
- Tashman, L., Masad, E., Zbib, H., Little, D., and Kaloush, K. (2005). "microstructural viscoplastic continuum model for permanent deformation in asphalt pavements." *Journal of Engineering Mechanics*, ASCE, 131(1), 48-57.
- Wang, L.B., Frost, J.D. and Shashidhar, N. (2001). "Microstructure Study of Westrack Mixes from X-ray Tomography Images." *TRR No.1767*, 85-94.
- Wang, L.B. (2003). "Stress Concentration Factor of Poroelastic Material by FEM Simulation and X-ray Tomography Imaging." *ASCE Engineering Mechanics Conference*, Seattle, WA.
- Wang, L.B., Harold S. Paul, Thomas Harman and John D' Angelo (2004). "Characterization of Aggregates and Asphalt Concrete using X-ray Tomography." *AAPT*, 73, 467-500.
- Wijk, G. (1978), "Some New Theoretical Aspects of Indirect Measurements of the Tensile Strength of Rocks." *Int. J. Rock Mech. Min. Sci. & Geomech. Abstr.*, 15, 149-160.
- Zhang, W. and Drescher, A. and Newcomb, D. E. (1997). "Viscoelastic Analysis of Diametral Compression of Asphalt Concrete." *Journal of Engineering Mechanics*, 123(6), 596-603.

Table 1 Stress concentration of the three WesTrack mixtures

Mixture	Phases ¹	Average	Maximum	S.C.F. ²
Fine	2	0.0363	0.0658	1.81
	3	0.0333	0.0728	2.18
Fine Plus)	2	0.0337	0.0641	1.90
	3	0.0362	0.1985	5.48
3(Coarse)	2	0.0313	0.0676	2.16
	3	0.0354	0.2144	6.05
Theoretical solution		0.0364	0.0375	1.03

¹ 2 phases: binder+voids, aggregates

3 phases: aggregates, binder, voids

² Stress concentration factor.

Table 2 Stress statistic study for the fine-mix sample

Segment	before void removal			after void removal		
	Average	Maximum	S.C.F.	Average	Maximum	S.C.F.
1	0.03638	0.06577	1.81	0.03499	0.06840	1.95
2	0.03591	0.04486	1.25	0.03108	0.04284	1.38
3	0.03647	0.05088	1.40	0.03236	0.07280	2.25
4	0.03738	0.06138	1.64	0.03077	0.05027	1.63
5	0.03639	0.06064	1.67	0.02723	0.04643	1.71
6	0.03715	0.05797	1.56	0.04224	0.07277	1.72
7	0.03665	0.05287	1.44	0.03879	0.05836	1.50
8	0.03590	0.06026	1.68	0.03510	0.06213	1.77
9	0.03493	0.05057	1.45	0.02866	0.04429	1.55
10	0.03576	0.06429	1.80	0.03200	0.05744	1.79
STDEV	0.07%	0.68%	18.24%	0.46%	1.14%	24.61%

Table 3 Stress statistic study for the fine-plus mix sample

Segment	before void removal			after void removal		
	Average	Maximum	S.C.F.	Average	Maximum	S.C.F.
1	0.03519	0.05505	1.56	0.03931	0.07033	1.79
2	0.03331	0.05491	1.65	0.01387	0.03542	2.55
3	0.03452	0.05704	1.65	0.03694	0.08786	2.38
4	0.03328	0.06415	1.93	0.04403	0.16453	3.74
5	0.03161	0.05040	1.59	0.02370	0.12659	5.34
6	0.03287	0.05068	1.54	0.04236	0.10995	2.60
7	0.03365	0.05140	1.53	0.03826	0.19846	5.19
8	0.03327	0.05574	1.68	0.04221	0.10105	2.39
9	0.03532	0.05204	1.47	0.04277	0.12222	2.86
10	0.03403	0.05656	1.66	0.03864	0.10459	2.71
STDEV	0.11%	0.41%	12.51%	0.97%	4.58%	121.38%

Table 4 Stress statistic study for coarse-mix sample

Segment	before void removal			after void removal		
	Average	Maximum	S.C.F.	Average	Maximum	S.C.F.
1	0.03312	0.05041	1.52	0.04467	0.10635	2.38
2	0.03398	0.06763	1.99	0.03856	0.18578	4.82
3	0.03186	0.04622	1.45	0.02858	0.10865	3.80
4	0.03352	0.05181	1.55	0.03000	0.09078	3.03
5	0.03178	0.04507	1.42	0.02636	0.11865	4.50
6	0.03021	0.05118	1.69	0.03716	0.16080	4.33
7	0.02723	0.04594	1.69	0.04396	0.21444	4.88
8	0.03121	0.05546	1.78	0.03292	0.13823	4.20
9	0.03018	0.04060	1.35	0.03666	0.16088	4.39
10	0.02968	0.05724	1.93	0.03563	0.12001	3.37
STDEV	0.20%	0.77%	21.72%	0.61%	3.93%	81.57%

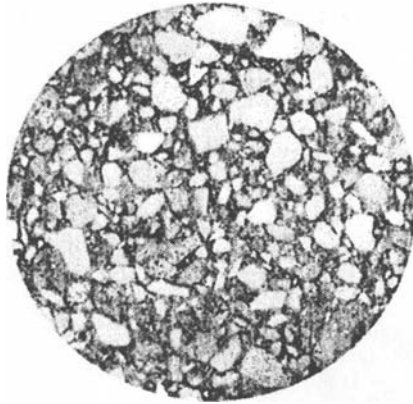


Figure 1 Gray image from x-ray scan

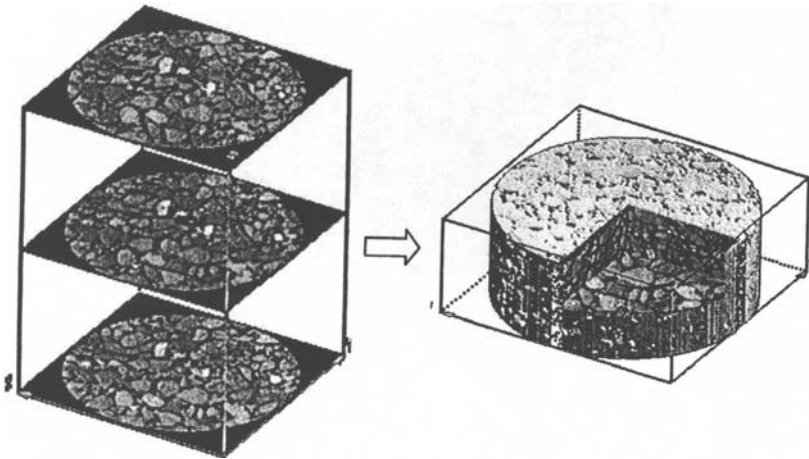


Figure 2 Reconstruction of three-dimensional microstructure

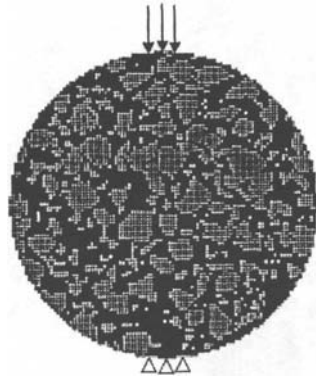


Figure 3 Three dimensional FE model

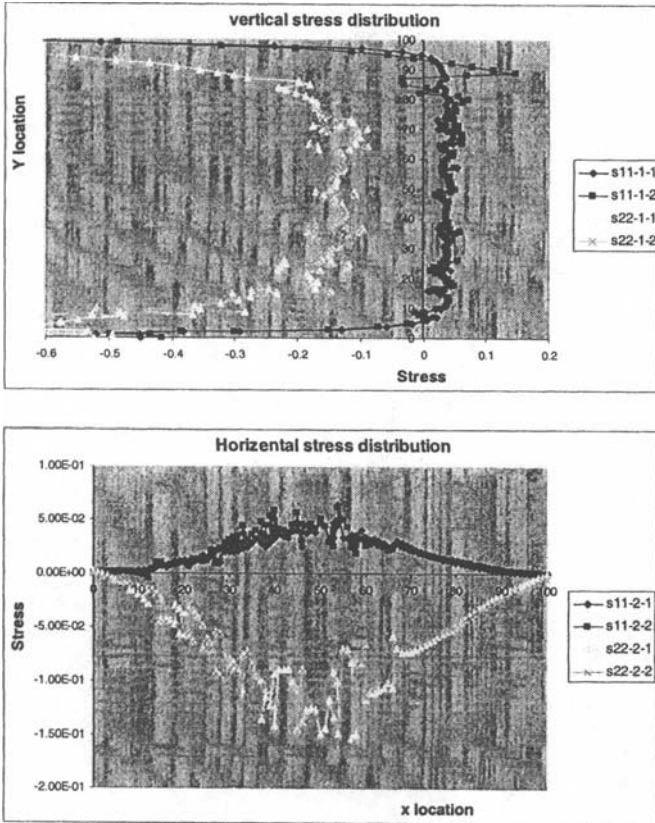


Figure 5 Stresses distribution for the fine-plus mix sample

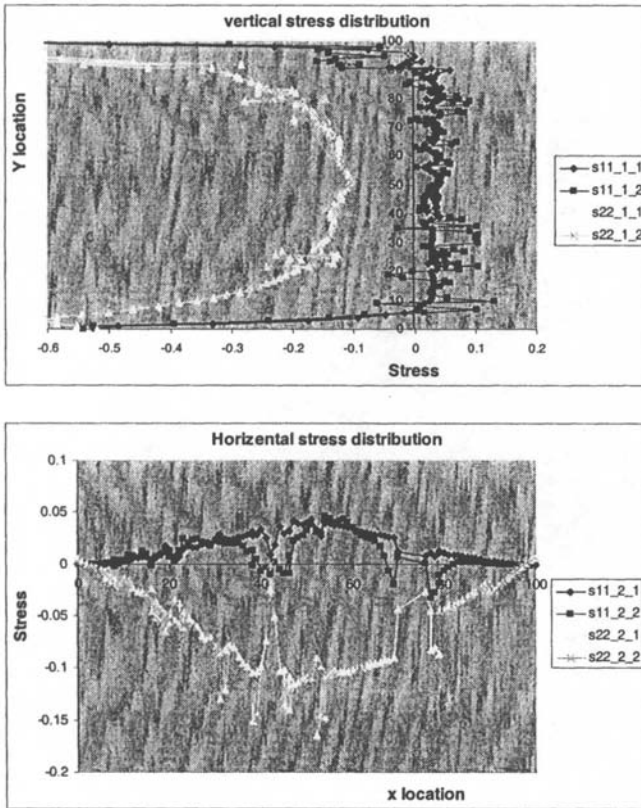


Figure 6 Stresses distribution for coarse-mix sample

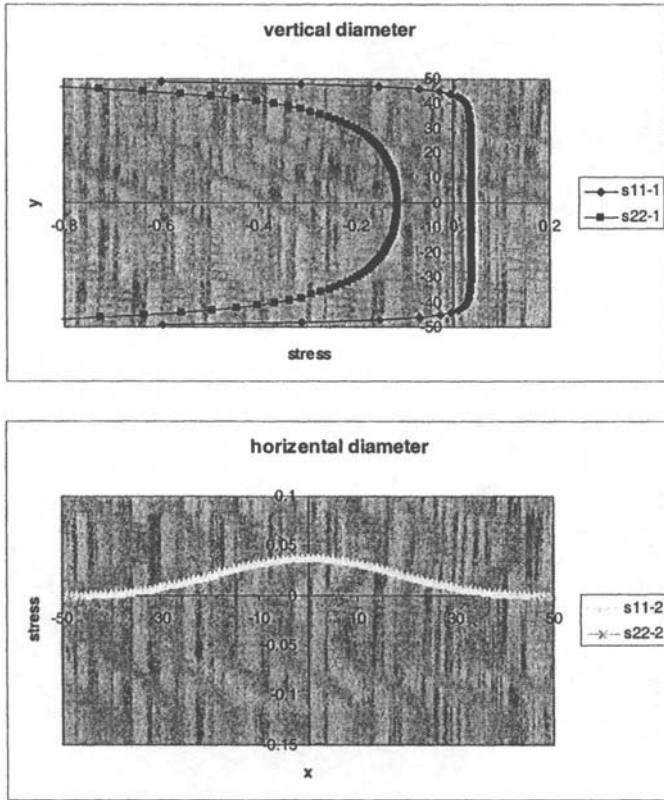


Figure 7 Stresses distribution along sample diameters (theoretical solution)

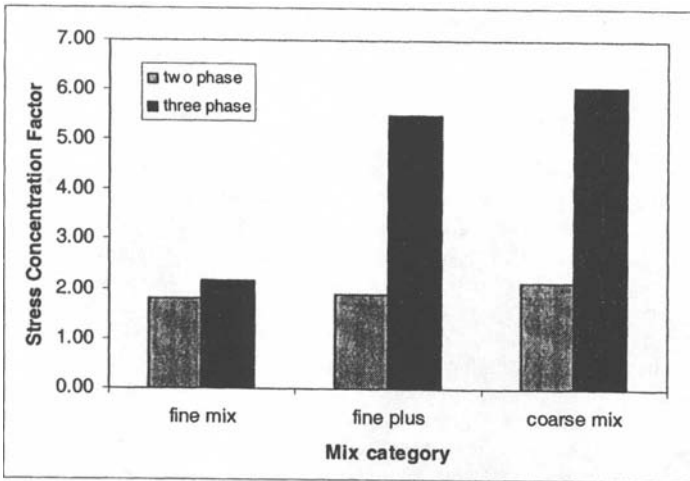
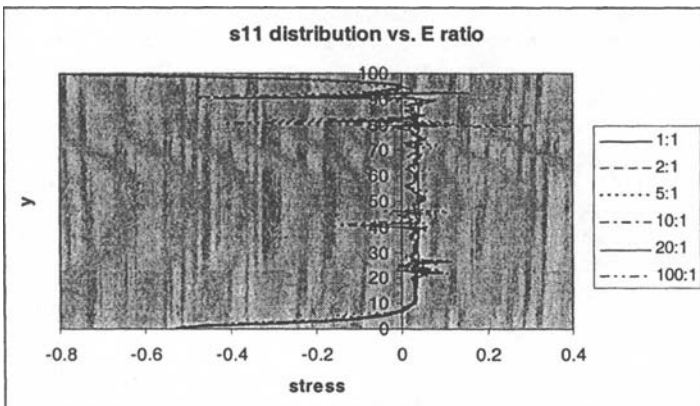


Figure 8 Stress concentration comparison



Note: s11 along vertical diameter with voids removed

Figure 9 Stress distribution for different E ratios

The Development of a Microstructural-Based Continuum Model for Hot Mix Asphalt

Samer H. Dessouky¹, Eyad A. Masad², Geo-Institute Member

ABSTRACT: Permanent deformation is one of the primary distresses in hot mix asphalt (HMA). It is influenced by the properties of the mix constituents including microstructural features such as aggregate directional distribution (anisotropy), and damage. Conventional continuum constitutive models do not explicitly consider the influence of microstructure distribution on the macroscopic response. The main objective of this paper is to develop an elasto-visco-plastic continuum model that accounts for aggregate directional distribution and damage. This is accomplished by modifying the Drucker-Prager yield function to account for these microstructural features. This yield function is incorporated into Perzyna's viscoplastic flow function. The model is implemented in finite element (FE) using an implicit numerical integration algorithm. FE analysis is conducted to study the influence of key factors such as anisotropy and damage on the model response. In addition, the FE model is used to simulate the response of HMA to compressive and extension triaxial tests at different loading rates and confining pressures, and the numerical results are compared to experimental measurements.

KEYWORDS: HMA, Microstructure, Anisotropy, Modeling, Finite Element

INTRODUCTION

Permanent deformation is one of the most serious problems for asphalt pavement highways and runways in the United States. It manifests itself as depressions along the wheel paths. This study is an effort to develop a constitutive model that account for the microstructure distribution, and can be used to predict permanent deformation.

The model presented in this paper builds on the formulation developed by Tashman et al. (2005), but it is expanded to include the elastic response of the material, and the influence of stress state. In addition, the procedure to account for anisotropy in the constitutive relationship is further simplified from that developed by Tashman et al. (2005). The continuum model is assumed to have an elastic recoverable component and a viscoplastic irrecoverable component associated with permanent deformation. Hooke's law is employed to account for the elastic component, while a modified Drucker-Prager yield surface defined in nonassociated Perzyna's formulation is utilized to account for the viscoplastic component. The continuum model is implemented in the FE ABAQUS package through a user-defined material subroutine. In summary, the new model accounts for the following mechanisms that are associated with permanent deformation:

- Elastic response prior to reaching the yielding stress threshold;
- Shear as the dominant stress causing permanent deformation;

¹Grad. Student, Dept. of Civil Eng., Texas A&M University, College Station TX 77843 dsamer@tamu.edu

²Asst. Prof. Dept. of Civil Eng., Texas A&M University, College Station TX 77843 emasad@civil.tamu.edu

- Dilation and hydrostatic pressure dependency of the material;
- Stress path dependency of the viscoplastic response;
- Work hardening/softening of the material;
- Aggregate directional distribution in the microstructure; and
- Damage in terms of cracks and air voids.

CONTINUUM MODEL DEVELOPMENT

The material response is assumed to have an elastic recoverable component and a viscoplastic irrecoverable component at relatively high temperatures associated with permanent deformation. The total strain increment $\Delta \epsilon$ is decomposed into elastic and viscoplastic components:

$$\Delta \epsilon_{ij} = \Delta \epsilon_{ij}^e + \Delta \epsilon_{ij}^{vp} \quad (1)$$

where the superscript (e) refers to the elastic part and (vp) refers to the viscoplastic part. Perzyna's flow rule incorporates an overstress function and a fluidity parameter that relate the rate of viscoplastic strain to the current stresses and loading history. Analogous to the classical theory of incremental plasticity, the viscoplastic strain rate is computed by means of postulated flow rules. The stress-strain relationship for time increment Δt is shown in Eq. (2):

$$\Delta \sigma_{ij} = D_{ijkl} \left(\Delta \epsilon_{kl} - \Gamma \cdot \langle \phi(f) \rangle \cdot \frac{\partial g}{\partial \sigma_{kl}} \cdot \Delta t \right) \quad (2)$$

where $\Delta \sigma$ is the stress increment tensor and D is the fourth-order elastic stiffness matrix. $\Gamma \cdot \langle \phi(f) \rangle$ specifies the magnitude of the vector $\Delta \epsilon^{vp}$, Γ is a fluidity parameter, and ϕ is an overstress function that is typically taken as a power function of the yield surface f . g is a viscoplastic potential surface that controls the direction of the viscoplastic strain increment. " $\langle \cdot \rangle$ " are McCauley brackets which imply that $\dot{\epsilon}^{vp}$ starts taking place only if $\phi > 0$ and it is zero otherwise.

To account for the factors associated with the mechanism of permanent deformation discussed previously, an extended Drucker-Prager yield function is employed in the form:

$$f = \tilde{f}(I_1, J_2, J_3, \alpha, d, \Delta, \xi) - \kappa = 0 \quad (3)$$

where I_1 , J_2 and J_3 are the first stress invariant, second deviatoric stress invariant, and third deviatoric stress invariant, respectively. These invariants account for the effect of confinement, shear stresses associated with viscoplastic deformation, and stress state. d is a parameter that reflects the influence of the stress path direction on yielding, which is equal to the tensile yield stress to compressive yield stress at a given confinement level. Δ is referred to as the vector magnitude, and it accounts for the influence of the material anisotropy. ξ is a damage parameter that accounts for the evolution of cracks and air voids. α is a parameter that reflects the material frictional

behavior, and κ is a hardening parameter that describes the cohesive and frictional characteristics of HMA. The extended Drucker-Prager model is presented in Eq. (4):

$$f = \bar{\tau}^e - \alpha \bar{I}_1^e - \kappa \quad (4)$$

where

$$\bar{I}_1^e = \frac{1}{3(1-\xi)} \cdot \bar{\sigma}_{ii} \quad (5)$$

$$\bar{\tau}^e = \frac{\sqrt{J_2}}{2(1-\xi)} \left[1 + \frac{1}{d} + \left(1 - \frac{1}{d} \right) \frac{J_3}{J_2^{3/2}} \right] \quad (6)$$

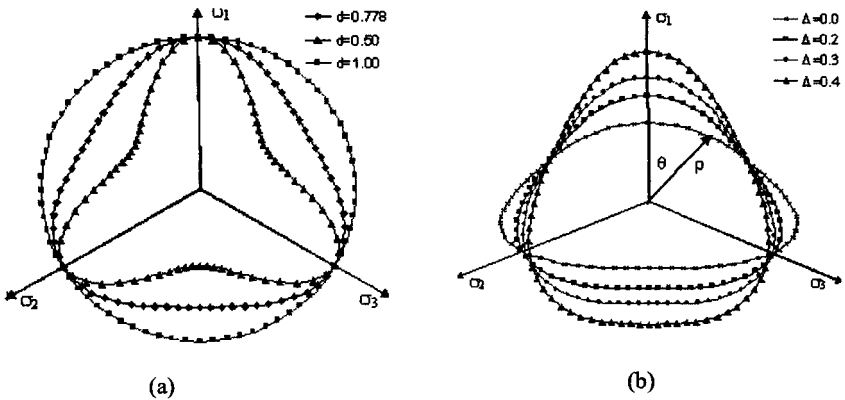
The effective stress $\bar{\sigma}_{ij}$ accounts for both the stress magnitude and anisotropy as shown in Eq. (7) (Tobita 1989, Dessouky 2005):

$$\bar{\sigma}_{ij} = \frac{3}{2} [\sigma_{ik} F_{kj} + F_{ik} \sigma_{kj}] \quad (7)$$

where the microstructure tensor, F_{ij} , is a function of Δ which is measured using image analysis of two-dimensional vertical sections of HMA specimens. The Δ value is equal to unity when all aggregates are oriented in the same direction, and is equal to zero for isotropic distribution. In HMA, Δ is typically between zero and 0.5 (Tashman et al. 2005). The plastic potential function g is taken to have the same form as the yield function in Eq. (4), but it has a slope equal to β instead of α .

In uniaxial compression and $\xi = 0$, Eq. (6) indicates that $\frac{J_3}{J_2^{3/2}} = 1$ and $\bar{\tau} = \sqrt{J_2}$,

while $\bar{\tau} = \frac{\sqrt{J_2}}{d}$ in uniaxial tension. To ensure convexity of the yield surface d ranges between 0.778 and 1. A d value less than 1 indicates that the strength of the material in tension is lower than that in compression as shown in Fig. 1. When $d = 1$, the dependence on the third deviatoric stress invariant vanishes and the Misses circle is recovered in the deviatoric plane. The effect of the anisotropy parameter Δ on the shape of the yield surface is also shown in Fig. 1. The results in this figure indicate that the anisotropy parameter causes the yield stress to be dependent on the direction of loading. For example, the compression yield stress at plane $\theta = 0^\circ$ is different from that corresponding to plane $\theta = 120^\circ$. Also, the yield stress in the axial direction perpendicular to the preferred orientation of particles (direction 1) increases as the material anisotropy increases, while very small change in stress is recorded for the radial direction (directions 2 and 3).



$$\bar{\tau}^e = \frac{\sqrt{J_2}}{2(1-\xi)} \left[1 + \frac{1}{d} + \left(1 - \frac{1}{d} \right) \frac{J_3}{J_2^{3/2}} \right]$$

Fig. 1. Shape of the Yield Surface in the Principal Stresses Plane as a Function of *d* and Δ .

EFFECT OF ANISOTROPY ON MATERIAL DILATION

The anisotropic distribution of particles affects the relative sliding of particles, and hence it influences the dilation of granular materials. The relationship between anisotropy and dilation has been studied experimentally by several researchers (e.g., Oda 1972). This section offers an analytical derivation of the relationship between anisotropy and dilation.

Consider β which is the slope of the potential surface. The parameter (β^*) which is a function the ratio of the volumetric strain rate $\dot{\epsilon}_v^{vp}$ to the deviatoric strain rate $\dot{\epsilon}_d^{vp}$ can be shown to be (Dessouky 2005):

$$\beta^* = -\frac{\dot{\epsilon}_v^{vp}}{\dot{\epsilon}_d^{vp}} = -\frac{\dot{\epsilon}_{11}^{vp} + 2\dot{\epsilon}_{33}^{vp}}{3(\dot{\epsilon}_{11}^{vp} - \dot{\epsilon}_{33}^{vp})} = 3 \cdot \frac{\beta + \Delta \left(\frac{2}{d} + \frac{\beta}{3} \right)}{\frac{3}{d} - \Delta \left(\frac{1}{d} - \frac{4}{3} \beta \right)} \tag{8}$$

where for an isotropic material ($\Delta = 0$) and $d = 1$, β^* is equal to β .

Figure 2. shows the relationship between β^* and β . It can be seen that dilation increases with an increase in anisotropy represented by the Δ value. This is an important finding, as it agrees with the experimental measurements made by other researchers on granular materials. For example, Oda (1972) found that maximum dilation occurred when the preferred orientation of particles coincided with the

horizontal direction and the major principal stress was imposed in the vertical direction.

The dilation parameter β can be determined experimentally from a triaxial test using the ratio of lateral and uniaxial viscoplastic strain rate as follows:

$$\frac{\dot{\epsilon}_{33}^{VP}}{\dot{\epsilon}_{11}^{VP}} = \frac{\left(\frac{\partial g}{\partial \sigma_{33}}\right)}{\left(\frac{\partial g}{\partial \sigma_{11}}\right)} = -\frac{(1+\Delta)}{(1-\Delta)} \cdot \frac{\left(\frac{1}{2d} + \frac{\beta}{3}\right)}{\left(\frac{1}{d} - \frac{\beta}{3}\right)} \quad (9)$$

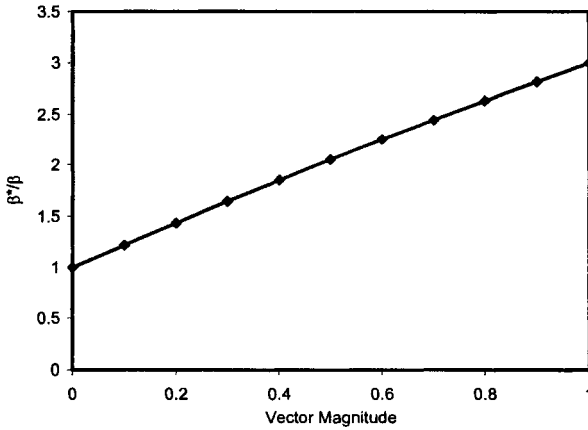
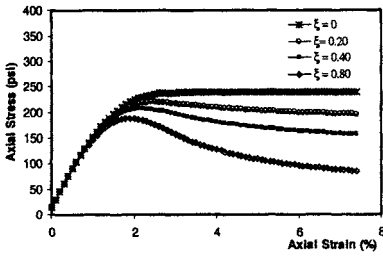


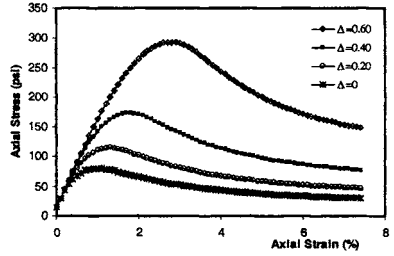
Fig. 2. Relationship between Dilation Parameter and Anisotropy for $d = 1$.

PARAMETRIC ANALYSIS

The model is implemented in FE analysis by using an implicit numerical integration algorithm, called Euler backward method, carried out in a time-step control. The equations that govern the evolution of stress, internal variables, inelastic deformation, and nonlinear parameters are discretized in an incremental format in a user defined material subroutine (UMAT) in the ABAQUS package. The FE analysis is used to conduct a parametric study to illustrate the efficiency of the developed constitutive relationship in capturing key features of the behavior of HMA. The parametric analysis results in Fig. 3 show the effects of the microstructure parameters Δ and ξ on the stress-strain relationship. The damage parameter is shown to influence the reduction in stress in the softening zone once the material past ultimate stress (Fig. 3a). As shown in Fig. 3b, the compressive strength in the axial direction, which is perpendicular to the preferred orientation of particles, increases with an increase in Δ .



a) Influence of ξ on Viscoplastic Deformation



b) Influence of Δ on Viscoplastic Deformation

Fig. 3. Examples of The Effects of Damage Parameter ξ and Anisotropy Parameter Δ on the Stress-Strain Response.

EXPERIMENTAL ANALYSIS AND RESULTS

Triaxial compression tests were conducted on four-inch diameter HMA specimens of gravel aggregate and PG 64-22 binder at strain rates of 0.0660%/min, 0.318%/min, 1.60%/min, 8.03%/min, and 46.4%/min, and at confining pressures of 0 psi, 15 psi, and 30 psi (Masad et al. 2003). In addition, triaxial extension tests were conducted on this mix using strain rates of 0.0660%/min, 0.318%/min and 1.60%/min and confining pressures similar to those used in the compression tests. Axial and radial stresses and strains were recorded throughout testing. Specimens were loaded up to an axial strain of 8 percent or until failure, whichever occurred first.

The data analysis has revealed that damage evolution is a function of confining pressure and effective viscoplastic strain ϵ_{vp} . An exponential form has been used to simulate the softening response as the material passes the ultimate stress (Eq. 10). The function in Eq. (10) can be shown to be equivalent to the one proposed by Desai (1998).

$$\xi = \exp(\xi_1 \cdot \frac{I_1}{3}) \cdot \left[1 - \exp(\xi_2 \cdot \epsilon_{vp} + \xi_3 \cdot \frac{I_1}{3}) \right] \quad (10)$$

In Eq. (10), ξ_1 , ξ_2 , and ξ_3 are coefficients that can be determined experimentally from the softening part of the stress-strain curve. The first exponential term controls the asymptotic limit of the function, while the last term, which includes the confining pressure, controls the damage rate of growth.

The experimental measurements indicated that α tends to change only at small strain levels, while the evolution of κ is more pronounced as shown in Fig. 4. Therefore, α is assumed to be constant. The evolution of κ is associated with hardening resulting from binder deformation and changes in aggregate structure. Hence, it is proposed to account for the evolution of the hardening parameter κ , as shown in Eq. (11):

$$\kappa = \kappa_0 + \kappa_1 \{1 - \exp(-\kappa_2 \cdot \epsilon_{vp})\} \tag{11}$$

where κ_0 defines the initial yield surface and κ_1 and κ_2 are material coefficients that account for the effect of effective viscoplastic strain on the material work hardening.

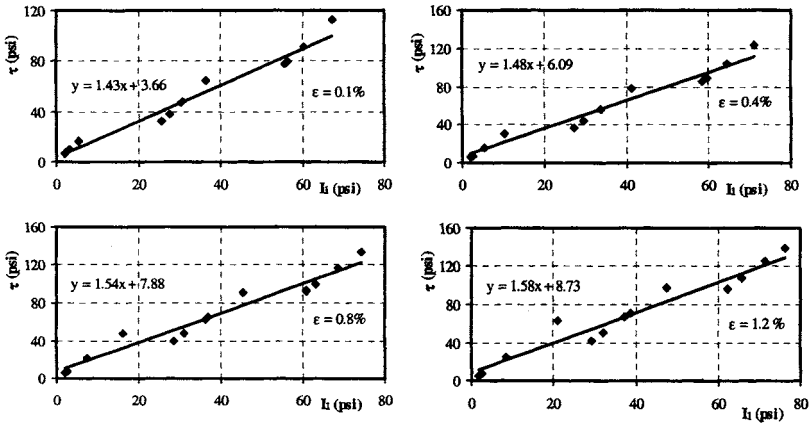


Fig. 4. Evolution of α and κ at Different Deformation Levels

Figure 5 shows compressive and extension testing data and FE model results. Each curve represents an average of two replicates. Higher strengths were associated with higher strain rates and/or confining pressures. The same parameters were used for the compression and extension tests except for the damage function parameters. This can be attributed to the fact that extension loading promotes opening of cracks and softening behavior in the binder phase, while damage in compression tests is associated with sliding of particles that occurs after some hardening behavior. The FE results overestimated the tensile strength compared with the experimental measurements. However, similar to the experimental results, the FE simulation results showed that tensile strength was much lower than compressive strength, and that the extension results were much less influenced by confining pressure and strain rate compared with the compression test results.

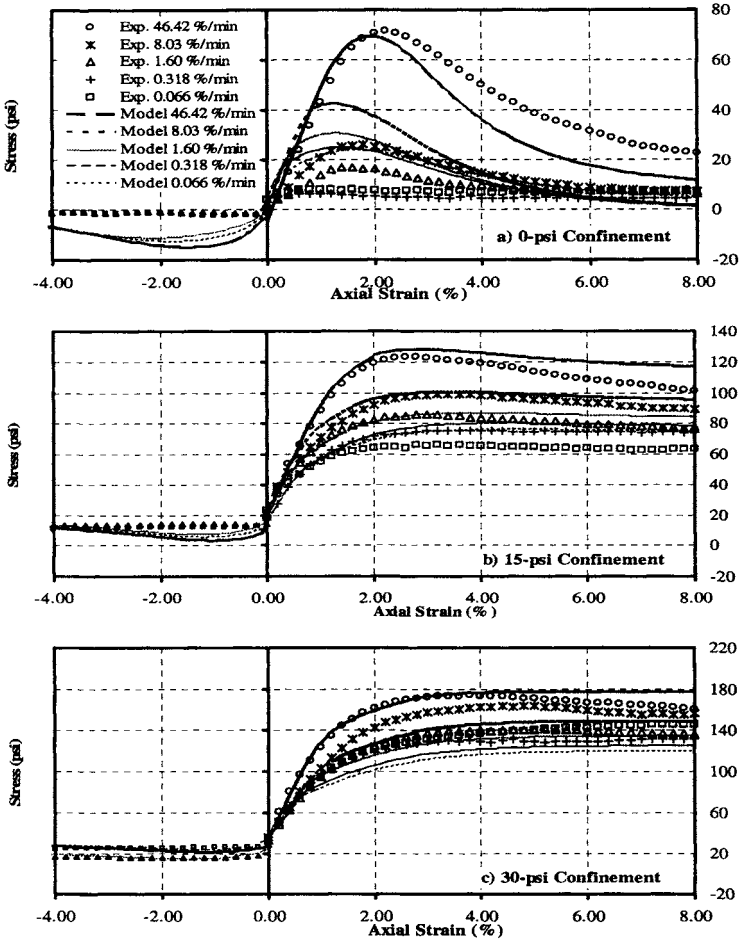


Fig. 5. Compression and Extension Experimental Measurements and Finite Element Results for Gravel Mixes

SUMMARY

This study presented the development of an elasto-visco-plastic continuum model to predict HMA response and performance. The model includes microstructure parameters that capture the directional distribution of aggregates and damage. In addition, the model is capable to account for the factors affecting the mechanisms of permanent deformation such as shear stress, aggregate structure friction and dilation, confining pressure, strain rate, and stress state.

The elasto-visco-plastic model was implemented in FE. A parametric study was conducted to investigate the effect of key model parameters on the material response. The results show clearly that the model response is sensitive to HMA anisotropy (Δ) and damage (ξ). Triaxial compression and extension strength tests were conducted at different loading rates and confining pressures. Similar to the experimental measurements, the FE results indicated that tensile strength of the mix was much lower than compressive strength. The damage parameters used in simulating the extension tests were different than those used in the compression tests, because softening in extension test occurs earlier and at a faster rate than in compression.

REFERENCES

- ABAQUS (2004). *User's and Theory Manuals*, versions 6.4, Hibbit, Karlsson & Sorensen Inc., Pawtucket, RI.
- Desai S. (1998). "Review and evaluation of constitutive models for pavement materials." Report submitted to SUPERPAVE, University of Maryland, College Park, MD.
- Dessouky, S. (2005). *Multiscale Approach for Modeling Hot Mix Asphalt*, Ph.D. Dissertation, Department of Civil Engineering, Texas A&M University, College Station, TX.
- Masad, E., Little, D., Tashman, L., Saadeh, S., Al-Rousan, T., and Sukhwani, R. (2003). *Evaluation of Aggregate Characteristics Affecting HMA Performance*. Research Report ICAR 203-1, Texas Transportation Institute, College Station, TX.
- Oda, M. (1972). "Initial fabrics and their relations to mechanical properties of granular materials." *Soils Foundation*, 12(1), 17-36.
- Tashman, L., Masad, E., Zbib, H., Little, D. and Kaloush, K. (2005). "Microstructure viscoplastic continuum model for permanent deformation in asphalt pavements." *Journal of Engineering Mechanics*, 131(1), 48-57.
- Tobita, Y. (1989). "Fabric tensors in constitutive equations for granular materials," *Soils and Foundations*, 29(4), 99-104.

DEVELOPMENT OF A COMPUTATIONAL MODEL FOR ASPHALTIC CONCRETE RESPONSE UNDER CYCLIC LOADING

Edwin Swart^{1,2}, Tom Scarpas² and Xueyan Liu²

ABSTRACT: When traffic load is imposed on a pavement, a non-uniform displacement field develops giving rise to a multitude of triaxial states of stress. Triaxiality has been known to significantly influence the response of asphaltic materials. In this contribution the extension of the Desai plasticity based material model for reversed cyclic loading is presented. Hardening of the material is simulated via a mixed hardening formulation. In order to enable a smooth elastic-plastic transition, the bounding surface concept proposed by Dafalias and Popov is utilized.

INTRODUCTION

At Delft University of Technology in the Netherlands in cooperation with the University of Nottingham, UK, a joint experimental and analytical investigation is currently being carried out on the mechanisms leading to damage of asphaltic materials. One of the deliverables of the project will be a fully calibrated three dimensional constitutive model for the inelastic, stress, temperature and strain-rate dependent response of asphalt concrete. Particular emphasis is placed on the capabilities of the model to simulate the response after large number loading cycles.

The preliminary version of the model has been implemented in the finite element system CAPA-3D [6] developed at Delft University of Technology. In this contribution, those aspects of the model relating to cyclic response simulation will be briefly presented.

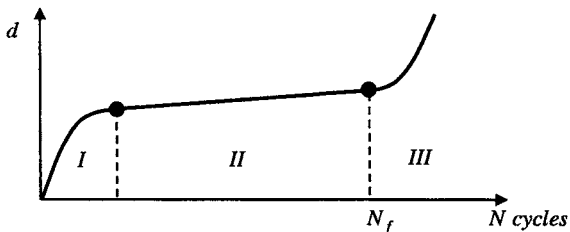


Fig. 1 Schematic of permanent deformation development relative to number of cycles

¹ Corresponding author, Nottingham Centre for Pavement Engineering, University of Nottingham, United Kingdom. E-mail: a.e.swart@ct.tudelft.nl

² Section of Structural Mechanics, Faculty of Civil Engineering and Geosciences, Delft University of Technology, The Netherlands

In Fig. 1 a schematic is presented of the development of permanent deformation in an asphaltic material when subjected to a large number of loading cycles under constant stress level. During the first few cycles, the permanent deformation increases rapidly. After some cycles, the rate of permanent deformation development stabilizes. It is only after a limit number of cycles N_f that response degradation occurs.

The monotonic response curve of the material serves as the backbone curve within which the cyclic response develops. As shown in Fig. 2, the tertiary phase initiates when the state of stress during cyclic loading attains a value of effective strain corresponding to strength degradation. This implies all experimentally observed monotonic response characteristics like, hardening, softening, sensitivity to confinement and state of stress, are inherited by the cyclic model.

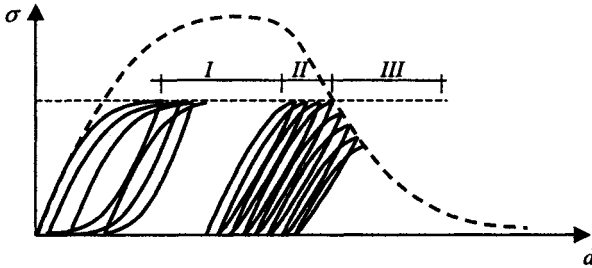


Fig. 2 Postulated cyclic response degradation model

In standard elastoplasticity, the response of a material within the yield surface is postulated to be elastic. In order to allow for some magnitude of energy dissipation for load cycles at stress states within the yield surface the bounding surface concept proposed earlier by Dafalias is utilized. By this means, during cycling, any experimentally observed amount of cyclic energy dissipation can be assigned. In the following, the monotonic features of the model will be briefly reviewed and then the cyclic will be addressed in more detail.

1 MONOTONIC MODEL

1.1 Computational Plasticity

The strain rate of the material $\dot{\epsilon}$ can be decomposed in an elastic and a plastic part:

$$\dot{\epsilon} = \dot{\epsilon}^e + \dot{\epsilon}^p \quad (1)$$

The associated flow rule is defined as:

$$d\epsilon^p = d\lambda \frac{\partial F}{\partial \sigma}, \quad (2)$$

with the standard Kuhn-Tucker conditions:

$$d\lambda \geq 0, \quad F \leq 0, \quad d\lambda \cdot F = 0 \quad (3)$$

Evolution of plastic flow is determined by the consistency condition:

$$\dot{F}(\sigma, \delta, \kappa) = 0 \quad (4)$$

1.2 Formulation of the Desai Model

In this contribution the Desai yield function, as proposed by Desai [1] in the context of the hierarchical approach, is utilized to model the monotonic mechanical response of the asphaltic material. One attractive feature of this particular surface is that it includes most of the currently common used plasticity models as special cases. The surface is continuous and hence avoids the problems of multisurface models. The chosen form of the model yield function is given by:

$$F = \frac{q^2}{3p_a^2} - \left[-\alpha \cdot \left(\frac{3p}{p_a} \right)^n + \gamma \cdot \left(\frac{3p}{p_a} \right)^m \right] = 0, \quad (5)$$

where p and q are the effective mean normal stress and deviatoric stress respectively, α, γ, m and n are material parameters. p_a is the atmospheric pressure. Parameter m controls the nonlinearity of the ultimate surface. In the theory of plasticity, nonassociated flow rules are commonly used for plasticity modeling of frictional material. In the hierarchical approach, the potential surface is given by:

$$Q = \frac{q^2}{3p_a^2} - \left[-\alpha_Q \cdot \left(\frac{3p}{p_a} \right)^n + \gamma \cdot \left(\frac{3p}{p_a} \right)^m \right] \quad (6)$$

in which $\alpha_Q = \alpha + \kappa_c (\alpha_0 - \alpha)(1 - \chi_v)$. Parameter α_0 is the value of α at the initiation of nonassociativeness, κ_c is the nonassociative material parameter, χ_v controls the contribution of volumetric plastic deformation to the expansion of the potential surface. All parameters in Eq. (5) and (6) are experimentally determinable. Determination of the parameters and specific forms for the hardening/softening parameter α can be found in Liu et al. [5] and Erkens et al. [7].

1.4 Numerical implementation

Aravas [3] proposed a numerical algorithm, based on the Euler backward concept, for pressure-dependent plasticity models. First a trial state of stress is obtained, assuming that the entire step is elastic:

$$\boldsymbol{\sigma}^e = {}^t \boldsymbol{\sigma} + \mathbf{C}^e \cdot \Delta \boldsymbol{\varepsilon} \quad (7)$$

Integration of Eq. (2) yields:

$${}^{t+\Delta t} \Delta \varepsilon_{ij}^p = \left| \Delta \lambda \cdot \frac{\partial Q}{\partial \sigma_{ij}} = {}^{t+\Delta t} \Delta \lambda \cdot \left(-\frac{1}{3} \left(\frac{\partial Q}{\partial p} \right) \cdot \delta_{ij} + \left(\frac{\partial Q}{\partial q} \right) \cdot \frac{3}{2} \frac{s_{ij}}{q} \right) \right| \quad (8)$$

The increment of plastic strain ${}^{t+\Delta t} \Delta \varepsilon^p$ can be expressed in terms of volumetric and deviatoric components as:

$${}^{t+\Delta t} \Delta \varepsilon_{ij}^p = \left| \frac{1}{3} \Delta \varepsilon_p \cdot \delta_{ij} + \Delta \varepsilon_q \cdot \frac{3}{2} \frac{s_{ij}}{q} \right|, \quad (9)$$

$$\text{where } {}^{t+\Delta t}\Delta\epsilon_p = \left. \begin{matrix} t+\Delta t \\ \left| \right. \end{matrix} -\Delta\lambda \left(\frac{\partial Q}{\partial p} \right) \text{ and } {}^{t+\Delta t}\Delta\epsilon_q = \left. \begin{matrix} t+\Delta t \\ \left| \right. \end{matrix} \Delta\lambda \left(\frac{\partial Q}{\partial q} \right) \right. \quad (10)$$

Elimination of $\Delta\lambda$ gives:

$$\left. \begin{matrix} t+\Delta t \\ \left| \right. \end{matrix} \Delta\epsilon_p \left(\frac{\partial Q}{\partial q} \right) + \Delta\epsilon_q \left(\frac{\partial Q}{\partial p} \right) = 0 \quad (11)$$

Equations (11) and (6), constitute a nonlinear algebraic system in terms of $\Delta\epsilon_p$ and $\Delta\epsilon_q$, which are chosen as the primary unknowns. The equations are solved by means of a Newton-Raphson iteration process at constitutive law level. During the iterative procedure, the stress is corrected along the hydrostatic and the deviatoric axes p and q . The stresses are finally updated via:

$${}^{t+\Delta t}\sigma = \left. \begin{matrix} t+\Delta t \\ \left| \right. \end{matrix} \sigma^e - K\Delta\epsilon_p \cdot \mathbf{I} - 2G\Delta\epsilon_q \cdot \left(\frac{3}{2} \frac{s}{q} \right). \quad (12)$$

2 CYCLIC MODEL

Classical plasticity does not allow for energy dissipation within the yield surface. A two-surface model, based on the bounding surface concept by Dafalias and Popov [2] has been developed. This model consists of a yield surface (Desai), which acts as a bounding surface to a smaller surface, known as loading surface. The loading surface is formulated with the same shape parameters as the bounding surface, Fig. 3. Initially its size and origin coincide with those of the F surface, i.e. $g(\bar{\sigma}, \alpha_g) = F(\sigma, \alpha_0)$ with $\bar{\sigma} = \sigma - \chi$. Due to strain hardening the bounding surface grows while the loading surface does not change in size and moves within F in the direction of the stress increment via kinematic hardening.

In the proposed model, states of stress inside the loading surface are postulated to be fully elastic. States of stress on the bounding surface are postulated to be elastoplastic. States of stress within the bounding surface but outside the loading surface are treated according to the procedure of Section 2.1.

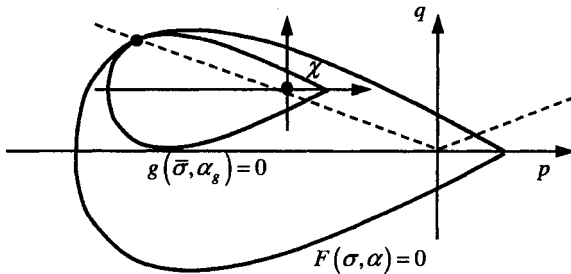


Fig. 3 Schematic of 2-surface model in p - q space

2.1 Constitutive framework

The loading surface moves in the direction of the elastic stress increment. Assuming, for visualization purposes, proportional loading, the state of stress ${}^*\sigma_F$ can be defined by the intersection of the projection of the elastic stress increment onto the outer surface, Fig. 4(a). Similarly, the state of stress ${}^*\sigma_Q$ can be defined by the intersection of the projection of the elastic stress increment onto the potential surface, Fig. 4(b).

During stress reversal at any point between the state of stress at the load reversal, ${}^{RVS}\sigma$, and the projection state ${}^*\sigma_F$, the increment of stress $\Delta\sigma$ is computed via

$$\Delta\sigma = C^e (\Delta\varepsilon - \Delta\varepsilon^{pc}) \tag{13}$$

$\Delta\varepsilon^{pc}$ is a fictitious plastic strain increment, evaluated via

$$\Delta\varepsilon^{pc} = (1 - \delta^\omega) (\Delta\varepsilon^p)_{\sigma_Q} \tag{14}$$

where $(\Delta\varepsilon^p)_{\sigma_Q}$ is the plastic strain increment at the potential surface $Q = 0$.

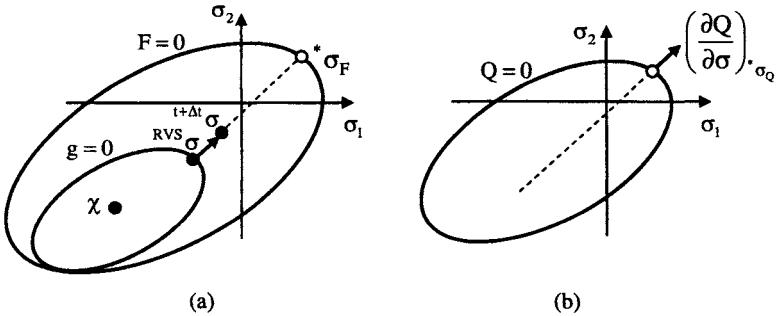


Fig. 4 Cyclic model for plane-stress conditions, (a) flow surface, (b) potential surface

2.1.1 parameter δ

The relative distance between the state of stress and the projection point at the bounding surface is described via:

$$\delta = \left(\frac{{}^*\sigma - {}^{t+\Delta t}\sigma}{{}^*\sigma - {}^{RVS}\sigma} \right) \tag{15}$$

When $\delta = 1$ the response is elastic, and when $\delta = 0$ the response is plastic.

2.1.2 Cyclic response degradation

Parameter ω is a material parameter representing material stiffness degradation with increasing number of cycles. ω varies from ω_1 at the first cycle to ω_∞ at the end of ratcheting.

$$\omega = \eta\omega_1 + (1 - \eta)\omega_\infty \tag{16}$$

The influence of ω on the response is shown in Fig. 5.

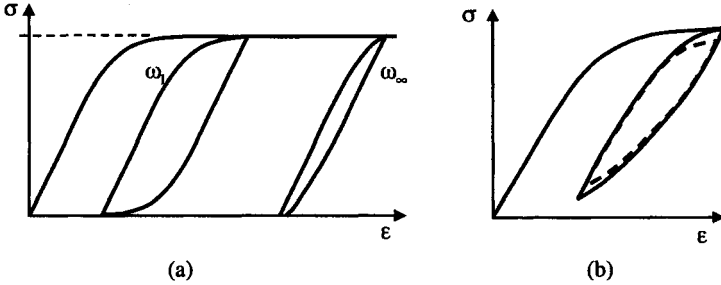


Fig. 5 Cyclic response degradation, (a) stress controlled and (b) strain controlled
Parameter η controls the degradation.

$$\eta = (1 + H \cdot \epsilon^{pc}) \cdot e^{-H \cdot \epsilon^{pc}} \tag{17}$$

The influence of η on the material response is shown in Fig. 6(a). A variation of $(1 - \delta^\omega)$ with δ for various ω values is shown in Fig. 6(b).

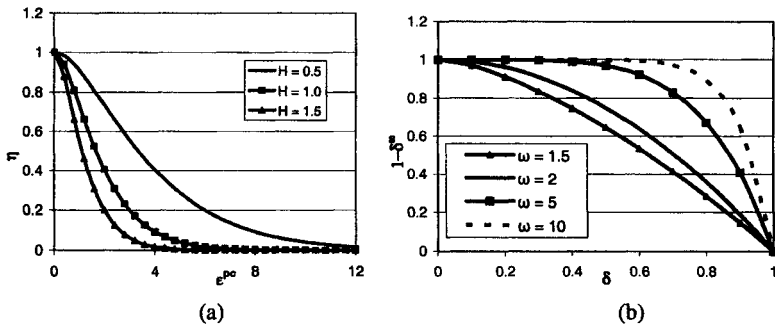


Fig. 6 (b) response degradation function, (a) Variation of $(1 - \delta^\omega)$ with δ .

Substituting Eq. (14) into Eq. (13) yields

$$\Delta\sigma = C^c \Delta\epsilon - C^c \cdot (\Delta\epsilon^p)_{\sigma_0} \cdot (1 - \delta^\omega), \tag{18}$$

which, physically, implies that the stress increment tensor $\Delta\sigma$ varies from $\mathbf{C}^e\Delta\varepsilon$ at ${}^{RVS}\sigma$ to the stress increment postulated by plasticity theory at ${}^*\sigma_Q$. In the following section computation of $(\Delta\varepsilon^P)_{\sigma_Q}$ will be addressed.

2.2 Numerical implementation

The truncated Taylor expansion of $F(\sigma, \alpha)$ about the state of stress at the projection point ${}^*\sigma$ is:

$${}^{t+\Delta t}F \approx {}^*F + \left(\frac{\partial F}{\partial \sigma}\right)_{\sigma}^T ({}^{t+\Delta t}\sigma - {}^*\sigma) + \left(\frac{\partial F}{\partial \alpha}\right)_{\sigma} ({}^{t+\Delta t}\alpha - {}^*\alpha) = 0 \quad (19)$$

The change of the yield condition from state * to state $t + \Delta t$ must be zero. This is the classic consistency condition of Prager, which on account of Eq. (18) becomes:

$$\Delta F = \left(\frac{\partial F}{\partial \sigma}\right)_{\sigma}^T \left(\mathbf{C}^e \Delta \varepsilon - \Delta \lambda {}^* \mathbf{C}^e \left(\frac{\partial Q}{\partial \sigma}\right)_{\sigma} \right) + \left(\frac{\partial F}{\partial \alpha}\right)_{\sigma} \Delta \alpha = 0 \quad (20)$$

in which α is some measure of hardening/softening.

$$\Delta \alpha = \frac{\partial \alpha}{\partial \varepsilon^P} \cdot \Delta \varepsilon^P \quad (21)$$

Substituting this in Eq. (20) and solving in terms of $\Delta \lambda$:

$$\Delta \lambda^* = \frac{\left(\frac{\partial F}{\partial \sigma}\right)_{\sigma}^T \cdot \mathbf{C}^e \cdot \Delta \varepsilon}{\left(\frac{\partial F}{\partial \sigma}\right)_{\sigma}^T \cdot \mathbf{C}^e \cdot \left(\frac{\partial Q}{\partial \sigma}\right)_{\sigma} - \frac{\partial F}{\partial \alpha} \cdot \frac{\partial \alpha}{\partial \varepsilon^P} \cdot \left(\frac{\partial Q}{\partial \sigma}\right)_{\sigma}} \quad (22)$$

Hence, $(\Delta\varepsilon^P)_{\sigma_Q}$ in Eq. (18) can be computed as:

$$(\Delta\varepsilon^P)_{\sigma_Q} = \Delta \lambda^* \left(\frac{\partial Q}{\partial \sigma}\right)_{\sigma} \quad (23)$$

3 NUMERICAL EXAMPLE

The actual model parameters have been evaluated on the basis of a preliminary set of multiaxial experimental results at the University of Nottingham.

Utilization of the above proposed model is illustrated in this section for the case of an asphaltic material subjected to uniaxial cyclic compression at a constant stress of 10 MPa. The parameters of the monotonic model are: $E = 2000$ MPa, $\nu = 0.35$ and $p_a = -0.1$ MPa. All other parameters are functions of the strain rate. The parameters of the cyclic model are: $\omega_1 = 4.0$, $\omega_u = 2.0$ and $H = 2.0$.

The stress-strain response of the material, before the tertiary phase, with increasing number of cycles is shown in Fig. 7. Model calibration of the tertiary phase is subject to investigation.

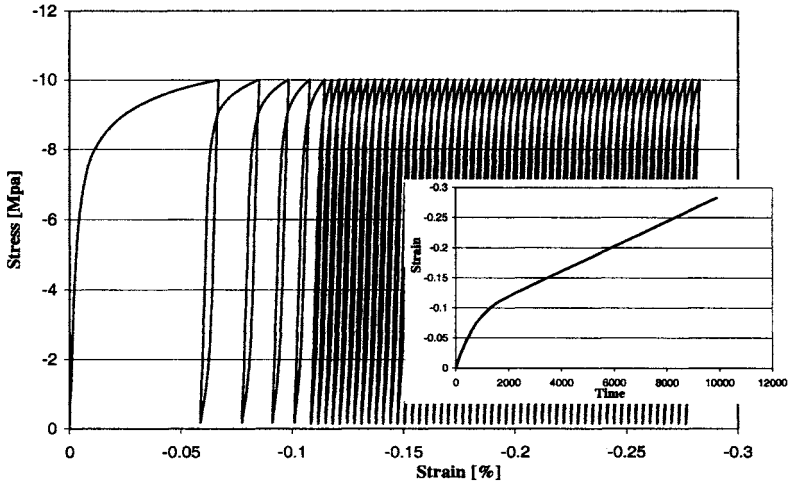


Fig. 7 Stress-strain relation numerical example

As typically observed in laboratory tests with constant stress, the model allows for a gradual decrease of the amount of energy dissipated per cycle and a smooth transition to the steady state response indicated as phase II in Fig. 1 and the insert of Fig. 7.

REFERENCES

- [1] C.S. Desai, *A general basis for yield, failure and potential functions in plasticity*, Int. Journal for Numerical and Analytical Methods in Geomechanics 4 (1980), 361-375.
- [2] Y.F. Dafalias, E.P. Popov, *A model of nonlinearly hardening materials for complex loading*, Acta Mechanica 21 (1975), 173-192.
- [3] N. Aravas, *On the numerical integration of a class of pressure-dependent plasticity models*, Int. J. Num. Meth. Eng. 24 (1987), 1395-1416.
- [4] A.E. Swart, A. Scarpas and J. Blaauwendraad, *3D Material Model for Cyclic Behaviour of Metallic Materials*, Fifth World Congress on Computational Mechanics, 2002, Vienna, Austria.
- [5] X.Liu, X. Cheng, A. Scarpas and J. Blaauwendraad, *Numerical modelling of the non-linear response of soil Part I: Constitutive Model*, International Journal of Solids & Structures 42 (2004), 1849-1881.
- [6] A. Scarpas and C. Kasbergen, *CAPA 3D User's Manual* (1999).
- [7] Erkens, S.M.J.G. , Liu, X. and Scarpas, A., "3D Finite Element Model for Asphalt Concrete Response Simulation", The International Journal of Geomechanics, Volume 2, Number 3, p. 305 - 330 (2002).

NUMERICAL IMPLEMENTATION OF A HYPERELASTIC-VISCOPLASTIC DAMAGE MODEL FOR ASPHALT CONCRETE MATERIALS AND PAVEMENTS

Dinesh Panneerselvam¹ and Vassilis P. Panoskaltsis^{2*}

ABSTRACT

The algorithmic aspects and the numerical implementation of a new multi-dimensional hyperelastic-viscoplastic-damage model for asphalt concrete are presented. A predictor-corrector algorithm is developed, the algorithmic moduli are computed and the model is implemented into the finite element environment ABAQUS® and is used for the simulation of several experimental results as well as for the analysis of a section of a pavement. The proposed strain energy function is expressed in terms of the invariants of the deviatoric left Cauchy-Green strain tensor as well as of the volume ratio J . A unique feature of the paper is that experiments are treated both as homogeneous (local) and as boundary value problems (global) and the model's simulations for each case are compared.

INTRODUCTION

Permanent deformation under repeated loading (rutting) is the most prominent distress in pavements. For its proper modeling it is crucial that the main mechanisms contributing to rutting be identified. These mechanisms are the densification (compaction) and the shear flow of the material. In properly compacted pavements shear flow is considered to be the primary rutting mechanism. Also, the mix exhibits volumetric/deviatoric coupling behavior; this is understood as the mix dilates under shear loading. A new multi-dimensional hyperelastic-viscoplastic-damage model is developed to describe and predict the permanent deformations and coupling behavior of asphalt concrete. The elastic behavior of asphalt concrete is modeled by a second order hyperelastic model, since the volumetric/deviatoric coupling behavior of the mix is observed even at very small strain values and at lower temperatures. Viscoplasticity is introduced in order to describe the rate dependent permanent deformation of the mix. This theory is used successfully to model the ratcheting behavior exhibited by the mix. The loading surface used in this model is based on the Vermeer loading surface, which has been used successfully for soils. A non-

¹ Application Engineer, ABAQUS Great Lakes Inc., Plymouth, Michigan 48170

² Associate Professor, Case Western Reserve University, Department of Civil Engineering, Cleveland, Ohio, 44106-7201, U.S.A., vpp@nestor.cwru.edu

* To whom correspondence should be addressed.

associative flow rule for the plastic strain's evolution and an evolution equation for the hardening parameter are provided; moreover, damage based on effective stress theories is included in the model.

This paper concentrates on the numerical implementation aspects of the constitutive model. Numerical implementation and algorithmic aspects of the multi-dimensional hyperelastic-viscoplastic-damage model are presented. A robust integration algorithm for the nonlinear differential equations is described; also the algorithmic (consistent) tangent moduli are derived. The model is implemented into the finite element environment ABAQUS[®] to study boundary value problems. Triaxial, uniaxial compression, shear and 'repeated simple shear tests at constant height' (RSST-CH) are studied and results are compared to experiments. Finally, a section of the pavement is studied as a boundary value problem in order to assess the capability of the model to predict rutting in the pavement. As is well known, asphalt is a temperature sensitive material. This important aspect is not taken into account in this work. A model, which includes temperature effects, will appear in a forthcoming publication by the authors.

Hyperelastic-Viscoplastic-Damage Model

In this section, a brief discussion on the aforementioned constitutive model is given and its governing equations are summarized.

Hyperelastic model

A second order hyperelastic model is developed in order to describe the coupling between shear and axial stress components of asphalt, which develop in a shear loading. Elasticity is used since the evolution of normal stresses is apparent from the very first cycles, during which no permanent deformation has occurred. These experiments were conducted at 4°C and viscous effects are minimal at this low temperature, Sousa et al. (1993).

The strain energy function $W(\boldsymbol{\varepsilon}): R^6 \rightarrow R$ that is proposed here for the second order hyperelastic isotropic model is given by

$$W(\boldsymbol{\varepsilon}) = b_1 I_1^2 + b_2 I_2 + b_3 I_1^3 + b_4 I_1 I_2 + b_5 I_3 \quad (1)$$

where, $\boldsymbol{\varepsilon}$ is the strain tensor, b_1 , b_2 , b_3 , b_4 , and b_5 are material constants. This form satisfies the condition that at zero strain state (material's natural state) the value of the strain energy function and the stress tensor are zero. I_1 , I_2 , I_3 are the invariants of the strain tensor defined as $I_1 = \text{tr} \boldsymbol{\varepsilon}$, $I_2 = \text{tr} \boldsymbol{\varepsilon}^2$, $I_3 = \text{tr} \boldsymbol{\varepsilon}^3$.

The stress tensor is given by

$$\sigma_{ij} = \frac{\partial W(\boldsymbol{\varepsilon})}{\partial \varepsilon_{ij}} = (2b_1 I_1 + 3b_3 I_1^2 + b_4 I_2) \delta_{ij} + (b_2 + b_4 I_1) \varepsilon_{ij} + b_5 \varepsilon_{im} \varepsilon_{mj} \quad (2)$$

The model has been validated against uniaxial compression, volumetric and shear experiments conducted at the University of California, Berkeley (Sousa et al. 1993); see Panneerselvam and Panoskaltis (2004) for model's validation.

Viscoplasticity

The permanent deformation in asphalt concrete, which is time dependent, is modeled by a Perzyna type viscoplasticity model. Asphalt concrete exhibits ratcheting behavior under repeated loading and to capture this phenomenon a loading surface based viscoplasticity model is introduced, instead of a classical yield surface based viscoplasticity model. Apart from the loading surface, other ingredients of the model are the flow rule for the viscoplastic strain and the hardening rule for the hardening parameter. A non-associative flow rule is adopted in order to prevent excessive dilation predicted by an associative one. The model also accounts for damage; the damage variable is a function of the viscoplastic strain and is introduced through effective stress theories. A summary of the equations of the model is given below; see Panneerselvam (2005) for more details on the model.

Loading Surface:

$$f^c = I_1^c I_2^c + \alpha I_3^c - H \kappa, \quad (3)$$

where I_1^c , I_2^c and I_3^c are the modified first, second and third invariants of stress and κ is the hardening variable. The invariants are properly modified, in order to account for the damage, as follows: The damage variable ' ω ' is defined as

$$\omega = \frac{A}{A_0}; \quad 0 \leq \omega \leq 1, \quad (4)$$

where A_0 is the initial area of the undamaged section and A is the area lost due to damage. It is a positive, monotonically increasing function, i.e. $\dot{\omega} > 0$; in other words, damage is irreversible. The effective stress σ_a , is defined as

$$\sigma_a = \frac{\sigma}{1 - \omega}, \quad (5)$$

where σ is the nominal stress. The damage is incorporated in the model and stress invariants are modified accordingly:

$$I_1^c = \frac{I_1}{1 - \omega}, I_2^c = \frac{I_2}{(1 - \omega)^2}, I_3^c = \frac{I_3}{(1 - \omega)^3}, \quad (6)$$

where I_1 , I_2 and I_3 are the typical stress invariants.

The damage variable is assumed to be a function of the total viscoplastic strain:

$$\omega = a_1 (\boldsymbol{\varepsilon}^{vp})^{a_2}, \quad (7)$$

where a_1 and a_2 are parameters.

Flow Rule (evolution equation for viscoplastic strain tensor):

$$\dot{\boldsymbol{\varepsilon}}^{vp} = \left(\frac{\langle f^c \rangle}{\eta} \right)^m \frac{1}{(x + \kappa^l)} \boldsymbol{\nu}, \quad (8)$$

where η is the viscous parameter, x, l, m and γ are material parameters.

Normal to the plastic potential Ω :

$$\boldsymbol{\nu} = \frac{\partial \Omega}{\partial \boldsymbol{\sigma}} \quad (9)$$

$$\Omega = \sqrt{J_2^c} + \gamma I_1^c, \quad (10)$$

where J_2^c is the modified second invariant of the deviatoric stress tensor.

Hardening Rule (evolution equation for hardening variable):

$$\dot{\kappa} = \left(\frac{\langle f^c \rangle}{\eta} \right)^m \frac{1}{(x + \kappa^l)}. \quad (11)$$

The superimposed dots in Eqs. (8) and (11) denote material time derivatives. These equations are supplemented with the elastic relation, given by the hyperelastic model.

Numerical Implementation: Basic Algorithmic Setup: Strain-Driven Problem

The complete model can be thought of as a model in series and accordingly, the total strain is additively decomposed into elastic and viscoplastic parts. The decomposition is justified since the magnitude of the strains is small.

$$\boldsymbol{\varepsilon} = \boldsymbol{\varepsilon}^e + \boldsymbol{\varepsilon}^{vp}. \quad (12)$$

Let $[0, T] \subset R$ be the time interval of interest. At time $t_n \in [0, T]$, it is assumed that the total strain and viscoplastic strain fields, as well as the internal variables are known, that is

$\boldsymbol{\varepsilon}_n$: total strain tensor

$\boldsymbol{\varepsilon}_n^{vp}$: viscoplastic strain tensor

κ_n : isotropic hardening variable

are given at time t_n . The elastic strain is obtained by Eq. (12), i.e. $\boldsymbol{\varepsilon}^e = \boldsymbol{\varepsilon}_n - \boldsymbol{\varepsilon}_n^{vp}$ and the stress tensor is obtained using the elastic stress strain relationships:

$$\boldsymbol{\sigma} = \frac{\partial W(\boldsymbol{\varepsilon}^e)}{\partial \boldsymbol{\varepsilon}^e}, \quad (13)$$

where W is the strain energy function introduced for the hyperelastic model. The stress components are calculated by substituting in Eq. (2) the elastic components of the total strain tensor.

Let $\Delta \mathbf{u}_{n+1}^i$ be the incremental displacement field, which is assumed to be resulting from the i^{th} iteration of the global equilibrium equations at time step t_{n+1} . The basic problem is to update the field variables to $t_{n+1} \in [0, T]$ in a manner consistent with the elasto-viscoplastic constitutive equations (3) to (11). The problem is strain driven in the sense that the total strain tensor is updated according to

$$\boldsymbol{\varepsilon}_{n+1} = \boldsymbol{\varepsilon}_n + \nabla^s (\Delta \mathbf{u}_{n+1}^i), \quad (14)$$

where $\nabla^s(\bullet)$ denotes the symmetric gradient operator. The evolution equations for the continuum problem are transformed into discrete, algebraic equations by applying an implicit backward -Euler difference scheme, which is first order accurate and unconditionally stable. Applying the backward-Euler difference scheme to Eqs. (8) and (11) a system of coupled nonlinear equations is obtained, which is given below.

$$\boldsymbol{\varepsilon}_{n+1}^{vp} = \boldsymbol{\varepsilon}_n^{vp} + \left(\frac{\langle f_{n+1} \rangle}{\eta} \right)^m \frac{\mathbf{v}_{n+1}}{x + \kappa_{n+1}^j} \Delta t, \quad (15)$$

$$\kappa_{n+1} = \kappa_n + \left(\frac{\langle f_{n+1} \rangle}{\eta} \right)^m \frac{1}{x + \kappa_{n+1}^j} \Delta t, \quad (16)$$

where Δt is the time step increment, i.e. $\Delta t = t_{n+1} - t_n$. The system of Eqs. (15) and (16) is solved under the general framework of predictor-corrector methods. The predictor phase consists of an elastic problem during which the internal variables are assumed to be frozen. In the corrector phase the internal variables evolve and the total viscoplastic strain and hardening parameter are updated to time step t_{n+1} . This state is obtained as a solution of the evolution equations Eqs. (15) and (16) by a Newton scheme (in multi dimensions). The predictor-corrector algorithm developed for the model is illustrated in the following Box. (Superscripts denote the iteration number.)

1. Predictor Phase**Compute elastic predictor**

$$\sigma_{n+1}^{(0)} = \nabla W \left(\nabla^s (\Delta u_{n+1}) - \epsilon_n^{vp} \right)$$

Update with damage

$$\sigma_{n+1}^{(0)} = \frac{\sigma_{n+1}^{(0)}}{1 - \omega}$$

Compute loading surface $f_{n+1}^{(0)} = f(\sigma_{n+1}^{(0)})$ IF $f(\sigma_{n+1}^{(0)}) \leq 0$ THEN **Elastic phase**Set $\epsilon_{n+1}^{vp} = \epsilon_n^{vp}$ and EXITELSE $[f(\sigma_{n+1}^{(0)}) \geq 0]$ **Plastic phase**

GO TO 2.

ENDIF

2. Corrector Phase

$$\sigma_{n+1}^{(k)} = \nabla W \left(\nabla^s (\Delta u_{n+1}) - \epsilon_n^{vp(k)} \right)$$

Update with damage

$$\sigma_{n+1}^{(k)} = \frac{\sigma_{n+1}^{(k)}}{1 - \omega}$$

2a. Compute Residuals

$$f_{n+1}^{(k)} = f(\sigma_{n+1}^{(k)})$$

$$R_{n+1}^{(k)} = \epsilon_{n+1}^{vp(k)} - \epsilon_n^{vp} - \left(\frac{f_{n+1}^{(k)}}{\eta} \right)^m \frac{V_{n+1}^{(k)}}{x + \kappa_{n+1}^{(k)}} \Delta t$$

$$S_{n+1}^{(k)} = \kappa_{n+1}^{(k)} - \kappa_n - \left(\frac{f_{n+1}^{(k)}}{\eta} \right)^m \frac{1}{x + \kappa_{n+1}^{(k)}} \Delta t$$

2b. Check ConvergenceIF $\|R_{n+1}^{(k)}\| > TOL_1$ or $f(\sigma_{n+1}^{(k)}) > TOL_2$ or $\|S_{n+1}^{(k)}\| > TOL_3$ THEN*Compute k^{th} increments*

$$\Delta \kappa_{n+1}^{(k)}, \Delta \epsilon_{n+1}^{vp(k)}$$

Update Stress Tensor, Viscoplastic Strains and Hardening Parameter

$$\sigma_{n+1}^{(k+1)} = \sigma_{n+1}^{(k)} + \Delta \sigma_{n+1}^{(k)}$$

$$\epsilon_{n+1}^{vp(k+1)} = \epsilon_{n+1}^{vp(k)} + \Delta \epsilon_{n+1}^{vp(k)}$$

$$\kappa_{n+1}^{(k+1)} = \kappa_{n+1}^{(k)} + \Delta \kappa_{n+1}^{(k)}$$

```


$$\omega = a_1 \left( \epsilon_{n+1}^{vp(k+1)} \right)^{a_2}$$

Set  $k \leftarrow k + 1$  and GO TO 2a.
ELSE
Set  $\epsilon_{n+1}^{vp} = \epsilon_{n+1}^{vp(k)}$ 
ENDIF EXIT
    
```

The algorithm presented in the Box is for the solution at a local material point. For the global procedure and in order to maintain the quadratic rate of convergence of Newton’s method, which is employed for the solution of the global equilibrium equations, the algorithmic tangent moduli are derived. These are defined as the derivative of the stress with respect to the strain tensor at time step t_{n+1} , after convergence at the local level has been attained. See, Simo and Taylor (1985), Simo and Hughes (1998) and Panoskaltzis and Lubliner (1991) (for the computation of algorithmic moduli in viscoelasticity). The algorithmic tangent moduli for the complete model are derived as follows:

$$C_{alg}^{-1} = \frac{d\epsilon_{n+1}}{d\sigma_{n+1}} = \frac{d\epsilon_{n+1}^e}{d\sigma_{n+1}} + \frac{d\epsilon_{n+1}^{vp}}{d\sigma_{n+1}} = D_{n+1}^e + \frac{d\epsilon_{n+1}^{vp}}{d\sigma_{n+1}}, \tag{17}$$

where D_{n+1} is the Hessian matrix obtained from the hyperelastic model. Therefore, the algorithmic tangent moduli can be written as:

$$C_{alg} = \left(D_{n+1}^e + \frac{d\epsilon_{n+1}^{vp}}{d\sigma_{n+1}} \right)^{-1}. \tag{18}$$

The second term in the expression for C_{alg} is determined from Eq. (15) as follows:

$$\frac{d\epsilon_{n+1}^{vp}}{d\sigma_{n+1}} = \left(\frac{f_{n+1}}{\eta} \right)^m \frac{1}{(x + \kappa_{n+1}^e) d\sigma_{n+1}} \frac{dv_{n+1} \Delta t}{d\sigma_{n+1}} + \frac{m \left(\frac{f_{n+1}}{\eta} \right)^{m-1} \frac{v_{n+1} \Delta t}{(x + \kappa_{n+1}^e) d\sigma_{n+1}}}{1 + \left(\frac{f_{n+1}}{\eta} \right)^m \frac{\Delta t \kappa_{n+1}^{e-1}}{(x + \kappa_{n+1}^e)^2} \Delta t}. \tag{19}$$

RESULTS

Model predictions to experiments will be presented in this section of the paper. The parameters of the model will be obtained by fitting it to experimental results; as is usually done in parameter estimation procedures, the experiments are assumed to be homogeneous and the results are interpreted as providing stress and strain at a point of the specimen (‘local fitting results’). Furthermore, in our work, and in order to better assess the reliability of our model, the experiments are thought of as representing boundary value problems –an assumption which is closer to reality- and the experimental results are compared to finite element results (‘global fitting results’). The algorithm described in the Box is implemented in MATLAB[®], and the

combined model is validated against triaxial experimental results by Tashman et al. (2004). Cylindrical specimens of 4 in diameter and 6 in height are subjected to uniaxial compression at three different rates (46.42%/min, 8.03%/min, and 1.6%/min) and two confining pressures (0 psi and 15 psi). The base of each cylinder is fixed and its top is subjected to displacement control in the axial direction, while it is fixed in the other directions. The model predictions to experimental results are given in Figs. 1 and 2 below (for parameter values see Panneerselvam 2005).

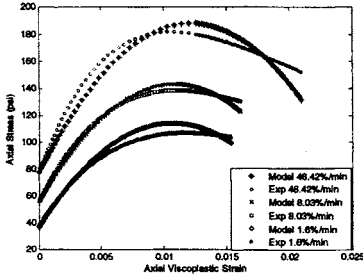


FIG. 1. Axial Stress vs. Axial Viscoplastic Strain. Model fit to triaxial experimental data at 0-psi confinement pressure

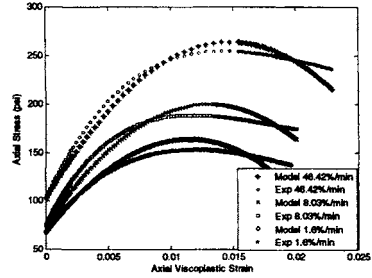


FIG. 2. Axial Stress vs. Axial Viscoplastic Strain. Model fit to triaxial experimental data at 15-psi confinement pressure

Hyperelastic model implementation in ABAQUS

In order to study the experiments as boundary value problems, the hyperelastic model needs to be implemented within the context of a finite element program. The implementation is done through user subroutine module UHYPER of ABAQUS[®]. At each Gauss integration point, the user material subroutine UHYPER is called for externally by the main program and stresses corresponding to strain states are obtained. In the subroutine, the strain energy function is supplied in terms of deviatoric strain invariants and also the derivatives of the strain energy function with respect to deviatoric strain invariants have been derived and provided. The strain energy function introduced in Eq. (1) has to be rewritten in terms of the deviatoric strain invariants. After some algebra, the strain energy function is obtained as:

$$U(\bar{I}_1, \bar{I}_2, J) = b_1 \bar{I}_1^2 J^{1/2} + b_2 \bar{I}_2 J^{1/2} + b_3 \bar{I}_1^3 J^2 + b_4 \bar{I}_1 \bar{I}_2 J^2 + b_5 J^2, \quad (20)$$

where \bar{I}_1 , \bar{I}_2 are the first and second deviatoric invariants, i.e. the invariants of the modified left Cauchy-Green deformation tensor $\bar{\mathbf{b}}$ (which describes the volume-preserving (isochoric) or distortional part of the deformation, see e.g. Simo and Hughes 1998) and J is the determinant of the deformation gradient \mathbf{F} . The finite element program's formulation is for the fully nonlinear case and as such it encompasses the present, material only, nonlinearity. The values of the parameters b_1 to b_5 are obtained by fitting the hyperelastic model (given by Eq. (1) to the same tests

but been interpreted as homogeneous. For the parameter determination analysis, being omitted here because of lack of space, see Panneerselvam (2005). The local fitting results are also shown in Figs. 3 and 4 and are indicated as ‘model’ in the figures’ captions. The tests performed by Sousa et al. (1993) are modeled as boundary value problems and solved for in ABAQUS®; cylindrical specimens were used with dimensions of 6 in diameter and 2 in height and the testing was kept within material’s elastic range. In the first type of experiments the specimens were subjected to uniaxial compression under displacement control. The finite element results are compared to experimental results and this is shown in Fig. 3. The good agreement between experimental, FEM and local results is remarkable. In the second type of experiments a shear type of test is performed. A prescribed amount of horizontal displacement is applied at the upper surface of the cylinder whose height is kept constant throughout the test. The comparison between finite element, experimental and local results is shown in Fig. 4; as before, the agreement is remarkable.

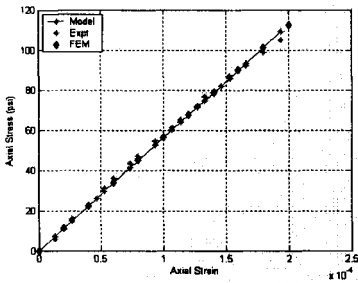


FIG. 3. Axial stress vs. axial strain. Comparison of finite element results to experimental data.

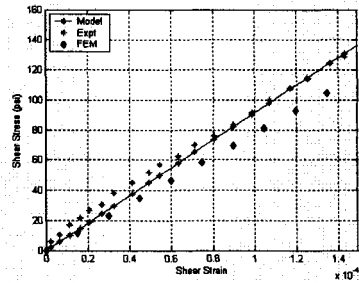


FIG. 4. Shear stress vs. shear strain. Comparison of finite element results to experimental data.

Hyperelastic-viscoplastic-damage model implementation in ABAQUS

The complete hyperelastic-viscoplastic-damage model is now implemented within the context of ABAQUS®. The implementation is carried out through user subroutine module UMAT. The algorithm described in the Box in conjunction to the consistent moduli given by Eqs. (18) and (19) are used. At each integration Gauss point UMAT is called for externally by the main program and stresses corresponding to strain states are obtained. The internal variables are updated at each time step through the user subroutine SDVINI.

The triaxial experiments performed by Tashman et al. (2004) and described earlier, are modeled as boundary value problems and solved for in ABAQUS®. The parameters which were obtained from the previous local simulation (in which the experiments were treated as being homogeneous, see Figs. 1 and 2) were used. The results from the finite element analysis are compared to the experimental data and this is shown in Fig. 5 and Fig. 6 for 0 and 15 psi confining pressure respectively.

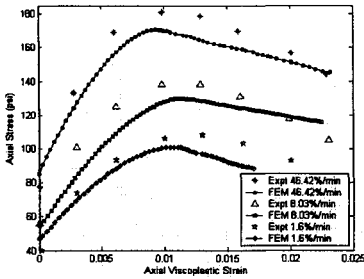


FIG. 5. Axial stress vs. axial viscoplastic strain. Comparison of finite element results to experimental data.

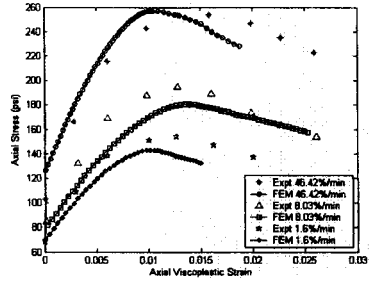


FIG. 6. Axial stress vs. axial viscoplastic strain. Comparison of finite element results to experimental data.

Next, the ‘repeated simple shear test at constant height’ (Sousa et al. 1993) is modeled as a boundary value problem. The RSST-CH experiment is conducted on the cylindrical specimens, which were described earlier in the monotonous experiments by Sousa et al. (1993), and the specimen is subjected to a repeated shear loading while the height of the specimen is kept constant. A haversine load of 0.05 s loading and 0.05 s unloading time is applied on a 0.2 in thick steel plate, which is glued to the cylindrical specimen. A remarkable characteristic of these experiments is that the accumulation of permanent shear strain with increasing number of cycles is a straight line on a log-log scale. The model is fitted to experimental results of 8 psi load amplitude and with the values obtained for the parameters the model’s predictions to 10 psi loading amplitude are obtained. The results, which are shown in Fig. 7 are very good.

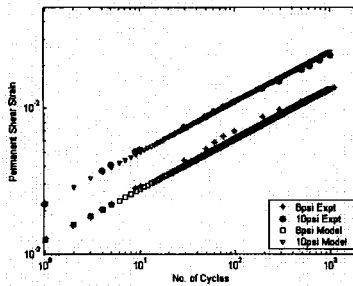


FIG. 7. Evolution of permanent shear strain with no. of cycles.

Finally, a section of a pavement, subjected to repeated tire pressure loading, is studied as a boundary value problem under plane strain conditions. This is a two dimensional model in which the two wheel pressure loads have been simulated as

continuous loading strips, consistent with the plane strain assumption. The boundary conditions used in the model are consistent with physical conditions of the pavement and also the symmetry in the road section has been used effectively; this results in more efficient computational time. The asphalt concrete layer is taken to be 15 in deep and rests on a 40 in deep subgrade. The bottom edge and also the sides of the subgrade are fixed. The width of the half pavement is 80 in and the width of the subgrade is 160 in. The outer edge of asphalt pavement is assumed to be unsupported and is free to deform. Traffic load is applied as two tire pressure loads of magnitude 100 psi; the wheel loads are 10 in wide and they have a center to center distance equal to 12 in. The plane strain conditions, under which the complete model of the pavement section is studied, is a good assumption for a section of a highway where the traffic does not stop or start. A more complicated three dimensional pavement model could be used to represent pavement sections such as intersections, where traffic accelerates, decelerates or stands still. The asphalt concrete pavement is modeled using the hyperelastic-viscoplastic-damage model developed in this work. The subgrade is a granular material and a nonlinear material model would best represent its behavior. However, for simplicity and to keep the computational time shorter, the subgrade is modeled as a linear elastic material with elasticity modulus of 20000 psi and Poisson's ratio of 0.3; see Sousa et al. (1993). Figure 8 shows the deformed shape of the pavement at the end of 15 cycles, magnified 100 times, and also the stress distribution in the pavement section. The figure shows permanently deformed shape and also shows the upheavals to the sides due to shear flow and dilation and is similar to those observed in rutted pavement sections. This simulation of rutting pattern illustrates the capability of the model to study boundary value problems representing pavement sections as well as model's potential for rational analysis and design of pavements.

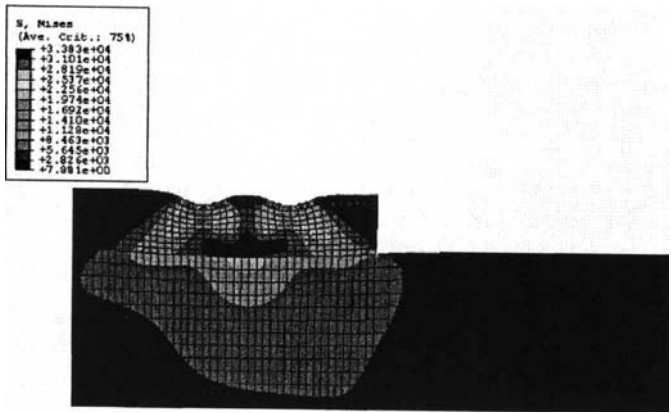


FIG. 8. Stress distribution in the deformed pavement.

ACKNOWLEDGEMENTS: The authors gratefully acknowledge financial support from the National Science Foundation, grant No. CMS-9802184.

REFERENCES

- Panneerselvam, D., and Panoskaltsis, V.P., (2004) "Modeling and predicting the permanent deformations and damage of asphalt concrete: Analytical and computational aspects." Proceedings of the 17th ASCE Engineering Mechanics Conference, V. Kaliakin et al. eds., University of Delaware, Newark, Delaware, June 13-16. (Proceedings in CDROM form).
- Panneerselvam, D., (2005) "Mechanics of Asphalt Concrete: Analytical and Computational Aspects", Ph.D. Dissertation, Department of Civil Engineering, Case Western Reserve University, Cleveland, Ohio.
- Panoskaltsis, V.P. and Lubliner J. (1991), "Integration Algorithm for Frictional Materials Including Plasticity, Damage and Rate Effects", in *Anisotropy and Localization of Plastic Deformation*, J.-P. Boehler and A.S. Khan eds., Elsevier, London, pp. 651-654.
- Simo, J.C., and Taylor, R.L., (1985) "Consistent Tangent Operators for Rate Independent Elastoplasticity," *Computer Methods in Applied Mechanics and Engineering*, **48**, 101-119.
- Simo, J.C., and Hughes, T.J.R., (1998) *Computational Inelasticity*, Springer-Verlag, New York.
- Sousa, J.B., Weissman, S.L., Sackman, J.L., and Monismith, C.L., (1993) "A Nonlinear Elastic Viscous with Damage Model to Predict Permanent Deformation of Asphalt Concrete Mixes", *Transportation Research Record*, 1384, 80- 93.
- Tashman, L., Masad, E., Little, D., and Zbib, H. (2004), "Identification of Hot Mix Asphalt Permanent Deformation Parameters Using Triaxial Strength Tests and a Microstructure-Based Viscoplastic Continuum Model," *Transportation Research Board*, 83rd Annual Meeting, January 11-15, Washington, D.C.

THE HUET-SAYEGH MODEL; A SIMPLE AND EXCELLENT RHEOLOGICAL MODEL FOR MASTER CURVES OF ASPHALTIC MIXES

Adriaan C. Pronk¹

ABSTRACT: The applicability of the Huet-Sayegh (H&S) model is shown for different asphalt mixes. The H&S model with only six parameters simulates in an excellent way the behavior of asphalt mixes in cycling tests over a very wide range of frequencies. Examples are given of these perfect fits for three completely different asphalt mixes. The only disadvantage is that the original model does not contain a viscous element for simulating the permanent deformation in contrast with the more familiar Burger's model. However, by adopting a linear dashpot in series with the H&S model an attractive alternative for the Burger's model is obtained which can be used over a large frequency range. Special attention is given to the mathematical operations connected to the use of the H&S model.

INTRODUCTION

Today the Burger's model is one of the traditional models for the characterization of the rheological behaviour of bituminous mixes. However, at a chosen temperature this model describes the response on a loading quite well but only for a limited range of frequencies. If the frequency for a sinusoidal load is varied over a large range the values for the elements in the Burger's model have to be changed. This disadvantage hampers the development of relationships between the model parameters and mix properties. Also there is a need for simple but good models in analytical and finite element programs. C. Huet (1965) has developed another model with the aid of so called parabolic dashpots, which is valid over a very wide range of frequencies (Pronk 2003a).

¹ Rijkswaterstaat Road and Hydraulic Engineering Institute, Ministry of Transport, Public Works and Water Management, P.O. Box 5044, 2600 GA Delft, The Netherlands, a.d.pronk@dww.rws.minvenw.nl

HUET-SAYEGH (H&S) MODEL

The Parabolic or Variable Dashpot

The characteristic rheological element in the H&S model is the parabolic or variable dashpot. The mathematical operation for the variable dashpot is only defined for sinusoidal signals as (Pronk 2003b):

$$\sigma\{e^{i\omega t}\} = \eta\tau^{a-1}\Omega^a [\varepsilon\{e^{i(\omega t-\varphi)}\}] = \frac{\eta}{\tau} (i\omega\tau)^a \varepsilon\{e^{i(\omega t-\varphi)}\} \tag{1}$$

With $\sigma\{e^{i\omega t}\}$ is applied sinusoidal stress, $\varepsilon\{e^{i(\omega t-\varphi)}\}$ is the occurring sinusoidal strain, τ is a time decay constant, η is the viscosity and Ω is a special mathematical operator. Regarding Eq.1 the variable dashpot can be seen as a rheological element (for sinusoidal signals) between the linear spring (S.cos(φ); $a = 0$) and the linear dashpot (S.sin(φ); $a = 1$).

FIG 1. The response of a linear spring (X axis), a linear dashpot (Y axis), and a parabolic dashpot on a sinusoidal load.

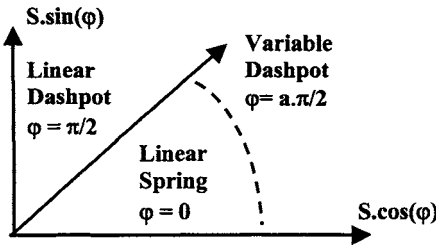
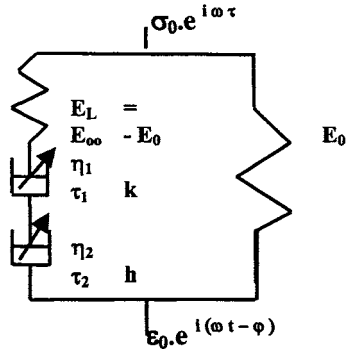


FIG 2. Scheme of the (general) H&S model



After a load the remaining deformation can be calculated with the aid of Eq. 2 (Pronk 1996) and will be zero for the variable dashpot if the parameter a is smaller than 1.

$$\varepsilon\{t \rightarrow +\infty\} = \lim_{\omega \rightarrow 0} \left[i\omega \cdot \left\{ \frac{1}{\eta \cdot \tau^{a-1} \cdot (i\omega)^a} \int_{-\infty}^{\infty} \sigma \cdot dt \right\} \right] = 0 \text{ for } 0 < a < 1 \tag{2}$$

The general H&S model

The H&S model (figure 2) looks like a Zener model but instead of one linear dashpot (Zener model) it has two variable or parabolic dashpots. For sinusoidal signals ($e^{i\omega t}$) the response equation of a general H&S model will be (see also Annex):

$$S(\omega) = E_0 + \frac{E_\infty - E_0}{1 + \delta_1 \cdot (i\omega\tau_1)^k + \delta_2 \cdot (i\omega\tau_2)^h} \tag{3}$$

with the following explanations:

$$\left. \begin{aligned} S\{\omega\} &= \text{complex stiffness [MPa]} \\ \omega &= \text{frequency [rad / s]}; \tau_{1,2} = \text{Time constants [s]}; \\ \delta_{1,2} &= \frac{\tau_{1,2} \cdot (E_\infty - E_0)}{\eta_{1,2}} = \text{Model parameters [-]} \\ E_0 &= S\{\omega \rightarrow 0\} \text{ [Pa]}; E_\infty = S\{\omega \rightarrow \infty\} \text{ [Pa]}; \\ I > h > k > 0; i &= e^{+i \cdot \frac{\pi}{2}} = \cos\left(\frac{\pi}{2}\right) + i \sin\left(\frac{\pi}{2}\right) = 0 + i \end{aligned} \right\} \tag{4}$$

This general model has six parameters and two time constants but C. Huet (1965) decreased the number by taking only one time constant $\tau = \tau_1 = \tau_2$ (a “popular” explanation is given in Annex) and one constant $\delta = \delta_1$ ($\delta_2 \equiv 1$). The response $S\{\omega\}$ can be rewritten as:

$$S\{\omega\} = E_0 + \frac{E_\infty - E_0}{A^2 + B^2} \cdot (A + B \cdot i) \tag{5}$$

$$A = I + \delta \cdot \frac{\cos(k \cdot \frac{\pi}{2})}{(\omega \cdot \tau)^k} + \frac{\cos(h \cdot \frac{\pi}{2})}{(\omega \cdot \tau)^h}; B = 0 + \delta \cdot \frac{\sin(k \cdot \frac{\pi}{2})}{(\omega \cdot \tau)^k} + \frac{\sin(h \cdot \frac{\pi}{2})}{(\omega \cdot \tau)^h} \tag{6}$$

Based on these formulas an Excel file has been made for a regression analysis. For this analysis four point-bending beam measurements (4PB tests) have been used at different frequencies and different temperatures. In contrast with the Burger’s model the temperature influence can be included quite easily by adopting only a simple relation for the time decay constant τ .

$$\tau = e^{A_1 + B_1 \cdot T + C_1 \cdot T^2} \tag{7}$$

In most cases the coefficient C_1 can be taken equal to zero (see figure 3). In order to convergence to realistic values a restriction is needed for the static modulus E_0 ($E_0 \geq 0$

MPa; default 1 MPa is adopted as a seed value). Without this restriction and if the measured curve doesn't have data at low frequencies and/or high temperatures the regression analysis (the solver option in Excel) might lead unrealistic negative E_0 values.

APPLICATION OF THE H&S MODEL (EXAMPLES)

The stiffness measurements are carried out with the aid of four point bending tests in controlled strain mode. The applied strain amplitude was 50 mm/m. A maximum of 500 cycles were applied before the next higher frequency chosen. After the last frequency the first (lowest) frequency was applied again in order to check that no substantial fatigue damage has been induced. In the following figures the fitting is shown with the H&S model for three different asphaltic mixes. Based on an integrated regression analysis procedure the figures presented in table 1 were calculated for the three asphalt mixes (ZOAB, Güss Asphalt, and GAB).

TABLE 1. Results of the integrated regression analysis for the three mixes

Asphalt Mix	E_0 [MPa]	E_∞ [MPa]	h [-]	k [-]	δ [-]	τ [s]		
						A_1 [-]	B_1 [1/°C]	C_1 [1/°C] ²
ZOAB	150	18,000	0.224	0.656	0.082	-5.1	-0.28	0.0014
Güss Asphalt	10	34,400	0.173	0.456	0.25	-4.5	-0.35	0.003
GAB	1	37,400	0.144	0.558	0.037	-5.1	-0.39	0.003

FIG 3. Results of the (separate) regression for a Porous Asphalt (ZOAB) Cole-Cole diagram

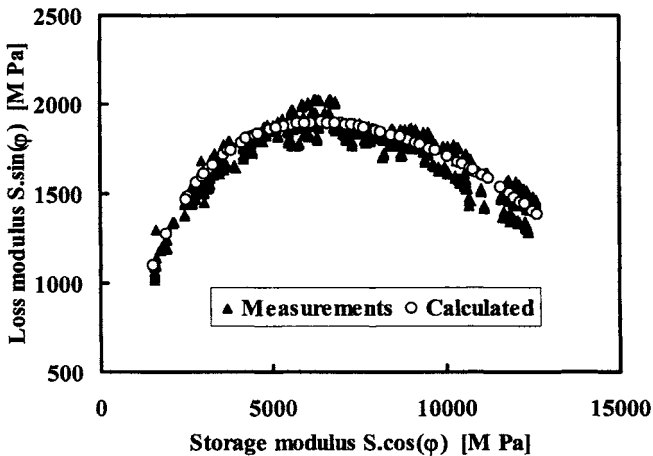
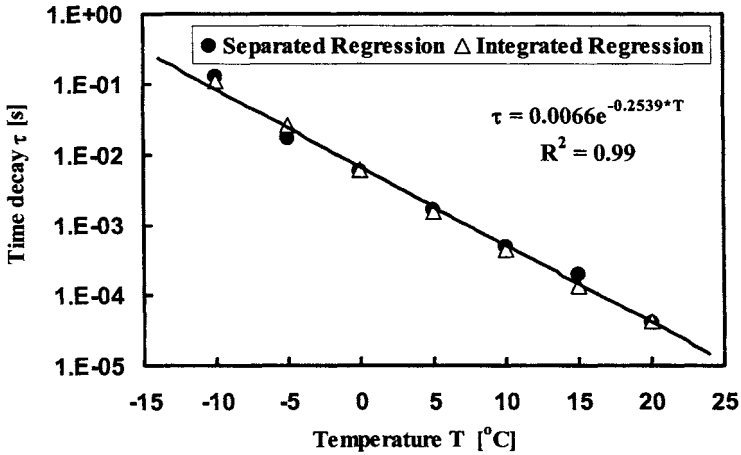


FIG 4. Results of the separate and integrated regression of τ as a function of temperature for a Porous Asphalt (ZOAB)



Porous Asphalt (ZOAB; very open graded mix)

This regression was carried out separately for all temperatures ranging from -10 to +20 °C. The frequency ranged from 5.9 to 58.6 Hz. At least 3 beams were tested. The complex stiffness modulus was measured between the 75th and 100th cycle. At that interval the target strain amplitude of 50 μm/m was always reached. The calculated time parameter τ is plotted in figure 4 as a function of the temperature. The same input data was also used for an integrated regression in which on forehand Eq. 7 was used for the τ dependency on the temperature. As clearly can be seen hardly no difference between these two regressions exists and that the regression coefficient C_1 in Eq. 7 can be omitted.

Güss Asphalt (penetration asphalt mix for dykes)

Güss Asphalt or in Dutch “Gietasfalt” is an asphalt mix used for (penetrating) sea dykes and steel bridges.. In figure 5 the frequency sweep measurements are given (at least three different beams were used per frequency; the frequency ranged from 5.9 to 58.6 Hz). The resulting master curves for stiffness and phase lag using the (integrated) H&S model are presented in figure 6. The stiffness and phase lag values are given as a function of the parameter $\omega \cdot \tau$ with $\tau = A_1 + B_1 \cdot T + C_1 \cdot T^2$ with T in °C. The constants A_1 , B_1 and C_1 follow from the integrated regression analysis.

FIG 5. Original frequency sweep data for a Güss Asphalt mix

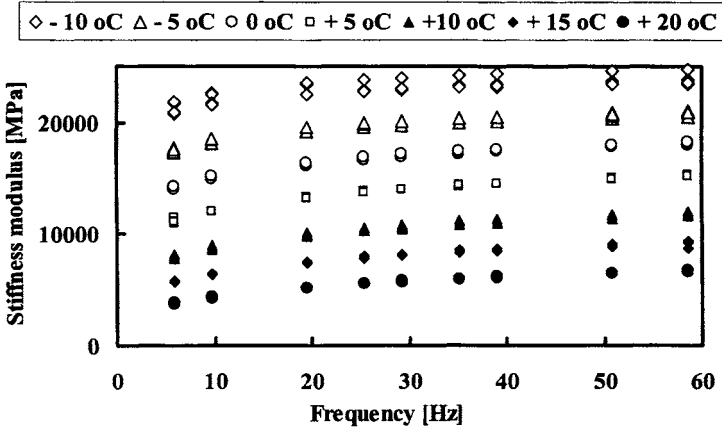
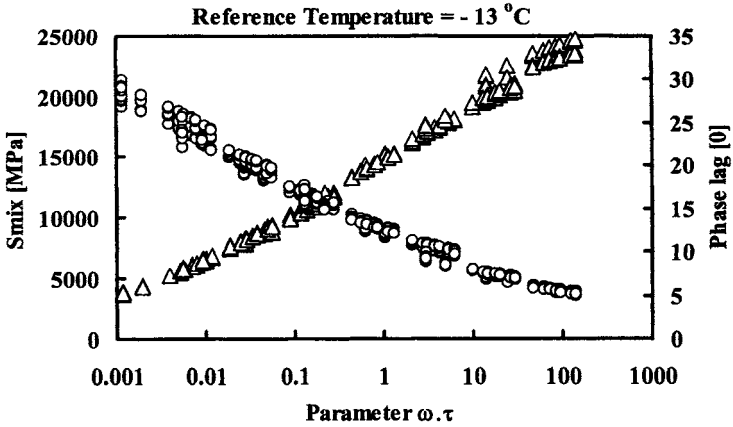


FIG 6. Master curves of the regression for a Güss Asphalt mix



Gravel Asphalt Concrete (GAB)

This asphalt mix was used in trial sections of the LINTRACK (Montauban 1988). The stiffness modulus is measured in a four point bending test (4PB) in controlled strain mode. The values are taken at cycle 22. The frequency ranges from 2 to 29.3 Hz. Four beams were tested in the frequency sweep (see figure 8). The temperature was varied from -10 to +30 °C. A regression line of the form $y = ax$ is plotted in the figures for

illustration. As clearly can be seen this regression line doesn't differ much from the equality line $y = x$.

FIG 7. Results of the (separate) regression for a Gravel Asphalt Concrete Calculated versus measured Stiffness modulus;

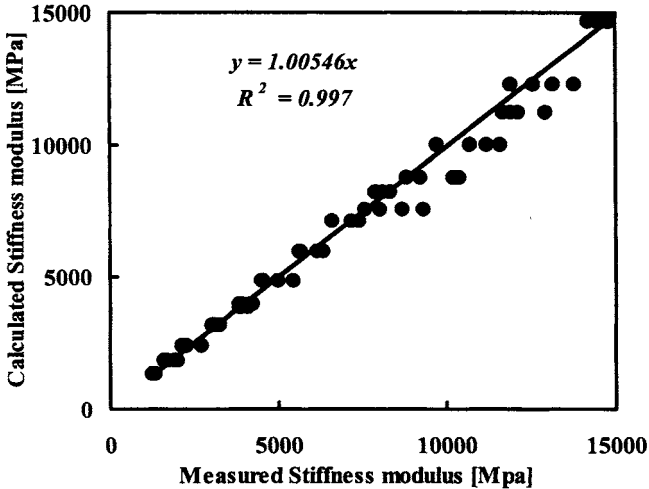
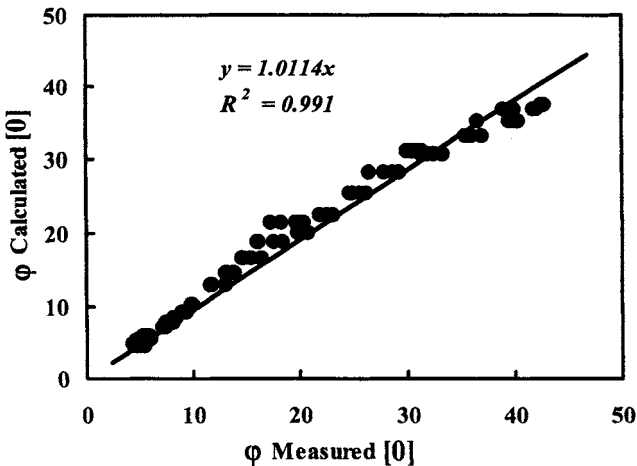


FIG 8. Results of the (separate) regression for a Gravel Asphalt Concrete Calculated versus measured Phase lag



CONCLUSIONS

1. Given the good results for the three investigated mixes it can be concluded that the H&S model is a simple but very good rheological model for the description of the master curves (stiffness and phase lag) for asphalt mixes with respect to the reversible response over a very wide range of frequencies.
2. Because most analytical linear visco-elastic models (like VEROAD) are based on the application of Fourier or Hankel transforms the H&S model can be applied quite easy in those response models (e.g. replacing the shear modulus G or even the bulk modulus K by the H&S model)
3. The H&S model doesn't contain irreversible (permanent) deformation like the Burger's model. However, viscous deformation can easily be included by adopting a linear dashpot in series with the H&S model.

REFERENCES

- Huet, C. (1965). "Étude, par une méthode d'impédance, du comportement viscoélastique des matériaux hydrocarbonés (Study of the viscoelastic behaviour of bituminous mixes by method of impedance)", Thesis, Faculté des sciences de l'université de Paris, Paris.
- Montauban, C.C. (1988). "Construction asphalt pavement GAB trial section (MEVA-3)", Report MAO-R- 89005, RHED, Delft (in Dutch).
- Pronk, A.C. (1996), "Some notes on the Fourier Transform application in VEROAD with respect to permanent deformation", W-DWW-96-065, DWW, Delft.
- Pronk, A.C. (2003a), "Revival of the Huet-Sayegh Response Model - Notes on the Huet-Sayegh Rheological Model", DWW-2003-029, RHED, Delft.
- Pronk, A.C. (2003b). "The Variable Dashpot", DWW-2003-030, RHED, Delft.

ANNEX THE HUET-SAYEGH MODEL

Comparison between the H&S, Burger's and Zener model

First of all a short description of the Zener model will be given. The Zener model consists out of a linear spring E_1 in series with a circuit of a parallel linear spring E_2 and a linear dashpot η_2 . In fact it is a Burger's model without the serial linear dashpot η_1 . By the so-called Z transform the Zener model is equivalent to a circuit of a linear spring E_1^* parallel to a series of a linear dashpot η_2^* and a linear spring E_2^* . In this form it resembles an H&S model with one linear dashpot. Both the Zener model and H&S model do not have a permanent deformation element. The permanent deformation in the Burger's model is represented by the serial dashpot η_1 .

Another big difference between the Zener and Burger's model at one hand and the H&S model at the other hand is the difference in the behaviour of the master curves for $\omega \rightarrow \infty$ and for $\omega \rightarrow 0$.

In the Zener and Burger's model the angle is 90° while in the H&S model these angles depend on the parameters h and k and differ from each other (ref. 1; figure 26)

H&S Model

The response (transfer function) for the H&S model is given in Eq. A1 in which the spring in line with the two variable dashpots is denoted by E_L .

$$\sigma = \varepsilon \cdot \left(E_o + E_L \cdot \frac{1}{1 + \frac{E_L \cdot \tau}{\eta_1 \cdot (i\omega\tau)^k} + \frac{E_L \cdot \tau}{\eta_2 \cdot (i\omega\tau)^h}} \right) \quad (\text{A1})$$

For $\omega \rightarrow 0$ the response equals E_0 and for $\omega \rightarrow \infty$ Huet denoted the response by E_∞ . To obtain this answer the spring E_L has to be equal to $E_L = E_\infty - E_0$. For the response of the original H&S model C. Huet also adopted a relationship between η_2 , E_∞ , E_0 , and τ , which reduces the amount of independent variables. Eq. A1 can be rewritten as:

$$\sigma = \varepsilon \cdot \left(E_o + (E_\infty - E_o) \cdot \frac{1}{1 + \delta \cdot (i\omega\tau)^{-k} + (i\omega\tau)^{-h}} \right) \quad (\text{A2})$$

The relationship between η_2 , E_∞ , E_0 , and τ and the definition of the parameter δ are given by Eq. A3.

$$\eta_2 = (E_\infty - E_o) \cdot \tau \quad ; \quad \eta_1 = \frac{(E_\infty - E_o) \cdot \tau}{\delta} \quad (\text{A3})$$

In a more general model one can have two δ and two τ parameters (Eq.A4).

$$\eta_1 = \frac{(E_\infty - E_o) \cdot \tau_1}{\delta_1} \quad ; \quad \eta_2 = \frac{(E_\infty - E_o) \cdot \tau_2}{\delta_2} \quad (\text{A4})$$

The H&S model is thus a simplification of a more general model. However, it seems logical to adopt only one τ parameter ("time decay constant"). The differential equation for this model with two linear dashpots is given in Eq. A5.

$$\frac{1}{E_L} \cdot \frac{d}{dt} \sigma + \left(\frac{1}{\eta_1} + \frac{1}{\eta_2} \right) \cdot \sigma = \left(\frac{E_o}{E_L} + 1 \right) \cdot \frac{d}{dt} \varepsilon + E_o \cdot \left(\frac{1}{\eta_1} + \frac{1}{\eta_2} \right) \cdot \varepsilon \quad (\text{A5})$$

The solution of the homogenous differential equation ($\sigma = 0$) gives only one time decay constant (Eq. A6):

$$\tau = \frac{E_o + E_L}{E_L \cdot E_o} \cdot \frac{\eta_1 \cdot \eta_2}{\eta_1 + \eta_2}; \quad E_o + E_L = E_\infty \quad (\text{A6})$$

If the operator Ω^a is used as a “normal” differential operator Eq. A7 will be obtained for the homogenous “differential” equation of the general H&S model:

$$\left(1 + \frac{E_o}{E_L}\right) \cdot \frac{d}{dt} \varepsilon + \frac{E_o}{\eta_1 \cdot \tau_1^{k-1}} \cdot \frac{d^{1-k}}{dt^{1-k}} \varepsilon + \frac{E_o}{\eta_2 \cdot \tau_2^{h-1}} \cdot \frac{d^{1-h}}{dt^{1-h}} \varepsilon = 0 \quad (\text{A7})$$

Notice that for a “positive” exponent of the differentiation both parameters h and k have to be less than 1. The solution of this type of differential equations can be obtained by filling in Eq. A8. Mark the minus sign in the exponent.

$$\varepsilon = \varepsilon_o \cdot e^{\frac{t}{\tau}} \Rightarrow -\left(1 + \frac{E_o}{E_L}\right) \cdot \frac{1}{\tau} + \frac{E_o}{\eta_1 \cdot \tau_1^{k-1}} \cdot \frac{(-1)^{1-k}}{\tau^{1-k}} + \frac{E_o}{\eta_2 \cdot \tau_2^{h-1}} \cdot \frac{(-1)^{1-h}}{\tau^{1-h}} = 0 \quad (\text{A8})$$

It seems logical to take τ equal to τ_1 and τ_2 . In that case Eq. A8 becomes similar to Eq. A5 with ($\sigma = 0$). In order to reduce the number of independent variables C. Huet (1965) adopted a relationship for the parameters of the second dashpot.

PARTIAL HEALING, A NEW APPROACH FOR THE DAMAGE PROCESS DURING FATIGUE TESTING OF ASPHALT SPECIMEN

Adriaan C. Pronk¹

ABSTRACT: Earlier findings in fatigue tests using a repeated sequence of a fixed number of cycles with a high deflection and a fixed number of cycles with a small deflection confirms the supposition that healing of the stiffness already occurs during the fatigue test and does not depend on a rest period of no loading at all. It was shown by theory and in practice that the decrease in temperature due to the decrease in dissipated energy per cycle when smaller strains were applied could not explain the amount of increase in the stiffness modulus. Further investigation of these findings and results has lead to a new *material* response model that describes both the evolution of the modulus and the phase lag of the complex stiffness model during fatigue testing. It should be marked that healing in this paper is only related to the complex stiffness modulus. This partial healing (PH) model is a material model for which the response in a point depends on the stress/strain state in that point (the rate of dissipated energy). Therefore the application of the PH model for the determination of the response (evolution of stiffness) of a finite specimen in a test will depend on the geometry and loading configuration of the specimen and the load mode. The PH model is applied on four point bending beam tests (4PB) in controlled deflection mode. The obtained parameters for the PH material model were used for the prediction of the stiffness evolution in uni-axial push-pull fatigue tests (UPP) on the same asphalt mix. A fair comparison was observed between the measured and predicted evolution of both the modulus and phase lag of the complex stiffness modulus in the UPP tests.

¹ Rijkswaterstaat Road and Hydraulic Engineering Institute, Ministry of Transport, Public Works and Water Management, P.O. Box 5044, 2600 GA Delft, The Netherlands, a.d.pronk@dww.rws.minvenw.nl

INTRODUCTION

The healing effect is normally investigated by applying rest periods during a fatigue test (Bonnaure, 1982; Bazin, 1967). The increase in fatigue life is related to the ratio of loading time and rest time (Verstraeten, 1982). Quite another approach is the visco-elastic correspondence principle (Schapery, 1984). This principle is used in tests with a haversine waveform and saw-tooth waveform (Kim, 1994). In all these investigations the effect of healing was studied by applying real rest periods. The authors quoted, however, did not consider the possibility of healing occurring in a loading period without rest periods. However, if instead of a real rest period a pseudo rest period is applied with lower strain amplitude it has been shown that the stiffness also increases during these pseudo rest periods (Pronk, 1997). This implies that the phenomenon of healing should be directly incorporated in the interpretation of fatigue tests with respect to the evolution of the stiffness modulus and phase lag.

Next to the fatigue damage (creation of micro defects etc.) the stiffness modulus of the material will also decrease due to the heating of the specimen by the (thermal) dissipated energy per cycle. If the tests are carried out in a temperature chamber with a good thermal condition (forced convection) the temperature increase of the specimen will be limited and as a consequence the decrease in stiffness due to heating can be neglected for normal strain values (below 250 micro strain) (Pronk, 1996a; Pronk, 1996b).

In the paper a model will be presented which makes it possible to describe the evolution of the stiffness modulus during the fatigue test very well. It is assumed that the asphalt mix can be considered as a linear viscoelastic material. This model can be used to predict the evolution of the stiffness modulus for other loading conditions as well as the healing (in stiffness modulus) after a rest period. It should be noticed that the PH model is related to the evolution of the complex stiffness modulus in cyclic bending tests only and not to the "fatigue strength or resistance" of the material. Although in many papers the fatigue life of a specimen is related to a certain reduction in the modulus of the complex stiffness modulus (e.g. 50 %; $N_{f,50}$).

PROPOSED MODEL

The dissipated energy per cycle ΔW_{tot} (calculated from the applied force P , the obtained deflection W and the phase lag ϕ' between force and deflection) can be split up into three parts:

- System losses per cycle ΔW_{syst}
- Visco-Elastic losses per cycle ΔW_{dis}
- Fatigue consumption per cycle ΔW_{fat}

If good equipment is used the system losses ΔW_{syst} can be ignored. In fact to the author's knowledge this term is never used in the calculations of strains ϵ and stresses σ from the applied force and measured deflection. A small difference between the phase lag ϕ' and the phase lag ϕ (between stress and strain) is obtained if mass inertia effects are taking into account in the processing formulas (Pronk, 1996c). But this difference will not result in system losses. In the normal interpretation and processing of bending tests the influences of shear forces are neglected. The same approach is followed here. The visco-elastic losses per cycle ΔW_{dis} are represented by the well-known formula for sinusoidal loadings:

$$\Delta W_{dis} = \pi \epsilon \sigma \sin(\phi) . \quad (1)$$

This amount of dissipated energy is completely transformed into heat. In case of the fatigue initiation phase an expression for the fatigue damage ΔW_{fat} is not known and is not taken into account in the processing formulas for the calculations of strains and stresses. This implies that the calculated strains and stresses are in principal wrong (overestimated) but the mistake made is negligible. In the proposed model it is assumed that next to the decrease in fatigue strength (remaining fatigue life) the fatigue consumption ΔW_{fat} is also responsible for the decrease in the stiffness modulus and the increase in the phase lag during the fatigue test. Furthermore it is proposed that the fatigue consumption ΔW_{fat} can be regarded as a very small portion of the visco-elastic losses ΔW_{dis} . The next step is the introduction of a stiffness damage term Q that is directly related to the fatigue consumption ΔW_{fat} .

$$Q \text{ is related to } \Delta W_{fat} \text{ is related to } \Delta W_{dis} \Rightarrow \frac{d}{dt} Q = \frac{d}{dt} \delta \cdot W_{dis} \approx \delta \frac{\Delta W_{dis}}{T} \quad (2)$$

With T = time of one cycle. Based on the findings in an earlier project (Pronk, 1997) it was concluded that at least a part of the damage Q created at time t will diminish in time. This implicates that healing as a phenomenon will occur always regardless the presence of a real rest period. The last step is the assumption that the stiffness damage Q effects both the imaginary part (Loss Modulus) $F = S \cdot \sin(\varphi)$ and the real part (Storage Modulus) $G = S \cdot \cos(\varphi)$ of the complex stiffness S according to:

$$F\{t\} = F_o - \int_0^t \frac{dQ\{\tau\}}{d\tau} \left[\alpha_1 \cdot e^{-\beta \cdot (t-\tau)} + \gamma_1 \right] \cdot d\tau \quad (3)$$

$$G\{t\} = G_o - \int_0^t \frac{dQ\{\tau\}}{d\tau} \left[\alpha_2 \cdot e^{-\beta \cdot (t-\tau)} + \gamma_2 \right] \cdot d\tau \quad (4)$$

The terms with the parameters α_1 and α_2 of the damage will be ‘healed’ in time with time decay β . The terms with the parameter γ_1 and γ_2 will not heal (partial healing model). In case of strain controlled mode the fatigue damage rate is given by Eq. 5:

$$\frac{dQ\{\tau\}}{d\tau} \approx \frac{\delta \cdot \Delta W_{dis}}{T} = \frac{\delta \cdot \int_0^T \sigma \cdot \frac{d\varepsilon}{d\tau} \cdot d\tau}{T} = \delta \cdot \pi \cdot \varepsilon_0^2 \cdot S\{\tau\} \cdot \sin(\varphi\{\tau\}) \cdot f = \delta^* \cdot S\{\tau\} \cdot \sin(\varphi\{\tau\}) = \delta^* \cdot F\{\tau\} \quad (5)$$

with f = frequency [Hz]; σ = stress [Pa]; ε_0 = strain [m / m]

The complete solutions of equations (3) and (4) are given in reference (Pronk, 2000). From earlier tests (Pronk, 1997) it is noticed that in 4PB tests no healing occurs for the imaginary part or at least it is negligible for the investigated mixes. Therefore the parameter α_1 is set equal to zero, which simplifies the equations considerable and leads to the following solution.

$$F\{t\} = S \cdot \sin(\varphi) = S_0 \cdot \sin(\varphi_0) \cdot e^{-\gamma_1 t} \quad (6)$$

$$G\{t\} = S \cdot \cos(\varphi) = S_0 \cdot \cos(\varphi_0) - S_0 \cdot \sin(\varphi_0) \cdot \left(\frac{\alpha_2^*}{\beta - \gamma_1} \cdot \{e^{-\gamma_1 t} - e^{-\beta t}\} + \frac{\gamma_2^*}{\gamma_1} \cdot \{1 - e^{-\gamma_1 t}\} \right) \quad (7)$$

$$\text{With } \alpha_2^* = \delta^* \cdot \alpha_2 \text{ and } \gamma_1^* = \delta^* \cdot \gamma_1; \gamma_2^* = \delta^* \cdot \gamma_2 \quad [\text{note: } \delta^* :: \varepsilon_0^2] \quad (8)$$

It should be noticed that the model as described above is in principle a *material* model. If it is applied to a specimen the dimensions of the specimen and the stress-strain distribution must be taken into account. For a bending beam test in which the obtained figures for stresses and strains are based on the curvature of the bended surface (maximum values) it implies that the obtained values for the parameters α_1 , α_2 , β , γ_1 and γ_2 will be lower. In case γ_1 equals zero, the dissipated energy per cycle will stay constant ($S \cdot \sin(\varphi)$ is constant). When γ_2 also equals zero the stiffness modulus S will reach a limit given by Eq. 9. This phenomenon is observed at low strain values.

$$S_{t \rightarrow \infty} = S_0 \cdot \sqrt{\left[\cos(\varphi_0) - \sin(\varphi_0) \cdot \frac{\alpha_2^*}{\beta} \right]^2 + \sin^2(\varphi_0)} \quad (9)$$

APPLICATION OF THE MODEL ON 4PB TESTS

The healing model is applied on four point bending tests, which were carried for a fatigue experiment (comparison of different fatigue tests) of the RILEM PEB TG 3 group (Pronk, 1999). The fatigue tests were performed at 9.8 Hz and 10 °C in controlled displacement (strain) mode. The target strain amplitude levels were 140, 180 and 220 micro strains. For each level four repetitions were carried out. The dimensions of the specimens were: total length 450 mm (effective length between the two outer clamps is 400 mm), height and width 50 mm. The distance between the two inner clamps is 130 mm. An overview of results is given in table 1. The initial values for the stiffness modulus and phase lag are taken from the readings at cycle 100. The fatigue life N_1 is determined as the number of cycles at which a sharp change in the dissipated energy per cycle occurs (Hopman, 1989; Pronk, 1990; Pronk, 1995) and $N_{f,50}$ is the traditional fatigue life defined as the number of cycles at which the stiffness modulus has decreased to half its initial value. The scatter in the fatigue lives N_1 and $N_{f,50}$ for equal strain amplitude levels is high but not unusual for fatigue tests. Per individual test the model parameters together with the initial values for the stiffness modulus and phase lag were determined from a regression fit using the measured values on the interval from N_0 (at which the strain amplitude remains constant) to $N = N_1$ cycles. Normally N_0 is around 100 cycles. The obtained values for all specimens are given in table 2.

The obtained figures for γ_1 δ do not vary a lot. The values range from 4.1 to 8.1 (except the figure of 16.3 obtained for test 0-503). Also the figures for γ_2 δ are more or less constant. At the other hand the variations in α_2 δ and β are rather large. This is due to the fact that the exponential term with β is much smaller than the exponential term with γ_1 . This effects the sensitivity of the determination leading to a more or less constant figure for the coefficient $\alpha_2/(\beta \cdot \gamma_1)$. After a detailed study it could be concluded that specimens 0-501 and A-501 were outliers (Pronk, 2000). In all other tests the evolutions of the stiffness modulus and phase lag could be described by

taking constant values for $\alpha_2 \delta$ and $\gamma_1 \delta$ and a strain dependent value for β . In table 3 the calculated values are given for the model parameters.

TABLE 1. Fatigue results of four point bending tests in controlled strain mode with sinusoidal loading at 10°C and 9.8 Hz

Beam	Density (kg/m ³)	Strain (μm/m)	N ₁ (kc)	N _{f,50} (kc)	S _{initial} (MPa)	Φ _{initial} (°)
0-501	2444	137	510	1,200	9,740	18.15
0-503	2454	218	48	111	9,694	18.77
0-504	2403	177	170	345	10,306	16.46
A-501	2397	137	400	1,020	9,488	18.32
A-503	2450	178	130	265	10,526	17.12
A-504	2381	217	42	88	9,669	18.03
A-601	2351	138	200	430	9,881	16.69
A-602	2436	219	90	200	10,175	18.05
A-604	2420	179	160	276	10,613	17.20
B-601	2405	218	120	200	10,357	17.06
B-602	2472	137	270	465	10,757	16.93
B-603	2444	177	120	215	10,639	17.14

TABLE 2. Results of the regression on each test separately

Beam	$\alpha_2 \delta$ (-)	$\gamma_2 \delta$ (-)	β (10 ⁻⁵ s ⁻¹)	$\gamma_1 \delta$ (-)	ϵ_0 (μm/m)
0-501	24.7	14.1	8.49	3.77	137
0-503	54.8	73.6	243	16.30	218
0-504	399	30.7	83	4.17	177
A-501	6.37	21	99.7	4.30	137
A-503	457	36	114	5.14	178
A-504	666	28.8	114	5.29	217
A-601	790	38	143	5.30	138
A-602	1490	33.7	562	5.91	219
A-604	511	37.8	124	7.62	179
B-601	282	36.3	126	8.14	218
B-602	461	34.1	80.5	6.65	137
B-603	569	39.9	156	6.56	177

The values for the model parameter β are given in figure 1 as a function of the applied strain amplitude level. The fact that β depends on the strain amplitude can be explained in a way. Temperature will activate a healing process and although rather small the temperature increase is higher at higher strain levels (more viscous dissipated energy per cycle) and likewise the effect of healing. Examples of the comparisons between measured and calculated evolutions are given in figures 2 to 4. In fact the presented comparisons were the worst of all comparisons.

TABLE 3. Results of the regression on all tests (except 0-501 and A-501) assuming that only β depends on the strain amplitude and all other model parameters are material constants

Strain ($\mu\text{m/m}$)	$\alpha_2 \cdot \delta$ (-)	$\gamma_2 \cdot \delta$ (-)	β (10^{-5} s^{-1})	$\gamma_1 \cdot \delta$ (-)
137	618	36.42	111	6.60
177	618	36.42	146	6.60
217	618	36.42	248	6.60

FIG. 1. Calculated model parameter β as a function of the strain amplitude ϵ_0 [$\mu\text{m/m}$] assuming a constant value per strain level. Tests 0-501 and A-501 are not taken into account. [mark that ϵ is in $\mu\text{m/m}$ for the regression]

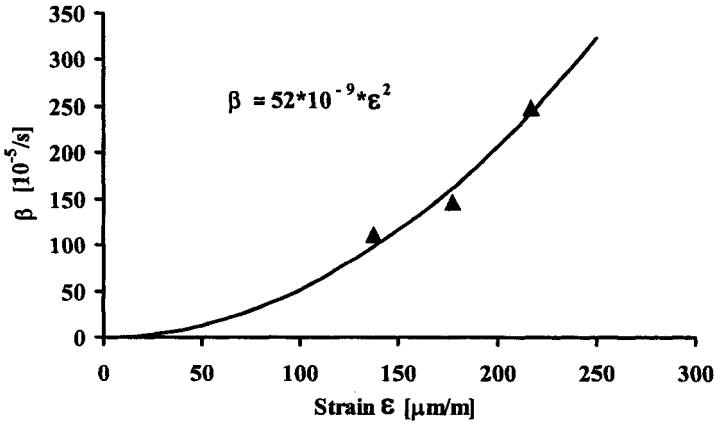


FIG. 2. Measured and calculated evolutions for 0-504 ($\epsilon = 177 \mu\text{m/m}$). Calculation based on the parameter data of table 3.

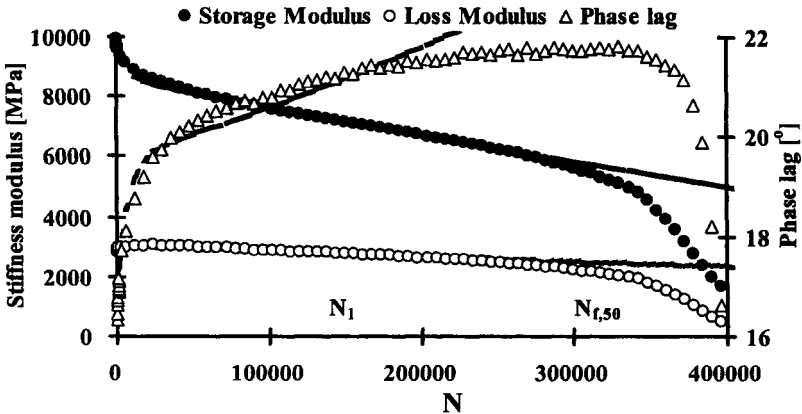


FIG. 3 Measured and calculated evolutions for A-601 ($\epsilon = 138 \mu\text{m/m}$). Calculation based on the parameter data of table 3.

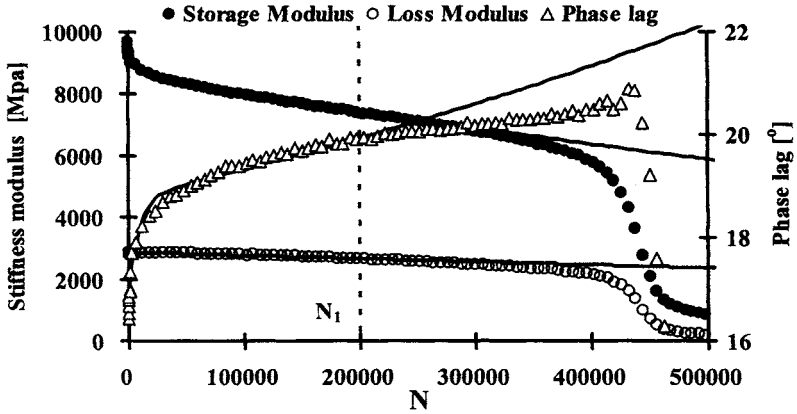
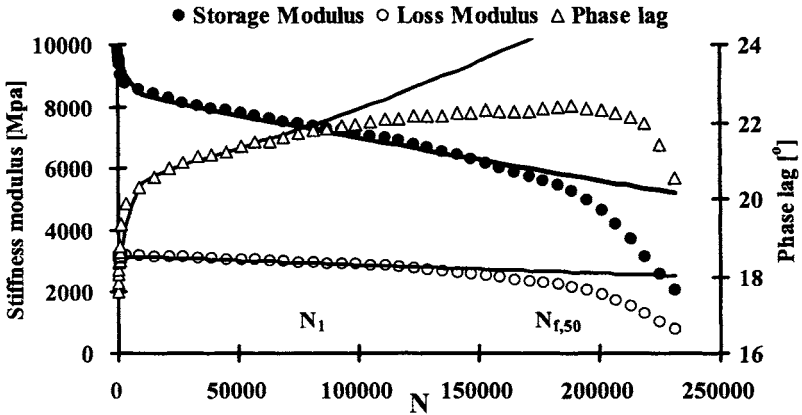


FIG 4. Measured and calculated evolutions for A-602 ($\epsilon = 219 \mu\text{m/m}$). Calculation based on the parameter data of table 3.



APPLICATION OF THE MODEL TO UPP TESTS

One way to verify the validity of the PH model is to apply this model to other fatigue tests. The PH₁ model is assumed to be a *material* model. Therefore the values for the parameters $\alpha_1, \alpha_2, \beta, \gamma_1$ and γ_2 will depend on the stress-strain distribution in side the specimen of the test at issue. The procedure how values of the parameters for the PH model may be obtained in case of uni-axial push-pull (UPP) tests is explained in Annex A. In fact the UPP test should be used as the basic test for the

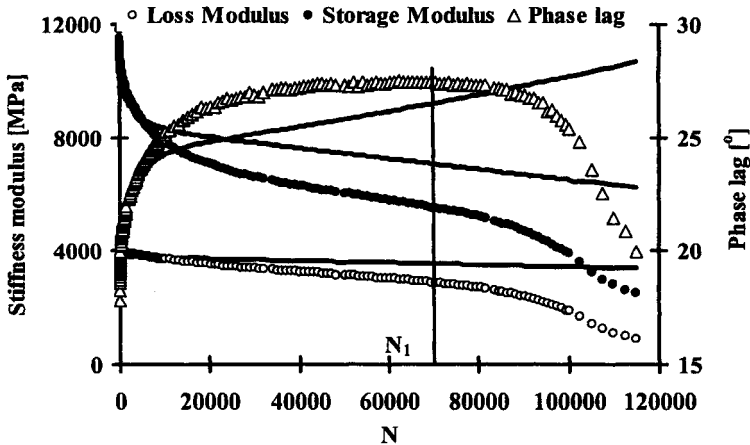
development of the PH model because the strain distribution in a cross-section will be constant (in theory) in contrast with a 4PB test or other bending devices.

The asphalt mix, which was used for the 4PB tests, was also used in strain controlled uni-axial push-pull tests (UPP) on cylindrical specimens with a height of 0.10 m and a diameter of 0.08 m (Pronk, 2000a). In theory these tests are homogenous with respect to the stress-strain distribution. However, in practice it is nearly impossible to remain a good constant strain distribution in a cross-section during the whole test. Only two tests could be used for this kind of validation. Based on the values (table 4) deduced from the 4PB tests (see Annex) the calculated evolutions for these two tests are given in figures 5 and 6.

TABLE 4. Calculated parameter values for the UPP tests from the 4PB regressions (Annex)

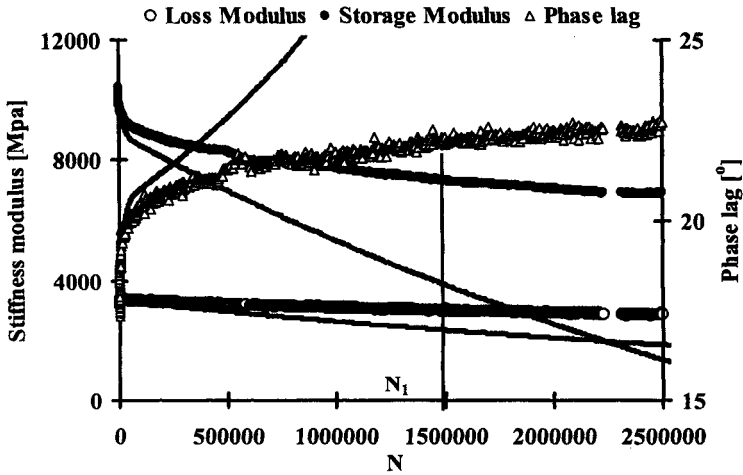
Cylinder	Strain [$\mu\text{m/m}$]	$\alpha_2 \cdot \delta$ (-)	$\gamma_2 \cdot \delta$ (-)	β (10^{-5} s^{-1})	$\gamma_1 \cdot \delta$ (-)
E13D180-17	172.5	1030	60.7	258	11
E13D80-14	82	1030	60.7	58	11

FIG. 5 Comparison of calculated and measured evolutions in UPP test E13D 180-17 using parameter values of table 5.



As clearly shown in figures 5 and 6 the approximated parameter values based on 4PB tests (see Annex) for the model evolution in UPP tests leads for test E13D 80-17 ($\epsilon_0=172.5 \mu\text{m/m}$) to a too optimistic performance and for test E13D 80-14 ($\epsilon_0=82 \mu\text{m/m}$) to an overestimation of the fatigue damage. Regarding the evolution of the loss modulus for UPP test E13D 180-17 the coefficient γ_1 is much too low while for test E13D 180-14 this coefficient is too high.

FIG. 6 Comparison of calculated and measured evolutions in UPP test E13D 180-14 using parameter values of table 4.



Another point is the relation of the parameter β with the strain amplitude. This parameter represents the healing, which according to the author is more related to the temperature and the temperature profile in a cross-section. For equal maximum strain amplitudes these temperature profiles do not differ much in a 4PB test and in an UPP test (Pronk, 1996b). Therefore a regression is carried out for the two UPP tests in which the parameter β was preset using the fit equation in figure 1. The calculated values for the parameters are given in table 5. A much better comparison is now obtained as shown in figures 7 and 8.

TABLE 5. Results of the regressions for UPP tests

Cylinder	$\alpha_2 \cdot \delta$ (-)	$\gamma_2 \cdot \delta$ (-)	β ($10^{-5} s^{-1}$)	$\gamma_1 \cdot \delta$ (-)
E 13 D 180-17	1350	131	155	49.8
“4PB test”	618	36.4	155	6.6
E13D80-14	608	18.2	35	3.4
“4PB test”	618	36.4	35	6.6

FIG. 7 Comparison of calculated and measured evolutions in UPP test E13D 180-17 using parameter values of table 5.

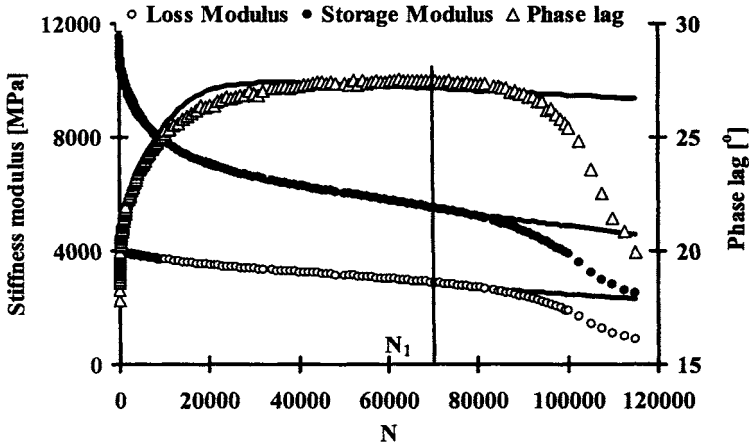
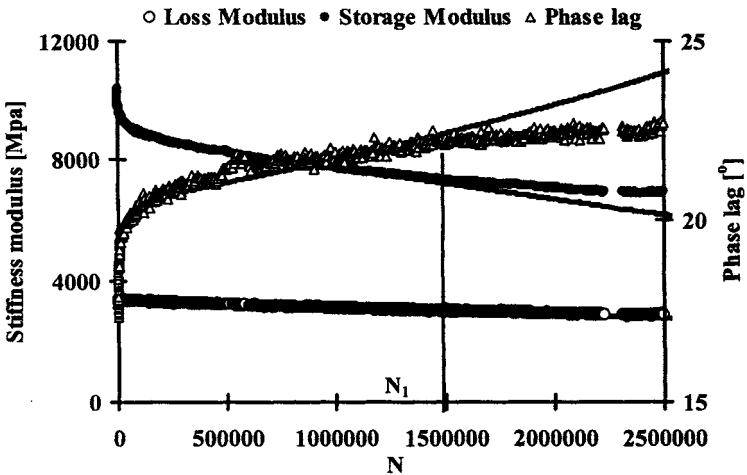


FIG. 8 Comparison of calculated and measured evolutions in UPP test E13D 180-14 using parameter values of table 5.



CONCLUSIONS

It is yet to early to draw firm conclusions. Nevertheless the presented partial healing model shows large potentials and it can explain on a sound base the

evolutions of the stiffness modulus and phase lag in 4PB tests very well. The PH model will also fit the evolutions in an UPP test. However, estimations of all the parameter values for an UPP test using the results from 4PB tests are yet not fully established. The following preliminary conclusions can be drawn

- The parameters $\alpha_2 \cdot \delta$ and $\gamma_{1,2} \cdot \delta$ can be considered as constants in a 4PB tests.
- The parameter β in a 4PB test depends on the applied strain amplitude. The calculated value increases with strain amplitude, which is logical because a higher strain means more dissipated energy. This leads to a 'higher' temperature, which increases the healing capacity. And this resembles itself by bigger time decay constant β . It seems that β is related to the temperature profile in the test.
- The model is applicable for describing the evolution of the complex stiffness in 4PB and UPP tests. However, simple first order estimation for all the parameters in an UPP test based on 4PB measurements fails.
- At high strain amplitudes (170 mm/m) the fatigue damage rate in an UPP test is more severe compared with a 4PB test with the same maximum strain value.

REFERENCES

- Bazin P. et al, (1967), "Deformability, fatigue and healing properties of asphalt mixes", Proc. 2nd Intern. Conf. on the Struct. Design of Asphalt Pavements, Ann Arbor, Michigan.
- Bonnaure F.P. et al, (1982), "A laboratory investigation of the influence of rest periods on the fatigue characteristics of bituminous mixes", Annual meeting of the Association of Asphalt Paving Technologists, Kansas City, Missouri.
- Hopman P.C. et al, (1989), "A renewed interpretation method for fatigue measurements - Verification of Miner's rule", Proc. of the 4th Eurobitume Symposium, Madrid, Spain.
- Kim Y.R. et al, (1994), "Healing in asphalt concrete pavements: Is it real?", 73rd Annual meeting Transportation Research Board, Washington, D.C., 1994
- Pronk A.C. et al, (1990), "Energy dissipation: The leading factor of fatigue", Proc. Strategic Highway Research Program: Sharing the Benefits, London, England, 1
- Pronk A.C., (1995), "Evaluation of the dissipated energy concept for the interpretation of fatigue measurements in the crack initiation phase", Report P-DWW-95-001, DWW, Delft, The Netherlands.
- Pronk, A.C. et al, (1996a), "Temperature increase in an asphalt beam during fatigue; theory and practice", Proc. Wegbouwkundige Werkdagen 1996, CROW, Ede, The Netherlands, ISBN 90-6628-221-5.
- Pronk, A.C., (1996b) "Analytical description of the heat transfer in an asphalt beam, tested in the 4 point bending apparatus", Report: W-DWW-96-006, DWW, Delft, The Netherlands.
- Pronk, A.C., (1996c), "Theory of the four point dynamic bending test", Report: P-DWW-96-008, Delft, The Netherlands.
- Pronk A.C., (1997), "Healing during fatigue in 4 point dynamic bending tests", Report: W-DWW-97-095, DWW, Delft, The Netherlands.
- Pronk A.C., (1999), "Four point bending tests - RILEM PEB - WG3", Report W-DWW-99-059, DWW, Delft, The Netherlands.
- Pronk, A.C., (2000), "Partial healing model - Curve fitting", Report W-DWW-2000-047, DWW, Delft, The Netherlands.
- Pronk, A.C., (2000a), "Uniaxial Push-Pull tests (UPP) of ENTPE (Fr)-Review of the measured data and interpretation-Application of the PH model", Report DWW RILEM 152 WG3.
- Schapery, R.A., (1984), "Correspondence principles and a generalized J-integral for large deformation and fracture analysis of visco-elastic media", Intern. Journ. of Fracture, vol. 25.

Verstraeten, J. et al, (1982), "Rational and practical designs of asphalt pavements to avoid cracking and rutting", Proc. 5th Intern. Conf. on the Struct. Design of Asphalt Pavements, Delft, The Netherlands.

ANNEX "Weighing Procedure"

In the 4PB test one measures the beam stiffness E.I instead of a *material* stiffness modulus. Therefore a weighed stiffness modulus will be calculated from bending beam measurements if the evolution of the material stiffness modulus becomes a function of the location in the specimen during the test. In this case only the midsection of the 4PB test (constant moment) will be taken into account. If the material stiffness modulus depends on the distance x to the neutral axis in the beam, the weighed stiffness modulus will be given by:

$$\bar{E} = 3 \cdot \int_0^1 [E\{x\} \cdot x^2] dx \quad A1$$

The starting point for the weighing procedure are Eq.3 and 4 and replacing the parameters α_1 , α_2 , β , γ_1 and γ_2 by $A_1 \cdot x^2$, $A_2 \cdot x^2$, $B \cdot x^2$ (see figure 1), $C_1 \cdot x^2$ and $C_2 \cdot x^2$. Eq. A2 and A3 are the solutions of the PH model for the evolution of the complex stiffness modulus in an UPP test.

$$F\{t\} = S \cdot \sin(\varphi) = S_0 \cdot \sin(\varphi_0) \cdot e^{-C_1^* \cdot t \cdot x^2} \quad A2$$

$$G\{t\} = S \cdot \cos(\varphi) = S_0 \cdot \cos(\varphi_0)$$

$$- S_0 \cdot \sin(\varphi_0) \left(\frac{A_2^*}{B - C_1^*} \cdot \left\{ e^{-C_1^* \cdot t \cdot x^2} - e^{-B \cdot t \cdot x^2} \right\} + \frac{C_2^*}{C_1^*} \cdot \left\{ 1 - e^{-C_1^* \cdot t \cdot x^2} \right\} \right) \quad A3$$

If the decrease in the loss modulus $S \cdot \sin(\varphi)$ is very small it is allowed to take the first order approximation for the exponential term in Eq. A2. Eq. A4 gives the (beam) loss stiffness modulus, which would be measured in a 4PB test applying the same (maximum) strain amplitude.

$$\overline{F\{t\}} = 3 \cdot \int_0^1 S \cdot \sin(\varphi) \cdot x^2 \cdot dx = 3 \cdot \int_0^1 S_0 \cdot \sin(\varphi_0) \cdot [1 - C_1^* \cdot t \cdot x^2] \cdot x^2 dx \quad A4$$

Eq. A4 will be equal to the first order approximation of Eq. 1 for the 4PB test if $\gamma_1^* = (3/5) \cdot C_1^*$. In reverse the coefficients C_1^* can be estimated using 4PB tests by multiplying γ_1^* with a factor 5/3. For the storage modulus $S \cdot \cos(\varphi)$ it yields:

$$\overline{G\{t\}} = 3 \cdot \int_0^1 S \cdot \cos(\varphi) \cdot x^2 dx = S_0 \cdot \cos(\varphi_0) \quad A5$$

$$S_0 \cdot \sin(\varphi_0) \cdot 3 \cdot \int_0^1 \frac{A_2^*}{B - C_1^*} \cdot \left\{ (1 - C_1^* \cdot t \cdot x^2) - (1 - B \cdot t \cdot x^2) \right\} + \frac{C_2^*}{C_1^*} \cdot \left\{ 1 - C_1^* \cdot t \cdot x^2 \right\} \cdot x^2 dx$$

Equation A5 will be equal to the first order approximation of Eq. 2 for the 4PB test if $\alpha_2^* = (3/5) \cdot A_2^*$, $\beta = (3/5) \cdot B$ and $\gamma_2^* = (3/5) \cdot C_2^*$. In reverse the coefficients A_2^* , B and C_2^* can be estimated using 4PB tests by multiplying α_2^* , β and γ_2^* with a factor 5/3.

LABORATORY INVESTIGATION ON HEALING OF SAND ASPHALT MIXTURES

Venkaiah Chowdary¹, J. Murali Krishnan², A.M.ASCE, and V. R. Rengaraju³

ABSTRACT

Asphalt is a complex civil engineering material. Asphalt when mixed with granular aggregates exhibits wide range of responses. "Healing" is one such mechanical response wherein if the material is allowed to rest after certain number of load applications, the material exhibits a "beneficial internal structure change". In this investigation, repeated triaxial tests were carried out on sand asphalt mixtures with varied confinement conditions and rest periods to quantify healing of asphalt mixtures in the laboratory. Two parameters were identified to quantify healing. The first parameter corresponds to the percentage change in instantaneous deformation before and after rest period. The second parameter corresponds to the percentage change in strain recovery at a fixed time period after unloading. The influence of various testing conditions on these two parameters is investigated.

INTRODUCTION

Asphalt concrete pavements are subjected to wide range of loading and environmental conditions. Fatigue occurring due to repeated traffic loading is one of the major distress in asphalt concrete pavements. It is well known that the laboratory fatigue tests have limited capability in predicting the fatigue life in the field. Some of the reasons due to the large difference between laboratory and field fatigue life are due to the differences in rest periods and loading. Normally, the fatigue life of

¹ Ph. D. Scholar, Department of Civil Engineering, Indian Institute of Technology Madras, Chennai-600036, India

² Assistant Professor, Department of Civil Engineering, Indian Institute of Technology Madras, Chennai-600036, India, Email: jmk@iitm.ac.in

³ Professor, Department of Civil Engineering, Indian Institute of Technology Madras, Chennai-600036, India

asphalt concrete pavements is predicted through laboratory investigations. During the rest period, relaxation of stresses due to viscoelastic nature of asphalt mixtures and healing takes place. While relaxation of stresses is a well understood phenomenon in viscoelastic material, healing for asphalt mixtures is quite complex and is yet to be unraveled in a convincing manner.

While healing for polymers is a reasonably well understood phenomena, one cannot say the same thing about healing in asphalt mixtures. Considering the fact that a typical asphalt mixture has several fractions of aggregates with complex interactions taking place at different length scales, a clear and precise understanding is found lacking. Some of the closest descriptions related to healing for asphalt mixtures are “the partial recovery of mechanical properties upon resting” (Smith and Hesp 2000) and “beneficial internal structure change” (Kim et al. 1990). It is hypothesized in the literature that the internal structure change can be due to several mechanisms such as closure of microcracks and macrocracks, coalescence of air voids, steric hardening of asphalt, etc.

Bazin and Saunier (1967) were one of the earliest to quantify the beneficial effect resulting due to rest periods introduced between successive loading cycles. Investigations were also conducted by Monismith et al. (1961), Deacon and Monismith (1967), Raithby and Sterling (1970), Bonnaure et al. (1982), Hsu and Tseng (1996), Pronk (1997), Philips (1998), Smith and Hesp (2000) on the various aspects of healing of asphalt pavements. A simplified linear constitutive model for healing is also in vogue (Kim and Little 1990; Daniel and Kim 2001; Kim et al. 2003). A complete review on fatigue of asphalt mixtures can be found in Baburamani (1999) and the implications related to considering healing in constitutive modeling in the review article by Murali Krishnan and Rajagopal (2003).

To understand the actual field behaviour of asphalt concrete pavements and to predict its service conditions to a reasonable accuracy, it is imperative that one understands the mechanism of healing that is at play during rest periods. The complexity of this phenomenon needs more detailed investigations on both the experimental and analytical front. This paper reports the experimental investigation carried out on healing of sand asphalt mixtures using a triaxial test setup with varied confinement conditions.

EXPERIMENTAL INVESTIGATIONS

Materials

Fine river sand passing through 4.75 mm Indian Standard sieve with gradation as shown in Figure 1 was mixed with 8 percent asphalt to prepare the Marshall sized samples of 100 mm diameter and 70 mm height. 60/70 grade straight run asphalt was used as the binder throughout the experiments. The relevant standard procedure as outlined in ASTM D1559-89 for preparing Marshall specimens for heavy traffic conditions was followed. The compacted specimens were cooled to room

temperature in the moulds. The physical properties of asphalt, sand and asphalt mix are shown in Table 1. Specimens of 35 mm diameter and 70 mm height as shown in Figure 2 were cored from the Marshall Samples prepared with 8 and 10 percent air voids using a coring machine. The cored samples were allowed to cure for 24 hours at room temperature before the test to ensure the relaxation of residual stresses developed during coring.

TABLE 1. Properties of Asphalt, Sand and Sand Asphalt Mix

Property (1)	Value (2)
Penetration @ 25°C, 5 sec, 100 g, 1/10 mm	67
Softening point of asphalt (°C)	41
Ductility of asphalt @ 27°C (cm)	102
Specific gravity of asphalt	1.01
Specific gravity of sand	2.56
Bulk specific gravity of sand asphalt mix at 8% air voids	2.10
Bulk specific gravity of sand asphalt mix at 10% air voids	2.06

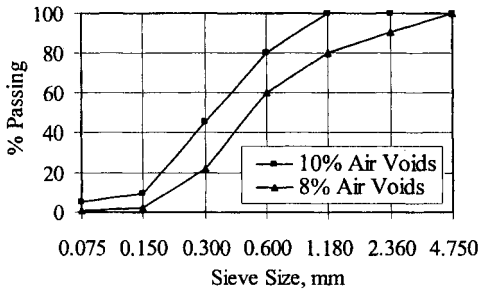


FIG. 1. Gradation of Sand Used for the Study

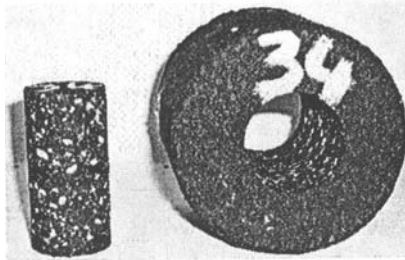


FIG. 2. Triaxial Test Specimen Cored from Marshall Sample

Testing Method

To characterize healing of asphalt mixtures in the laboratory, repeated triaxial tests were carried out on sand asphalt mixtures with varied confinement conditions. In reality, an asphalt concrete pavement is confined in all directions and the cyclic loading simulates the load application due to the vehicular movement. All the tests were conducted in load controlled mode. Two loading/unloading cycles of 7 and 14 seconds were conducted. Two sets of lateral pressure / vertical pressure ($0.5 \text{ kg/cm}^2 / 2.5 \text{ kg/cm}^2$; $0.875 \text{ kg/cm}^2 / 4.375 \text{ kg/cm}^2$) corresponding to a ratio of 1:5 were applied for each specimen. This specific ratio of lateral to vertical pressure was chosen after several laboratory trials. One of the main considerations in choosing this specific ratio is related to subjecting the specimen to load levels that will engender deformation capable of healing during the rest periods and yet not physically deform the specimen.

The cored specimen from the Marshall sample was covered with a rubber membrane to prevent entry of water during confinement. The specimen was placed inside the triaxial test cell and was made water tight. The specimen was tested at constant load with rest periods introduced between successive loading cycles to observe the deformation response. Continuous data throughout the loading and rest periods was gathered through a data acquisition system attached to a computer. The entire testing was conducted at room temperature.

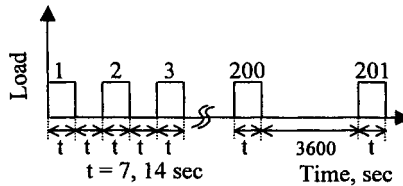


FIG. 3. Load Controlled Cyclic Loading and Rest Periods

Repeated load and rest period of same duration was applied for certain number of cycles as shown in Figure 3. The material was allowed to rest for one hour and the same loading and rest cycles of equal duration were applied again to observe the deformation response. The deformation of the material with time during loading and rest periods was measured. Two samples were tested for each condition and the repeatability was found to be less than 5 percent.

RESULTS AND DISCUSSION

Figure 4 shows the microstrain versus time data for the 8% air voids mixture for different loading and confinement conditions and Figure 5 shows the same for 10% air voids mixture. It is seen that the response of the material before and after rest periods is markedly different.

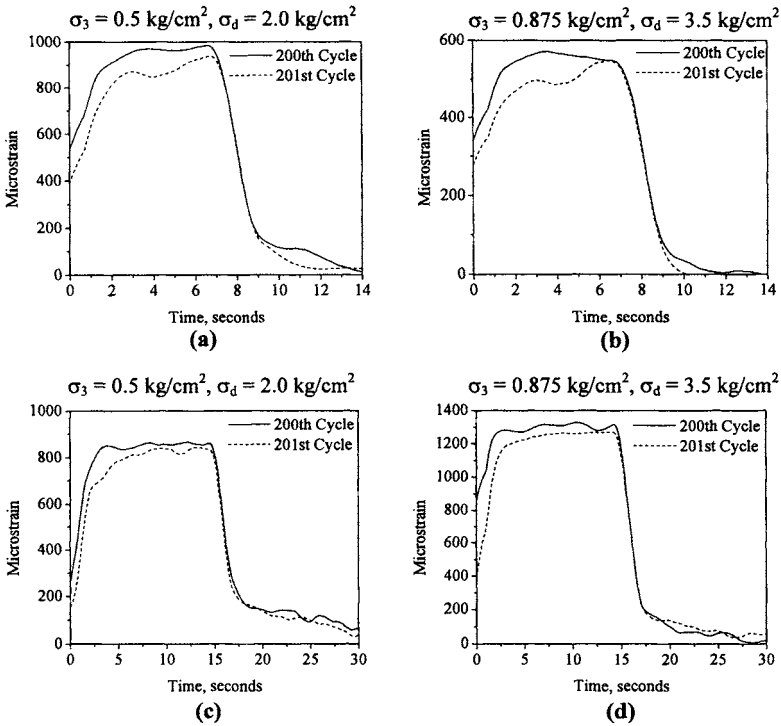


FIG. 4. (a), (b) 8% air voids, 7 seconds loading/rest period; (c), (d) 8% air voids, 14 seconds loading/rest period

Two parameters were selected for characterizing the healing of sand asphalt mixtures investigated in this study. The first parameter corresponds to the change in the instantaneous elastic deformation at time $t = 0$. For the same load application, a reduction in the instantaneous elastic deformation after rest period signifies improved material property (the material modulus value increases resulting in decreased elastic deformation). The changes in instantaneous elastic deformation for all the testing conditions plotted here are shown in Table 2. The second parameter chosen to characterize healing is related to the improved strain recovery or 'springiness' resulting due to the rest period. The percentage of strain recovered at the end of three seconds after load removal when compared with the strain at the end of the loading cycle was selected as the second parameter. The three second time limit was chosen after carefully observing the experimental plots. The results of the difference in the strain recovery are shown in Table 2. From the Table 2 and from the Figures 4 and 5, it is seen that the first parameter essentially depends on the magnitude of rest period. The more the rest period, the more beneficial change results in the material parameter related to the instantaneous elastic deformation. The second parameter

essentially characterizes how much of deformation can be recovered during strain recovery and the influence of rest period on this deformation recovery. The experimental data presented here shows that it depends on the loading and rest period cycle. While a definite trend is seen for 8% air voids asphalt mixture, it is lacking for the 10% air void asphalt mixture. It is to be reiterated here that more experimental observations in terms of several loading/rest period magnitudes can result in increased understanding of the influence of air voids on healing parameters.

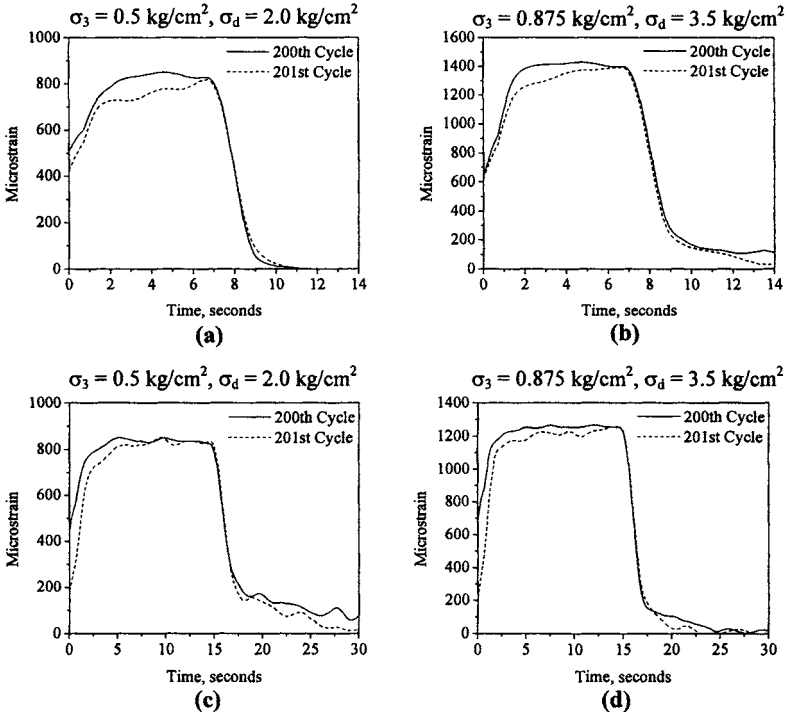


FIG. 5. (a), (b) 10% air voids, 7 seconds loading/rest period; (c), (d) 10% air voids, 14 seconds loading/rest period

It is to be emphasized here that no apriori assumed material model was used for characterizing healing. It is not uncommon to see terminologies such as “dynamic modulus” or “stiffness” etc., in characterizing the healing of asphalt mixtures. Very few experimental observations have been reported that just describes the material behavior without ascribing any specific constitutive model. For instance, for developing a proper non-linear, frame invariant constitutive model for sand asphalt that takes into account healing, experimental observation such as reported in this study will be very useful.

It is well known that healing of asphalt mixtures depends considerably on the temperature of the pavement. Hence any rigorous testing to characterize the healing of asphalt mixtures at least in the laboratory should include testing at different temperatures. However, in this investigation, the focus was on developing an understanding of healing from a macroscopic point of view in terms of clearly observable kinematic parameters. It is also possible that when tested at different temperatures or at sequences of varying temperatures, additional information about the kinematics of deformation may be obtained.

TABLE 2. Healing Parameters

Air voids in the mix (%)	Loading time/rest period (seconds)	Lateral pressure, σ_3 (kg/cm ²)	Deviatoric pressure, σ_d (kg/cm ²)	Healing Parameters		
				(I) Difference in instantaneous elastic deformation (microstrain)	(II) Percentage change in elastic recovery after 3 seconds of unloading	
					Before rest	After rest
(1)	(2)	(3)	(4)	(5)	(6)	(7)
8	7	0.5	2.0	144.89	87.89	91.01
8	7	0.875	3.5	62.57	93.61	99.41
8	14	0.5	2.0	104.56	78.18	78.70
8	14	0.875	3.5	457.20	85.67	86.23
10	7	0.5	2.0	80.39	98.34	97.02
10	7	0.875	3.5	16.89	87.88	89.33
10	14	0.5	2.0	264.90	76.52	82.16
10	14	0.875	3.5	459.49	88.69	87.71

CONCLUSIONS

In this investigation on experimental observation of healing of sand asphalt mixtures, cyclic triaxial tests were conducted with rest periods introduced at the end of every two hundred cycles. Two kinematic parameters were introduced in an attempt to characterize healing. The two parameters considerably exhibit the influence of rest periods on healing. While this is a well known observation, the fact that these are just kinematical observations gives credence to this study without recourse to the use of any specific constitutive model or material moduli.

Healing of asphalt mixtures needs to be characterized at different length scales. For instance, detailed investigations using sophisticated techniques such as computer tomography (Masad et al. 1999) have thrown light on the influence of internal structure of asphalt mixtures and their evolution. On the other hand, investigations reported here concerns characterizing healing in a macroscopic sense. Investigations are currently underway to test the influence of different lateral/axial pressure ratios on healing.

REFERENCES

- Baburamani, P. (1999). "Asphalt fatigue life prediction models – A literature review." *Res. Rep. ARR 334*, ARRB Transportation Research Ltd., Australia.
- Bazin, P., and Saunier, J.B. (1967). "Deformability, fatigue and healing properties of asphalt mixes." *Proc., 2nd Int. Conf. on the Struct. Des. of Asphalt Pavements*, Ann Arbor, Michigan, USA, 553-569.
- Bonnaure, F.P., Huibers, A.H.J.J., and Boonders, A. (1982). "A laboratory investigation of the influence of rest periods on the fatigue characteristics of bituminous mixes." *Proc., Assn. of Asphalt Paving Technologists*, 51, 104-128.
- Daniel, J.S., and Kim, Y.R. (2001). "Laboratory evaluation of fatigue damage and healing of asphalt mixtures." *J. Mat. in Civ. Engrg.*, ASCE, 13(6), 434-440.
- Deacon, J.A., and Monismith, C.L. (1967). "Laboratory flexural-fatigue testing of asphalt concrete with emphasis on compound loading tests." *Hwy. Res. Rec. 158*, Highway Research Board, 1-31.
- Hsu, T.W., and Tseng, K.H. (1996). "Effect of rest periods on fatigue response of asphalt concrete mixtures." *J. Transp. Engrg.*, ASCE, 122(4), 316-322.
- Kim, Y.R., and Little, D.N. (1990). "One-dimensional constitutive modeling of asphalt concrete." *J. Engrg. Mech.*, ASCE, 116(4), 751-772.
- Kim, Y.R., Little, D.N., and Benson, F.C. (1990). "Chemical and mechanical evaluation on healing mechanism of asphalt concrete." *Proc., Assn. of Asphalt Paving Technologists*, 59, 240-275.
- Kim, Y.R., Little, D.N., and Lytton, R.L. (2003). "Fatigue and healing characterization of asphalt mixtures." *J. Mat. in Civ. Engrg.*, ASCE, 15(1), 75-83.
- Krishnan, J.M., and Rajagopal, K.R. (2003). "Review of the uses and modeling of bitumen from ancient to modern times." *Appl. Mech. Review*, ASME, 56(2), 149-214.
- Masad, E., Muhunthan, B., Shashidhar, N., Harman, T. (1999). "Internal structure characterization of asphalt concrete using image analysis." *J. Comp. in Civ. Engrg.*, ASCE, 13(2), 88-95.
- Monismith, C.L., Secor, K.E., and Blackmer, E.W. (1961). "Asphalt mixture behaviour in repeated flexure." *Proc., Assn. of Asphalt Paving Technologists*, 30, 188-222.
- Philips, M.C. (1998). "Multi-step models for fatigue and healing, and binder properties involved in healing." *Proc., Eurobitume Workshop on Performance Related Properties for Bituminous Binders*, Luxembourg, Paper No. 115.
- Pronk, A.C. (1997). "Comparison of 2 and 4 point fatigue tests and healing in 4 point dynamic bending test based on the dissipated energy concept." *Proc., 8th Int. Conf. on Asphalt Pavements*, Seattle, Washington, USA, 987-994.
- Raithby, K.D., and Sterling, A.B. (1970). "The effect of rest periods on the fatigue performance of a hot-rolled asphalt under reversed axial loading." *Proc., Assn. of Asphalt Paving Technologists*, 39, 134-152.
- Smith, B.J., and Hesp, S.A.M. (2000). "Crack pinning in asphalt mastic and concrete: effect of rest periods and polymer modifiers on the fatigue life." *Proc., 2nd Eurasphalt and Eurobitume Congress*, Barcelona, Spain, Book II, 539-546.

FATIGUE CHARACTERIZATION OF HMAC MIXTURES USING MECHANISTIC EMPIRICAL AND CALIBRATED MECHANISTIC APPROACHES INCLUDING THE EFFECTS OF AGING

Lubinda F. Walubita¹, Student Member, ASCE, Amy Epps Martin², Member, ASCE, Charles Glover³, Sung Hoon Jung⁴, Gregory Cleveland⁵, and Robert L. Lytton⁶, Fellow, ASCE

ABSTRACT: Laboratory fatigue characterization of HMAC mixtures constitutes a fundamental component of pavement design and analysis to ensure adequate performance. In this study, the traditional mechanistic empirical (ME) approach and a continuum micromechanics based calibrated mechanistic approach with surface energy (CMSE) measurements were comparatively utilized to characterize the fatigue resistance of two HMAC mixtures in the laboratory, including investigating the effects of aging. Although the results were comparable, the CMSE approach exhibited greater flexibility and potential to discretely account for most of the fundamental material properties (including fracture, aging, healing, visco-elasticity, anisotropy, crack initiation, and crack propagation) that affect HMAC pavement fatigue performance. Compared to the mechanistic-empirically based ME approach, the CMSE approach is based on the fundamental concepts of continuum micromechanics and energy theory; and utilizes the visco-elastic correspondence principle, Paris' Law of fracture mechanics, and Schapery's work potential theory to monitor cumulative fracture damage in HMAC mixtures, measured in terms of dissipated pseudo strain energy (DPSE) under repeated uniaxial tensile tests. Additionally, the CMSE results exhibited relatively lower statistical variability. For the materials and test conditions considered in the study, aging reduced HMAC mixture fatigue resistance and its ability to heal. Thus aging plays a significant role in HMAC mixture fatigue performance and should be incorporated in fatigue design and analysis.

¹ Research Assistant, Texas Transportation Institute, 501G CE/TTI Building, 3136 TAMU, College Station, TX 77843-3136, Email: lfwalubita@hotmail.com

² E.B. Snead II Associate Professor, Texas A&M University, 503F CE/TTI Building, 3136 TAMU, College Station, TX 77843-3136, Email: a-eppsmartin@tamu.edu

³ Professor, Texas A&M University, Dept of Chemical Engineering, 3122 TAMU, College Station, TX 77843-3122, Email: c-glover@tamu.edu

⁴ Research Assistant, Texas A&M University, Dept of Chemical Engineering, 3122 TAMU, College Station, TX 77843-3122, Email: sung.jung@chemail.tamu.edu

⁵ Technical Operations Manager, Texas Department of Transportation, 125 East 11th Street, Austin, TX 78701-2483, Email: gclevla@dot.state.tx.us

⁶ Benson Chair Professor, Texas A&M University, 503A CE/TTI Building, 3136 TAMU, College Station, TX 77843-3136, Email: r-lytton@civil.tamu.edu

INTRODUCTION

Hot-mix asphalt concrete (HMAC) is a heterogeneous complex composite material of air, binder, and aggregates used in pavement construction. Approximately 500 million tons of HMAC (valued at about \$11.5 billion) is used in pavement construction yearly in the USA (Si 2001). Despite this widespread usage, the fatigue characterization of HMAC mixtures to ensure adequate performance is not very well established, and fundamental fatigue predictive models still remain to be developed.

Under traffic loading and changing environmental conditions, HMAC exhibits nonlinear elasto-viscoplastic and anisotropic behavior. Its mechanical properties and performance are loading rate, temperature, and directionally dependent (Lytton et al. 1993). With time, HMAC also ages but has the potential to heal (closure of fracture surfaces) during traffic loading rest periods. Inevitably, this complex nature of HMAC response behavior under changing traffic loading and environmental conditions makes it harder to adequately model HMAC mixture properties, particularly with respect to fatigue cracking. Complicating mixture resistance to fatigue are the effects of binder oxidative aging (as a function of time) that increase both the binder viscosity and elastic moduli, thus reducing its ductility and increasing the HMAC mixture's susceptibility to fatigue cracking (Glover et al. 2003).

Comprehensive HMAC mixture fatigue analysis approaches that take into account the complex nature of HMAC are thus needed to ensure adequate field fatigue performance. Analysis models associated with such approaches should have the potential to utilize fundamental HMAC mixture properties that are critical to HMAC pavement fatigue performance when predicting mixture fatigue resistance and pavement fatigue life. Various fatigue analysis approaches have been developed and some are in use today, but many are inadequate in producing fatigue resistant HMAC mixtures or pavement structures that are structurally adequate in fatigue throughout the pavement's design life.

In this study, the traditional mechanistic empirical (ME) fatigue analysis approach and a continuum micromechanics based calibrated mechanistic fatigue analysis approach with surface energy (CMSE) measurements were utilized to comparatively evaluate the fatigue resistance of two HMAC mixtures. The second objective of the study was to investigate the effects of binder oxidative aging on HMAC mixture properties and fatigue resistance. In the paper, the experimental design program including the two HMAC mixtures, aging exposure conditions, and field conditions are discussed followed by a brief description of the two fatigue analysis approaches (ME and CMSE) and their associated laboratory tests. Results are then presented and analyzed, followed by a discussion and summary of the findings.

EXPERIMENTAL DESIGN

Two commonly used TxDOT HMAC mixtures termed Basic and Rut Resistant and defined as Bryan and Yoakum mixtures, respectively, were utilized. The Bryan mixture was a dense graded TxDOT Type C mixture designed with PG 64-22 binder and limestone aggregate (TxDOT 2003). The Yoakum mixture was a 12.5 mm Superpave mixture designed with a PG 76-22 binder (modified with 5% SBS polymer modifier) and crushed river gravel aggregate. Additionally, the Yoakum mixture used 14% limestone screenings and 1% hydrated lime.

The optimum design binder contents were 4.6% and 5.6% for the Bryan and Yoakum mixtures, respectively, by weight of aggregate. The target specimen fabrication air void (AV) content for both mixtures was $7\pm 0.5\%$ to simulate in situ field AV after construction and trafficking when fatigue resistance is critical. The standard Superpave Gyrotory Compactor (SGC) and the linear kneading beam compactors were used for compacting cylindrical and beam HMAC specimens for CMSE and ME testing, respectively (AASHTO 1994; AASHTO 1996; and TxDOT 2003).

Three aging exposure conditions (0, 3, and 6 months) at 60 °C that simulate approximately up to 12 years of Texas field HMAC aging at the critical pavement service temperature were selected to investigate the effects of aging on HMAC mixture fatigue properties and N_f (Glover et al. 2003). The oxidative aging process involved keeping the compacted specimens in an environmentally temperature-controlled room at 60 °C and allowing the heated air to circulate freely around the specimens. This allowed for accelerated oxidative aging of the binder within the HMAC specimens. Note that all loose HMAC mixtures were subjected to the standard AASHTO PP2 4 hr short-oven aging process at 135 °C prior to 60 °C aging (AASHTO 1994). After HMAC mixture testing, aged binders were extracted for testing to characterize the binder chemical and physical properties (Walubita et al. 2005). For each test type, at least two replicate HMAC specimens were tested per aging condition per mixture type. Because HMAC fatigue cracking is generally more prevalent at intermediate pavement service temperatures, most of the laboratory tests were conducted at 20 °C. Otherwise, the data were normalized to 20 °C during the analysis phase.

For hypothetical field conditions, a standard TxDOT pavement structure consisting of 150 mm HMAC (3,447 MPa, $\nu = 0.33$), 350 mm flex (granular) base (194 MPa, $\nu = 0.40$), and a subgrade with an elastic modulus of 63 MPa ($\nu = 0.45$) was utilized. Typical traffic conditions consisted of an 80 kN axle load, 690 kPa tire pressure, and 5 million equivalent single axle loads (ESALs) with about 25% trucks over a design life of 20 years and a 95% reliability level in a Wet-Warm (WW) Texas environment considered critical to HMAC pavement fatigue performance. Tensile (ϵ_i) and shear (γ) strains which constitute the input failure load-response parameters for the ME and CMSE fatigue analysis approaches were computed using an elastic multi-layered ELSYM5 software, but were adjusted based on Finite Element (FEM) simulations to account for more realistic HMAC behavior in terms of visco-elasticity and plasticity (Walubita et al. 2005).

THE MECHANISTIC EMPIRICAL (ME) APPROACH

The ME approach utilized in this study is that developed during the SHRP A-003A research project and described in the AASHTO TP8-94 test protocol (Tayebali et al. 1992 and AASHTO 1996). The laboratory testing (strain-controlled flexural bending beam fatigue tests at 20 °C), failure criteria (50% flexural stiffness reduction), and analysis procedure including the required analysis input data were conducted consistent with this protocol (AASHTO 1996 and Walubita et al. 2005). Eq. 1 shows the ME fatigue analysis model utilized for predicting HMAC mixture fatigue life in this study (Tayebali et al. 1992 and AASHTO 1996).

$$N_f = \frac{SF [k_1 (\epsilon_i)^{-k_2}]}{TCF} \geq M \times \text{Traffic Design}_{ESALS} \dots\dots\dots(1)$$

In Eq. 1, N_f is the HMAC mixture field fatigue life; SF is a composite field shift factor that accounts for traffic wander, construction variability, loading frequency, healing, and crack propagation through the HMAC layer; k_i are laboratory determined material constants; ϵ_i is the critical design tensile strain computed at the bottom of the HMAC layer; TCF is the temperature correction factor that accounts for the temperature differences between laboratory testing conditions and the environment; and M is a reliability multiplier that accounts for mixture variability and the anticipated uncertainties in the mixture fatigue performance during service. In this study, values of $SF = 19$, $M = 3.57$, and $TCF = 1.0$ were used (Tayebali et al. 1992).

THE CALIBRATED MECHANISTIC APPROACH WITH SURFACE ENERGY (CMSE) MEASUREMNTS

The CMSE is a continuum micromechanics approach based upon the fundamental theory that HMAC is a complex composite material that behaves in a nonlinear elasto-viscoplastic manner, exhibits anisotropic behavior, ages, heals, and requires that energy be expended to cause load-induced damage in the form of cracking. Equally, energy must be expended to close up these fracture surfaces, a process called healing. The approach utilizes the visco-elastic correspondence principle, Paris’s Law of fracture mechanics, and the work potential theory described by Schapery (1984) to remove viscous effects and monitoring of accumulated fracture damage through changes in dissipated pseudo strain energy (DPSE) under repeated uniaxial tensile tests (Lytton et al. 1993 and Si 2001). The CMSE approach considers that HMAC micro-fatigue damage consists of two components; resistance to fracture under repeated loading and the ability to heal during loading rest periods, processes that both change over time. The approach further considers that resistance to fracture is governed by two processes; namely the number of repetitive load cycles for microcracks to coalesce to macrocrack initiation (N_i) and the number of repetitive load cycles for macrocrack propagation through the HMAC layer (N_p) that add to N_f . The HMAC is thus characterized in terms of fracture (ΔG_f) and healing (ΔG_h) processes, and requires only uniaxial relaxation tests (tension and compression), strength, repeated load tests in uniaxial tension (RDT), and fracture and healing surface energy components of binders and aggregates measured separately (Walubita et al. 2005).

CMSE Fatigue Analysis Models and Failure Criteria

Eq. 2 is the fundamental principle of CMSE fatigue modeling of HMAC mixtures utilized in this study.

$$N_f = SF_i [N_i + N_p] \geq Q \times \text{Traffic Design}_{ESALS} \dots\dots\dots(2)$$

$$SF_i = SF_a \times SF_h \times SF_{ag} \dots\dots\dots(3)$$

$$N_p = k_1 (\gamma)^{-k_2} \dots\dots\dots(4)$$

The CMSE approach considers the fact that HMAC is not an isotropic material and introduces an anisotropic shift factor SF_a to account for the differences in the vertical and lateral elastic modulus that result due to the differences in the particle orientation during compaction/construction. Due to traffic rest periods and temperature variations, the binder has a tendency to heal, which often results in improvement in the HMAC mixture fatigue performance. A SF_h shift factor is thus introduced in the analysis to account for this healing process. This SF_h is a function of the loading rest periods, pavement design life, field temperature correction factor, HMAC elastic relaxation modulus in compression, surface energy due to healing (ΔG_h), and fatigue field calibration constants. The CMSE approach considers that aging, principally due to binder oxidation over time, is a very significant factor contributing to the fatigue deterioration of HMAC pavements and introduces an aging shift factor (SF_{ag}) to account for the binder aging effects in N_f predictions. In this paper, an SF_{ag} was determined as a function of the binder shear properties and aging period (time).

N_i defined as the number of load cycles required to initiate and grow a microcrack of 7.5 mm in length in the HMAC layer, is a function of crack density, specimen cross-sectional area, Paris' Law fracture coefficients (A and n), and the rate of damage accumulation (b) as indicated by DPSE in the uniaxial repeated-direct tension test. N_p refers to the number of load cycles required to propagate a 7.5 mm microcrack through the HMAC layer thickness. This N_p is calculated as a function of the maximum microcrack length, HMAC layer thickness, shear modulus, Paris' Law fracture coefficients (A and n), and a design shear strain (γ) (Lytton et al. 1993 and Si 2001). Other CMSE input parameters include non-linearity correction factor (ψ), material coefficients, regression and shear coefficient factors, HMAC brittle-ductile failure characterization, healing constants, and field calibration constants.

Q is a reliability factor that accounts for mixture and traffic prediction variability and the anticipated uncertainties in the mixture fatigue performance during service. A Q value of 1.0 was used in this study. However, further CMSE research should inevitably explore the derivation of Q as a function of reliability level so as to adequately account for HMAC mixture and traffic prediction variability in N_f analysis.

Fatigue failure for the CMSE approach was defined as crack initiation and propagation through the HMAC layer thickness of a 7.5 mm microcrack length. This threshold value was selected based on the previous work by Lytton et al. (1993).

TYPICAL RESULTS AND ANALYSIS

HMAC mixture results at a reference temperature of 20 °C and 95% reliability level, including the effects of 0, 3, and 6 months aging at 60 °C are presented in this section (Walubita et al. 2005).

HMAC Mixture Fatigue Lives

Considering that 0, 3, and 6 months aging at 60 °C is an equivalency of up to 12 years of HMAC pavement service life in Texas (Glover et al. 2003), Fig. 1 shows that both ME and CMSE N_f predictions are comparable. Both approaches indicate a considerable N_f decay with aging and that the Yoakum mixture exhibited better fatigue resistance in terms of N_f magnitude.

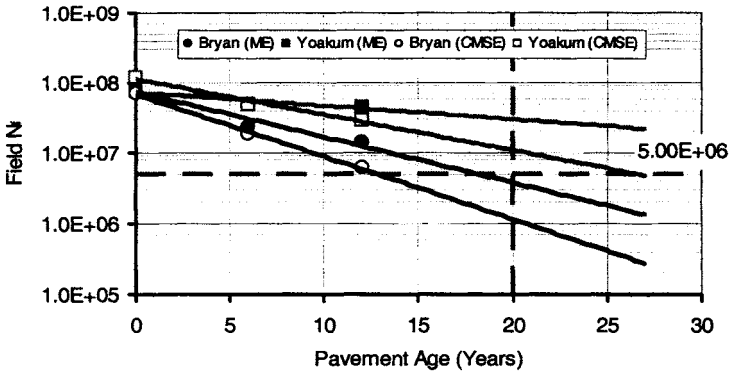


FIG. 1. HMAC Mixture Field N_f @ 20 °C

Assuming that N_f exhibits an exponential functional relationship with pavement age as fitted in Fig. 1 and if the ME N_f extrapolations at year 20 (Fig. 1) are divided by an M value of 3.57 consistent with Eq. 1, both the ME (1.03×10^6 and 8.30×10^6 for Bryan and Yoakum mixtures, respectively) and CMSE (1.21×10^6 and 9.96×10^6 for Bryan and Yoakum mixtures, respectively) N_f predictions are comparable. Thus both fatigue analysis approaches indicate inadequate and adequate theoretical fatigue performance for the Bryan and Yoakum mixtures, respectively, based on the 5×10^6 design traffic ESALs and 20 years service life at 95% reliability level.

While the N_f predictions were comparable, variability in terms of COV of $Ln N_f$ ranged between 6.87% to 9.85% for the ME approach and 2.81% to 3.98% for the CMSE approach. Among other factors, this high ME variability based on logarithmic response was tied to the AV variability with COV ranges of 2.81% to 5.94% and 4.04% to 7.87% for 10 random cylindrical and beam specimens, respectively. Compared to the more compact and easy to handle SGC compacted cylindrical specimens, it was generally more difficult to control the beam specimen AV during compaction due to the nature of their shape and the kneading compaction method.

Incorporating the Effects of Binder Oxidative Aging in CMSE N_f Predictions

Eq. 5 shows a simplified model of the aging shift factor (SF_{ag}) derived as a function of the measured binder shear properties (unaged and aged) and aging period.

$$SF_{ag} = u\chi_m^w \dots\dots\dots(5)$$

In Eq. 5, u and w are material regression constants; χ_m is the material property ratio that relates the aged and unaged binder shear properties; and t is the pavement age in years.

Using Eq. 5, SF_{ag} values were determined as plotted in Fig. 2 and subsequently used to predict N_f based on the measured 0 months N_f using Eq. 6.

$$N_f = SF_{ag(i)} \times N_{f(0months)} \dots\dots\dots(6)$$

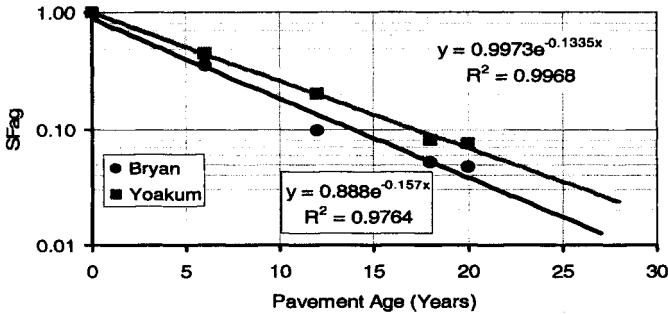


FIG. 2. Plot of CMSE SF_{ag} versus Pavement Age

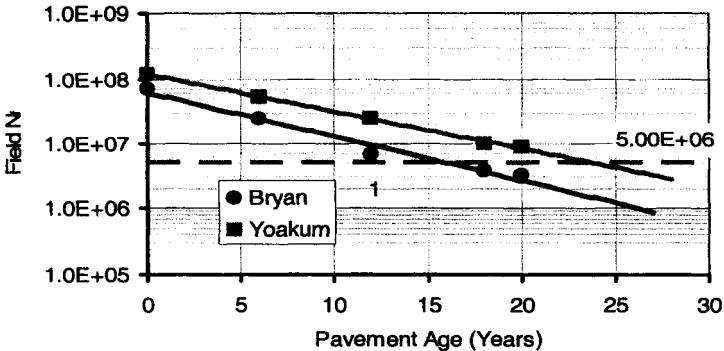


FIG. 3. CMSE Field N_f Predictions based on SF_{ag} Analysis

Fig. 3 shows the predicted N_f results as a function of pavement age and in fact do not differ significantly from the AASHTO 2002 Pavement Design Guide (MEPDG) software (AASHTO 2004) predictions based on a similar pavement structure, environmental conditions, and a 20 year design life at 95% reliability level. For example, the predicted N_f in the 20th year of service life according to this CMSE- SF_{ag} approach are approximately 3.24×10^6 and 8.67×10^6 for Bryan and Yoakum mixtures, respectively; compared to the 4.71×10^6 and 6.21×10^6 MEPDG software (AASHTO 2004) predictions for Bryan and Yoakum mixtures, respectively (Walubita et al. 2005).

Considering that this SF_{ag} methodology was based on a simple generalized binder oxidative aging concept with measured binder shear properties and aging conditions as the primary variables, these preliminary results are plausible. The result offers a motivation for further investigation of binder oxidative aging effects and development of representative aging shift factors based on binder properties after accelerated laboratory aging.

HMAC Mixture Properties and Effects of Binder Oxidative Aging

The mixture tensile test conducted at 20 °C indicated that as the HMAC ages; it becomes more brittle, thus breaking under tensile loading at a lower strain level. For both mixtures, while the σ_t was within the test variability, the ϵ_f at break decreased significantly by over 50% after 6 months aging due to an increase in mixture brittleness from binder oxidative aging (i.e., from 1,245 to 401 microstrain for the Bryan mixture and from 3,483 to 851 microstrain for the Yoakum mixture). In terms of mixture comparison, the Yoakum mixture exhibited more ductility and better resistance to tensile stress than the Bryan mixture based on higher σ_t and ϵ_f values (Walubita et al. 2005).

Based on simple energy theory concepts, the higher the ΔG_f value, the greater the resistance to fracture damage and the lower the ΔG_h value, the greater the potential to self heal. With these relationships, the SE test results at 20 °C indicated that the Yoakum mixture had a better adhesive bond strength to resist fracture damage and a stronger potential to self heal compared to the Bryan mixture at all aging conditions. In terms of response to aging, ΔG_f generally exhibited a decreasing trend and vice versa for ΔG_h . Thus binder oxidative aging reduces HMAC mixture resistance to fracture damage and its ability to self heal (Walubita et al. 2005).

Analysis of the DPSE results based on RDT testing at 30 °C with the test data normalized to 20 °C indicated that the rate of fracture damage accumulation for both mixtures increased with aging and that the Bryan mixture was more susceptible to fracture damage than the Yoakum mixture (Walubita et al. 2005).

DISCUSSION OF RESULTS AND COMPARISON OF APPROACHES

Although the ME approach exhibited relatively higher variability, the ME and CMSE N_f predictions were comparable and both indicated an exponentially declining N_f trend with aging and that the rate of N_f decay is mixture dependent. The utilization of the CMSE SF_{ag} analysis further provided confidence in the extrapolated N_f results and highlighted the significance of incorporating binder oxidative aging effects in N_f predictions. The further development of a comprehensive CMSE SF_{ag} particularly as a function of time with more research will inevitably allow for realistic N_f prediction at any desired pavement age.

In terms of HMAC mixture comparison, the Yoakum mixture exhibited better fatigue resistance in terms of N_f magnitude and less sensitivity to binder oxidative aging. This was attributed to the relatively higher SBS polymer modified binder content (5.6% versus 4.6% for Bryan by aggregate weight) and the 1% hydrated lime content in the Yoakum mixture. Although lime is often added to improve mixture resistance to moisture damage, this lime perhaps increased the mixture's resistance to both fatigue and aging.

Additionally, the Yoakum mixture indicated better fracture and healing potential properties in terms of ΔG_f and ΔG_h , better ductility properties in terms of ϵ_f values, and greater resistance to fracture damage indicated by lower b values during RDT testing. By contrast, the Bryan mixture was more susceptible to binder oxidative aging, more brittle with aging, less resistance to fracture damage, and less able to self heal; and consequently it performed poorly in terms of N_f magnitude. Overall, this result suggests that in performance comparison studies of this nature, the whole host of HMAC mixture design characteristics and material properties need to be evaluated. For the ME-CMSE comparison, significant details are summarized in Table 1.

TABLE 1. ME versus CMSE Approach

Parameter	ME Approach	CMSE Approach	Comment
Concepts	Mechanistic-empirically based	Utilizes continuum micromechanics & fundamental HMAC properties	
Input data	Comparatively few	Comprehensive	^a
Laboratory testing	Lengthy	Numerous but relatively easy to run	
Testing time	≅ 30 hrs	≅ 70 hrs (SE is still under development)	Time may vary depending on equipment type & test parameters
Equipment cost	\$155,000 (\$25,560 for BB device)	\$210,000 (\$80,000 for SE devices)	Based on July 2004 estimates
Failure criteria	50% stiffness reduction	7.5 mm microcrack growth & propagation through HMAC layer	
Failure load-response parameter	Tensile strain (ϵ_f)	Shear strain (γ)	
Analysis procedure	Relatively easy & straightforward	Comprehensive & lengthy	CMSE utilizes numerous equations
Aging effects	None (but can use Miner's hypothesis)	Shift factor (SF_{ag}) being developed	
Variability (COV of $Ln N_f$)	Comparatively high	Relatively low	
^a Comprehensive CMSE input data are necessary to account for relevant factors that affect fatigue performance			

The principal difference stems from the fact that the ME approach is mechanistic-empirically based while the CMSE approach was formulated on the fundamental concepts of continuum micromechanics and energy theory with fracture and healing as the two primary mechanisms controlling HMAC mixture fatigue damage and utilizes the fundamental HMAC mixture properties to estimate N_f . The ME field N_f prediction is significantly dependent on the selected composite SF value and the ε_f while for the CMSE approach, all parameters are virtually determined from actual measured material properties and are discretely accounted for in the analysis. In terms of laboratory testing, the BB test is quite lengthy and the BB equipment is limited to only HMAC beam testing in a flexural tensile mode. With the exception of the SE test protocols which are still under development, the CMSE tests although numerous so as to sufficiently model all relevant mixture properties; are relatively simple to run and less time consuming. Additionally, the ME 50% stiffness reduction failure criterion's correlation to actual fatigue damage accumulation, crack area, severity, and/or crack length through the HMAC layer thickness in an in situ pavement structure is not very well defined. For the CMSE approach, the adequacy of assuming the growth of one microcrack (~ 7.5 mm) through the HMAC layer thickness as representative of the fatigue cracking process in the entire HMAC pavement structure still needs to be reviewed.

SUMMARY OF FINDINGS

For the materials and test conditions considered in this study, the following findings were derived:

- The HMAC mixture N_f predictions by both the ME and CMSE approaches were comparable although the ME approach exhibited greater variability in terms of COV of $\ln N_f$. In terms of the effects of binder oxidative aging, both the ME and CMSE approaches indicated an exponentially declining N_f trend with aging and that the rate of N_f decay is mixture dependent.
- While the ME approach is mechanistic-empirically based, the continuum micromechanics based CMSE approach exhibited greater flexibility and potential to discretely account for most of the relevant fundamental material properties (including fracture, aging, healing, visco-elasticity, anisotropy, crack initiation, and crack propagation) that affect HMAC pavement fatigue performance.
- The Yoakum (Rut Resistant) mixture exhibited better fracture and healing potential properties measured in terms of the tensile strength, surface energy, and dissipated pseudo strain energy. Consequently, this mixture exhibited less sensitivity to aging and had better fatigue resistance measured in terms of N_f magnitude possibly due to the higher SBS modified binder content and the 1% hydrated lime content compared to the Bryan (Basic) mixture. Thus for mixture performance comparison studies, the entire HMAC mixture design matrix and material properties for each HMAC mixture need to be evaluated.
- Binder oxidative aging reduces HMAC mixture fatigue resistance and potential to self heal. This finding signifies the importance of incorporating aging effects in N_f predictions, and the CMSE SF_{ag} concept utilized in this paper produced promising results. However, more research is recommended to better quantify the N_f -aging relationship and develop more representative SF_{ag} factors.

- Overall, this study has demonstrated the applicability of the CMSE approach for fatigue characterization of HMAC mixtures. Nonetheless, more research and HMAC mixture fatigue characterization is strongly recommended to further validate the CMSE approach.

Although two fatigue analysis approaches were presented in this paper, it should be noted that any fatigue design approach can produce desired results provided it is well calibrated to the environmental and traffic loading conditions of interest and that all relevant factors affecting fatigue performance, including material characterization, are appropriately taken into consideration.

ACKNOWLEDGEMENTS

This study was conducted as part of a TxDOT research project to comparatively evaluate and recommend an appropriate fatigue design and analysis approach. The authors thank TxDOT and the FHWA for their support in funding this research study and all TTI and TEES personnel for their help during the course of this research work. Special thanks are also due to Edward A. Ofori for his editorial comments.

REFERENCES

- AASHTO TP8-94 (1996). Standard Test Method for Determining the Fatigue Life of Compacted Hot-Mix Asphalt (HMA) Subjected to Repeated Flexural Bending. AASHTO Designation: PP2 (1994). Standard Practice for Short and Long Term Aging of Hot Mix Asphalt, *AASHTO Provisional Standards*, Washington, D.C.
- AASHTO, (2004). *Pocket Facts*. AASHTO 2002 Pavement Design Guide. <http://www.2002designguide.com/> Accessed November 2004.
- Glover, C.J., Davison, R.R., Domke, C.H., Ruan, Y., Juristyarini, P., Knorr, D.B., and Jung, H.S. (2003). Development of a New Method for Assessing Asphalt Binder Durability with Field Validation. Technical Research Report FHWA/TX-03/1872-2.
- Lytton, R. L., J. Uzan, E. G. Fernando, R. Roque, D. Hiltunen, and S. Stoffels. (1993). *Development and Validation of Performance Prediction Models and Specifications for Asphalt Binders and Paving Mixes*, SHRP-A-357, Washington, D.C.: Strategic Highway Research Program, NRC.
- Schapery, R. A. (1984). "Correspondence Principles and a Generalized J-Integral for Large Deformation and Fracture Analysis of Viscoelastic Media." *Int. J. Fracture*, 25, 195-223.
- Si, Z. (2001). "Characterization of Microdamage and Healing of Asphalt Concrete Mixtures." Ph.D. Dissertation, Texas A&M University, College Station, TX.
- Tayebali, A.A., Deacon, J.A., Coplantz, J.S., Harvey, J.T., and Monismith, C.L. (1992). Fatigue Response of Asphalt Aggregate Mixes. SHRP A-003.
- TxDOT. (2003). *Pocket Facts*. TxDOT Test Specification Manuals. (<http://manuals.dot.state.tx.us>) Accessed May, 2003.
- Walubita, L.F., Epps Martin, A., Jun, H.S., Glover, C.J., Park, E.S., Chowdhury, A., and Lytton, R.L. (2005). Comparison of Fatigue Analysis Approaches for Two Hot Mix Asphalt Concrete (HMAC) Mixtures. Draft TxDOT Technical Research Report FHWA/TX-05/0-4468-2.

NOTATIONS AND SYMBOLS

b	=	Rate of fracture damage accumulation under RDT testing
COV	=	Coefficient of Variation
CMSE	=	Calibrated Mechanistic with Surface Energy measurements
FHWA	=	Federal Highway Administration
k_i	=	Laboratory determined material constants
M	=	ME reliability multiplier dependent on the reliability level (e.g., 95%, 90%) that accounts for mixture variability and the anticipated uncertainties in the mixture performance during service
ME	=	Mechanistic Empirical
N	=	Laboratory load cycles
N_f	=	HMAC mixture field fatigue life expressed in terms of the number of 80 kN traffic ESALs to failure
N_i	=	Number of load cycles to crack initiation
N_p	=	Number of load cycles to crack propagation
Q	=	CMSE reliability factor
RDT	=	Uniaxial Repeated Direct Tension (RDT) test
R^2	=	Coefficient of Correlation
SBS	=	Styrene-Butadiene-Styrene
SF	=	ME composite field shift factor that accounts for traffic wander, construction variability, loading frequency, healing, and crack propagation through the HMAC layer.
SF_a	=	CMSE shift factor due to anisotropy, ranging between 1 and 5
SF_{ag}	=	CMSE shift factor due to aging, ranging between 0 and 1
SF_h	=	CMSE shift factor due to binder healing, ranging between 1 and 10
STOA	=	Short-term oven aging
TCF	=	ME temperature correction factor that accounts for the temperature differences between laboratory testing conditions and the environment
TxDOT	=	Texas Department of Transportation
TEES	=	Texas Engineering Experiment Station
TTI	=	Texas Transportation Institute
u, w	=	Material regression constants that relate to binder properties
ϵ_i	=	Critical design tensile strain computed at the bottom of the HMAC layer in a representative pavement structure and environmental conditions (mm/mm)
γ	=	Critical design shear strain computed at the edge of a loaded tire in a representative pavement structure and environmental conditions (mm/mm)
ν	=	Poisson's ratio
χ_m	=	Material property ratio that relates the binder $G^*(\omega)$ of the aged to the unaged binder (i.e., $\chi_m = m^*_{(Binder(i)/m^*_{(Binder(0))})}$)
$G^*(\omega)$	=	Binder complex shear modulus in angular frequency domain (MPa)
m^*	=	Slope of the binder $G^*(\omega)$ master-curve
ΔG_f	=	HMAC mixture surface energy due to fracture (ergs/cm ²)
ΔG_h	=	HMAC mixture surface energy due to healing (ergs/cm ²)

A CASE STUDY: ASSESSING THE SENSITIVITY OF THE COEFFICIENT OF THERMAL CONTRACTION OF AC MIXTURES ON THERMAL CRACK PREDICTION

Hao. Yin¹, Ghassan R. Chehab², and Shelley M. Stoffels³

ABSTRACT: Thermal cracking results in both structural and functional problems in asphalt concrete (AC) pavements. A critical parameter affecting the buildup of thermal stresses that ultimately lead to cracking in AC pavements is the coefficient of thermal contraction (CTC) of the AC mixture. The objective of this study is to assess the sensitivity of CTC of AC mixture on thermal cracking. Values of CTC of AC mixtures were identified through literature review, while other relevant data needed for thermal cracking prediction were obtained for three AC mixtures from the new Mechanistic-Empirical Pavement Design Guide (MEPDG) documentation. Finally, the amount of thermal cracking, in terms of length and percent damage, was predicted using the new (MEPDG) software. Results showed that the sensitivity of CTC of AC mixtures on thermal cracking is highly material dependent. The greatest sensitivity was observed with medium strength and ductile AC mixture.

INTRODUCTION

Thermal cracking of asphalt concrete (AC) pavements is a serious problem in northern regions of the United States, as well as in Alaska, Canada, and other

¹ Graduate Research Assistant, The Pennsylvania State University, Dept. of Civil and Environmental Engineering, University Park, PA 16802, hxy153@psu.edu

² Assistant Professor, The Pennsylvania State University, Dept. of Civil and Environmental Engineering, University Park, PA 16802, gchehab@engr.psu.edu

³ Associate Professor, The Pennsylvania State University, Dept. of Civil and Environmental Engineering, University Park, PA 16802, sms26@engr.psu.edu

countries at extreme northern and southern latitudes where low temperatures can fall below $-23\text{ }^{\circ}\text{C}$ (Huang 1993). Thermal cracking typically runs transversely across pavements, typically starting at a spacing of 30 m or more for new pavements down to 3-6 m for older ones (Vinson et al. 1989).

Transverse cracks in pavements are a problem because they act as conduits for the migration of water and fines into and out of the pavement, which, depending on the drainage conditions in the pavement structure, can cause a saturated condition in the underlying layers. If this happens, heavy wheel loads applied on the saturated pavement will cause excessive pore water pressure in the underlying layers, thus reducing the effective bearing capacity of the unbound base and the upper subgrade layers. Transient wheel loads can also cause pumping of fines through transverse cracks, which can produce voids under the pavement. All of these effects result in poor ride quality and reduction in pavement life. Thermal cracking is caused by adverse environmental conditions rather than by applied traffic loads, particularly due to extreme temperature drops that induce thermal tensile stresses in the AC layers.

To improve the design and performance of highways in the United States, the National Cooperative Highway Research Program (NCHRP) initiated project 1-37A to develop a new pavement design guide for new and rehabilitated pavements based on a mechanistic-empirical (M-E) approach. The resulting Mechanistic-Empirical AASHTO Pavement Design Guide (MEPDG) is accompanied with Design Guide (MEPDG) software that enables the design of both new and rehabilitated sections of flexible and rigid pavements. The thermal cracking model (TCMODEL) incorporated in the MEPDG software predicts thermal cracking performance using AC mixture properties measured from the Indirect Tensile Test (IDT), along with site-specific environmental and pavement structural information. Three AC mixture property parameters are required by the MEPDG software to predict thermal cracking: average tensile strength at $14\text{ }^{\circ}\text{F}$; creep compliance $(D(t))$, at $-4\text{ }^{\circ}\text{F}$, $14\text{ }^{\circ}\text{F}$, and $32\text{ }^{\circ}\text{F}$; and the CTC of AC mixtures. A user can either input the value of CTC directly or accept a default value computed by the software based on user defined values of percent volume of voids in the mineral aggregate (VMA) and the CTC of aggregates. The MEPDG software offers a good opportunity to assess the sensitivity of CTC of AC mixture on thermal cracking and provides a better understanding of the functionality of the TCMODEL. The results of this study will aid state highway agencies in selecting the appropriate inputs and levels of accuracy for the TCMODEL to design better and durable AC pavements.

THERMAL CRACKING MECHANISM

The mechanism of thermal cracking initiation and propagation is well documented in previous research (Roque et al. 1993; Chehab and Kim 2004). At very low temperatures, AC exhibits predominantly linear viscoelastic behavior and brittle failure modes. As the AC pavement cools, the surface layers will have a tendency to contract. However, because the pavement is restrained, no deformation can occur; consequently, thermal stresses are induced, typically in the longitudinal direction where the restraint is the greatest. For very severe cooling cycles (very low temperatures and/or very fast cooling rates), when tensile stresses built up within the

AC layer exceeds the tensile strength of the AC mixture, cracks develop at the surface and edges of the AC layer and penetrate the depth and width of the AC layer. Depending upon the magnitude of tensile stresses and the AC resistance to fracture (crack propagation), transverse cracks may develop at various locations along the length of the pavement as subsequent cooling cycles ensue.

THE COEFFICIENT OF THERMAL CONTRACTION

Most engineering materials experience a change in volume due to a change in temperature. This change is often described in terms of the coefficient of thermal expansion (α) as defined below:

$$\alpha = \frac{(\varepsilon_{T_2} - \varepsilon_{T_1})}{T_2 - T_1} = \frac{\Delta\varepsilon_T}{\Delta T} \quad (1)$$

where:

- ε_{T_1} = thermal strain of the specimen due to the temperature change from T_0 to T_1
- ε_{T_2} = thermal strain of the specimen due to the temperature change from T_1 to T_2
- ΔT = change in temperature
- $\Delta\varepsilon_T$ = change in thermal strain

The value of CTE is positive for expansion and negative for contraction. For thermal cracking, α is often referred to as coefficient of thermal contraction (CTC) since *contraction* of the pavement layer is the mechanism involved.

Extensive research has been conducted in the United States and Canada since the 1960s on the subject of CTC of AC mixtures. Most of the conclusions on CTC were drawn from laboratory studies using various CTC measurement devices. A comprehensive literature summary of experimental determination of CTC of AC mixtures can be found in Stoffels and Kwanda's study (1995). Test devices include: dilatometer, extensometer, brass frame, push-rod dilatometer, strain gauge, and LVDTs; and AC specimens used were either beam or cylindrical and were subjected to either controlled or uncontrolled rate of cooling.

While experimental determination of CTC produces accurate results, this requires significant resources and efforts compared with testing of asphalt binders and aggregates. Lytton et al. (1993) presented an empirical model to determine the linear CTC of AC mixtures in the solid state (at low temperature) using volumetric CTC of binder in the solid state, volumetric CTC of the aggregate, VMA, and percent volume of aggregate in mixture. This model is currently adopted in the TCMODEL in the MEPDG software. Given that the CTC of binder is not measured for routine mix design, TCMODEL uses a default value of $34.5 \times 10^{-5} / ^\circ\text{C}$ for *all* binders (NCHRP 1-37A 2004). Values of the CTC of AC mixtures reported in the literature range from 1.33 to $3.7 \times 10^{-5} / ^\circ\text{C}$. Figure 1 shows a screen shot of the thermal cracking model interface in the new MEPDG software.

SENSITIVITY STUDY

One pavement section representing major Interstate and US highways in the Northwest region of Indiana was selected in the sensitivity study. This section is

located on Interstate I-65 North-Bound near Rensselaer, Indiana. The original pavement was a JRCPC constructed in 1968. The 10” concrete layer was rubblized in 1994 and overlaid with 13” of hot mix asphalt (HMA). The HMA layer consisted of a base, binder, and surface course, all of which were unmodified AC-20 Marshall mixes.

For this study, all design input values selected resembled those used for the original design of the rubblized section. Thermal cracking inputs (tensile strength and creep compliance) of AC mixtures from this pavement section were available. Climate data from weather stations surrounding the pavement location were used to generate local climate data for thermal cracking prediction. A typical 20-year design life often used for AC pavement design in the US was chosen with no scheduled maintenance or rehabilitation activities. Level 1 inputs representing the highest level in the hierarchy system and providing the highest degree of reliability were selected for thermal cracking, the failure criterion for which was set at 1000 ft/mi. Additional information about the selected pavement section and related data inputs used for the MEPDG software are documented elsewhere (Chehab and Galal 2005).

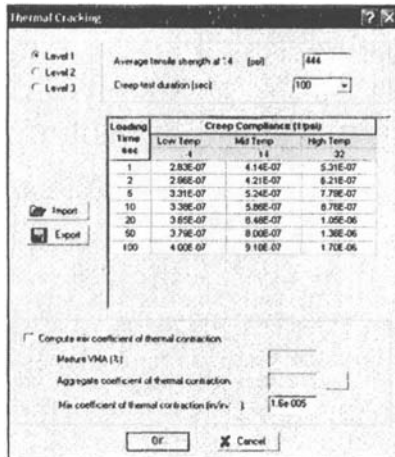


FIG. 1. Screen shot of the MEPDG software interface for thermal cracking

Three AC mixtures were used for studying the sensitivity analysis of CTC on thermal cracking. All design input parameters needed in conducting the MEPDG analysis were kept constant, except for those parameters affecting the thermal cracking prediction, mainly: CTC, binder grade, tensile strength, and creep compliance, as presented in Table 1. The selected mixtures represent commonly used AC mixtures in pavement design and construction: mix 1 – low strength and high ductility, mix 2 – medium strength and medium ductility, mix 3 – high strength and low ductility. The three values of CTC used cover a wide range of typical values for

AC mixtures: low ($1.0 \times 10^{-5} / ^\circ\text{F}$), medium ($1.5 \times 10^{-5} / ^\circ\text{F}$), and high ($2.0 \times 10^{-5} / ^\circ\text{F}$). The units of CTC are expressed in $^\circ\text{F}$ rather than $^\circ\text{C}$ due to input requirements of the MEPDG software.

TABLE 1. Tensile strength and creep compliance of AC mixtures used in the sensitivity study. (Reproduced from MEPDG Appendix HH)

Binder Grade	Creep Compliance, D(t), 1/psi				Tensile Strength, TS, psi
	Loading Time (sec)	Low Temp ($^\circ\text{F}$)	Mid Temp ($^\circ\text{F}$)	High Temp ($^\circ\text{F}$)	Mid Temp ($^\circ\text{F}$)
		-4	14	32	14
AC mixture 1					
AC-5 Pen 120-150 PG 52-28 PG 52-34	1	2.07E-07	2.41E-07	4.27E-07	370
	2	2.21E-07	2.69E-07	4.69E-07	
	5	2.41E-07	2.96E-07	5.52E-07	
	10	2.55E-07	3.24E-07	6.27E-07	
	20	2.69E-07	3.52E-07	7.45E-07	
	50	2.83E-07	3.93E-07	9.45E-07	
	100	3.10E-07	4.07E-07	1.12E-06	
AC mixture 2					
AC-10 Pen 85-100 PG 58-22 PG 58-28	1	2.83E-07	4.14E-07	5.31E-07	444
	2	2.96E-07	4.21E-07	6.21E-07	
	5	3.31E-07	5.24E-07	7.79E-07	
	10	3.38E-07	5.86E-07	8.76E-07	
	20	3.65E-07	6.48E-07	1.05E-06	
	50	3.79E-07	8.00E-07	1.36E-06	
	100	4.00E-07	9.10E-07	1.70E-06	
AC mixture 3					
PG 70-34	1	3.86E-07	5.17E-07	6.21E-07	511
	2	4.41E-07	5.52E-07	7.24E-07	
	5	4.76E-07	6.21E-07	9.38E-07	
	10	5.17E-07	7.10E-07	1.16E-06	
	20	5.65E-07	8.07E-07	1.46E-06	
	50	6.69E-07	9.58E-07	1.99E-06	
	100	7.17E-07	1.12E-06	2.59E-06	

By varying D(t), strength, and CTC, a total of nine software runs were conducted. Predicted crack lengths for each run are plotted in Figure 2. From the results, the following can be stated:

- For mix 1, which is characterized by low strength but high ductility, the crack lengths predicted with different CTC's overlap each other and exceed the design limit in the first winter. Since the pavement fails so quickly regardless of the CTC value, CTC's sensitivity is not significant, probably due to the low strength of the pavement.
- The evidence of CTC's effect on thermal cracking is evident for runs conducted for mix 2, which is characterized by medium strength and ductility. As expected, thermal cracking increases with the increase of CTC. Pavement service life prior to thermal cracking failure shortens by 50% when CTC is increased from low to medium: i.e., by 50%. With a high CTC.

pavement fails approximately at the same time as mix 1 suggesting equivalent effects of low tensile strength and high CTC.

- When the mix is strong and ductile enough, such as for mix 3, the sensitivity of CTC is insignificant. As evidenced in Figure 2, the pavement does not fail within the design life regardless of the value of CTC.

The aforementioned observations suggest that the sensitivity of CTC on thermal cracking is highly material dependent and has to be assessed in the context of other properties such as tensile strength and creep compliance. For the pavement structure in question, most of the thermal cracking occurs within the first five years of service life, as predicted and observed from distress surveys. Consequently, a more detailed analysis of CTC sensitivity is evaluated in the next phase of the study, considering only the first five years of service life for mix 2, conditions where sensitivity of CTC was most evidenced.

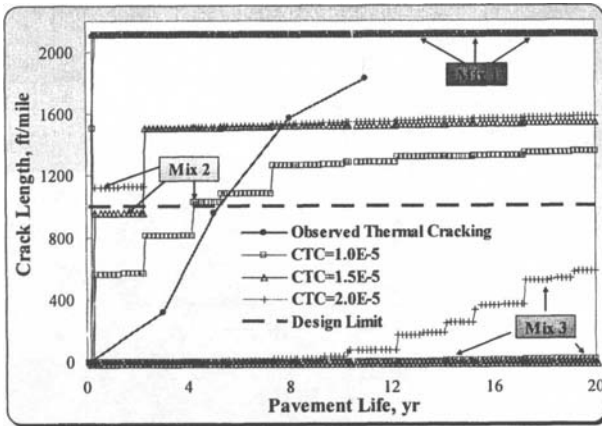


FIG. 2. Crack lengths predicted with different CTCs

In the second phase of the sensitivity study, the value of CTC is incremented at each subsequent run by $0.2 \times 10^{-5} / ^\circ\text{F}$ within the confines of a pre-selected range of values. It was expected that a $0.2 \times 10^{-5} / ^\circ\text{F}$ increment rate would be appropriate to observe any apparent sensitivity trend. The predicted crack lengths from the software runs are plotted in Figure 3. As observed, thermal cracking is very sensitive to the CTC of AC mixture. Thermal cracking failure occurs within: four years for CTC values less than or equal to $1.2 \times 10^{-5} / ^\circ\text{F}$, two years for $1.2 \times 10^{-5} / ^\circ\text{F} < \text{CTC} < 1.6 \times 10^{-5} / ^\circ\text{F}$; and within the first year when CTC is equal to or greater than $1.8 \times 10^{-5} / ^\circ\text{F}$.

Further observations can be made from Figure 4 where crack damage is plotted for different CTC values during the first five years. Crack damage is defined as the ratio in percent between the length of total cracks to the length of pavement section. It is interesting to note that the sensitivity of CTC varies with time; crack growth is mostly linear within the first two years, where a 2% growth in damage occurs for

each increment of CTC. After that, thermal cracking becomes more sensitive to CTC, with the significant increase occurring in the third and fourth years, especially for low values of CTC. Note that for years 3, 4, and 5, the predicted cracking (>28%) is almost same for $CTC \geq 1.4 \times 10^{-5} / ^\circ F$. This observation reveals that the value of CTC will not affect the predicted cracking after thermal stresses induced by temperature drops have been released through a certain amount of thermal cracks. The cumulative crack damage predicted for different CTC's are summarized in Table 2.

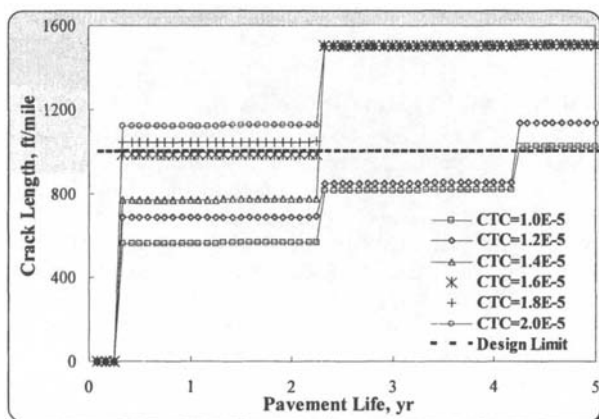


FIG. 3. Crack lengths predicted with different CTCs of AC mixture 2

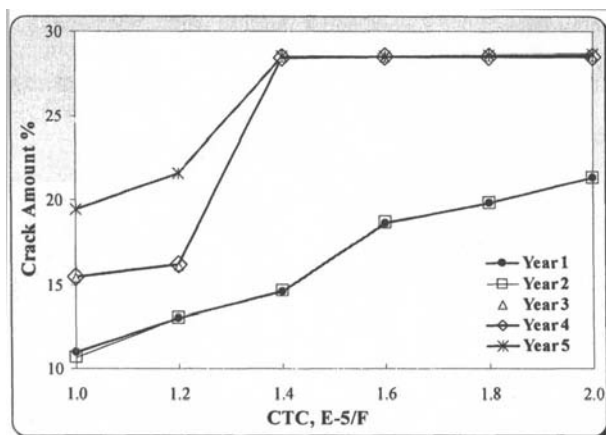


TABLE 2. Cumulative crack damage during first 5 years for mixture 2

Pavement Life, yr	CTC, E ⁻⁵ /°F					
	1.0	1.2	1.4	1.6	1.8	2.0
1	11%	13%	15%	19%	20%	21%
2	11%	13%	15%	19%	20%	21%
3	15%	16%	28%	28%	28%	28%
4	15%	16%	28%	28%	28%	29%
5	19%	22%	29%	29%	29%	29%

CONCLUSTIONS AND RECOMMENDATIONS

With the release of the mechanistic-empirical pavement design guide (MEPDG), attention has been placed on the importance of the coefficient of thermal contraction, CTC. In particular, users of the MEPDG will need to know how critical and sensitive will CTC be in predicting thermal cracking of AC pavements. Using reported values of CTC of AC mixture from literature, the sensitivity of this parameter on thermal cracking was assessed through a case study on one pavement section in Indiana, using numerous MEPDG software runs. Results indicate that the sensitivity of CTC of AC mixture on thermal cracking is material and time dependent. Greatest sensitivity of CTC was observed with mixtures of medium strength and ductility. Investigation of different sites involving diverse environmental conditions and material properties is required to formulate more universal conclusions. Moreover, additional efforts for studying the sensitivity of CTC on thermal cracking must incorporate the tensile strength and creep compliance of the mix since significant interaction exists with CTC in determining the extent of thermal cracking. Finally, a comprehensive sensitivity study will require the consideration of the glass-transition temperature of AC, T_g . Other research (Bahia and Anderson 1993; Jung and Vinson 1994) has shown that T_g significantly affects behavior of asphalt materials at very low temperatures.

During the Strategic Highway Research Program (SHRP), an empirical method was proposed to estimate CTC of an AC mixture from the properties of the mix and its components. While this method has been widely used and has been incorporated in the MEPDG, research (Stoffels and Kwanda 1996; Mehta et al. 1999) has shown the need for more accurate methods to determine the AC CTC. As there are no standardized tests yet, future research for developing new analytical/experimental methods would be highly beneficial.

REFERENCES

1. Bahia, H., and Anderson, D.A. (1993). "Glass transition behavior and physical hardening of asphalt binders." *Journal of Asphalt Paving Technology*, Vol. 62, 93-129.
2. Chehab, G.R. and Kim, Y.R. (2005). "Viscoelastoplastic continuum damage model application to thermal cracking of asphalt concrete." *Journal of Materials in Civil Engineering*, ASCE, In print.
3. Chehab, G.R. and Galal, K. (2005). "The M-E design guide: a case study on HMA overlays over fractured PCC slabs." *Journal of Asphalt Paving Technology*, Vol. 74E.
4. Huang, Y.H. (1993). *Pavement analysis and design*, 1st Ed., Upper Saddle River, New Jersey.
5. Jung, D.H., and Vinson, T.S. (1994). "Low-temperature cracking: test selection." Strategic Highway Research Program, *Research Report SHRP-A-400*, National Research Council, 2101 Constitution Avenue, Washington, DC.
6. Lytton, R.L., Uzan, J., Fernando, E.J., Roque, R., Hiltunen, D., and Stoffels, S.M. (1993). "Development and validation of performance prediction models and specifications for asphalt binders and paving mixes." Strategic Highway Research Program, *Research Report SHRP-A-357*, National Research Council, 2101 Constitution Avenue, Washington, DC.
7. Mehta, Y.A., Stoffels, S.M., and Christensen, D.W. (1999). "Determination of coefficient of thermal contraction of AC using indirect tensile test hardware." *Journal of Asphalt Paving Technology*, Vol. 68, 349-368.
8. "Guide for mechanistic-empirical design of new and rehabilitated pavement structures." (2004). *Final Report NCHRP 1-37A*, ERES Consultants Division, 505 West University Avenue, Champaign, Illinois.
9. Roque, R., Hiltunen, D. R., and Stoffels, S. M. (1993). "Field validation of SHRP asphalt binder and mixture specification tests to control thermal cracking through performance modeling." *Journal of Asphalt Paving Technologists*, Vol. 62, 615-638.
10. Stoffels, S.M. and Kwanda, F.D. (1996). "Determination of the coefficient of thermal contraction of AC using the resistance strain gage technique." *Journal of Asphalt Paving Technology*, Vol. 65, 73-90.
11. Vinson, T.S., Janoo, V.C., and Haas, R.C.G. (1989). "Summary report on low temperature and thermal fatigue cracking." Strategic Highway Research Program, *Research Report SHRP-A-306*, National Research Council, 2101 Constitution Avenue, Washington, DC.

EVALUATION OF MOISTURE SENSITIVITY OF HOT MIX ASPHALT BY FLEXURAL BEAM FATIGUE TEST

Qing Lu¹ and John T. Harvey², P.E., Member, ASCE

ABSTRACT: The research presented in this paper developed a test protocol for using the flexural beam fatigue test to evaluate the moisture sensitivity of hot mix asphalt (HMA). The following test parameters were determined: vacuum intensity and duration for pre-saturating specimens, preconditioning temperature and duration before the fatigue test, and temperature and strain level during the fatigue test. An experiment was designed to include two aggregates, two binders, and one antistripping additive for testing by this procedure. The indirect tensile strength ratio (TSR) test and the Hamburg Wheel Tracking Device (HWTD) test were also performed on the same mixes. Generally, the three test methods did not give consistent results in terms of relative ranking of performance. The flexural beam fatigue test showed potential capability to evaluate moisture sensitivity of HMA, but further refinement is needed.

INTRODUCTION

Moisture damage, which can be understood as the progressive functional deterioration of asphalt mixtures by loss of the adhesive bond between asphalt and aggregate surface and/or loss of cohesion within the binder due to water, has been noticed and studied in the pavement community for over 70 years. It is a complex phenomenon, affected by a variety of factors including material properties, mix composition, traffic loading, and climate characteristics. The most significant symptom of moisture damage is catastrophic failure of pavements, in which the mix disintegrates and aggregates are stripped of asphalt ("stripping"). This type of failure often occurs within a few years after construction. Most research in the literature was targeted at preventing this failure. Moisture may also act in a subtle way, in which stripping is unobservable, but due to the disruption of mix integrity, moisture reduces the performance life by accelerating all distress modes of interest in pavement design, including fatigue cracking, permanent deformation (rutting) and thermal cracking. Less attention has been paid to research in this area.

The indirect tensile strength ratio (TSR) test is currently most widely used to determine the moisture sensitivity of HMA. Several versions of this test exist, such as AASHTO T 283, ASTM D 4867 and CTM 371. These tests all utilize a similar

¹ Graduate Student Researcher, University of California at Berkeley, Institute of Transportation Studies, Pavement Research Center, 1353 S. 46th St., Richmond, CA, 94804-4603, luqing@berkeleyu.edu

² Associate Professor, University of California at Davis, Department of Civil and Environmental Eng., Davis, CA, 95616, jtharvey@ucdavis.edu

conditioning procedure: a partially saturated specimen is subjected to a freeze-thaw cycle and the percentage of strength loss is measured. There are two limitations to this test. First, the conditioning process does not include dynamic loading that is essential in the field and may well contribute to moisture damage in a saturated pavement. A recent survey of the field performance of HMA pavements in California revealed that severe stripping typically occurs in the wheel path, while at the same site much less damage is observed in between the wheel paths or on the shoulder. Second, the TSR test is not performance related test. That is, its result cannot be used in performance models to predict the pavement life.

Dynamic loading is included in a group of loaded wheel rut tests, such as Hamburg Wheel Tracking Device (HWTD) test (Rand 2002), PURWheel (Pan and White 1999), and Asphalt Pavement Analyzer (APA) test (Collins et al. 1997). They apply a repeated steel or pneumatic wheel load on specimens submerged in water and measure the progression of rut depth. This type of test is used as a proof test to determine the premature failure susceptibility of HMA due to a variety of factors, such as weak aggregate structures, inadequate binder stiffness, and moisture damage. However, as with the TSR test, results from the loaded wheel rut tests cannot be directly used in pavement design.

To better determine the moisture sensitivity of a mix in the laboratory, a test method is needed that can better simulate the field loading conditions and for which results can potentially be used in performance prediction. The flexural beam fatigue test holds promise in this area because it measures the properties used in pavement design: stiffness and fatigue damage under repeated loading. Both of these properties are used in most pavement design methods.

The objective of this study is to evaluate the effect of moisture on the fatigue response of HMA and to examine the feasibility of using the fatigue test to determine the moisture sensitivity of HMA. The paper is focused on the development of the test procedure, with some results presented.

EXPERIMENTAL DESIGN

The four-point bending flexural beam fatigue test was selected for this study. The test was performed in the same way as the conventional fatigue test in a controlled-strain mode, which is believed to better replicate the conditions in the field where the deformation of asphalt concrete layers are partly constrained by the underlying structures. This is more rational for thin AC layers overlaid on old pavements, which is a major practice on current US highways. For comparison, both the HWTD test and the TSR test were conducted on the same mixes, following the procedures in the AASHTO T 324-04 test and California CTM 371-03 test, respectively.

Before conducting the test, several parameters needed to be determined: mix design, moisture content and preconditioning temperature and duration of the beam specimens, temperature and strain level during the fatigue test.

Mix Design

A 19-mm nominal maximum medium gradation proposed in Caltrans Standard Specifications was used for all mixes in the experiment. The optimum binder content of each mix was determined by the Hveem mix design procedure.

Two aggregates, W and C, were selected for the experiment. Aggregate W has poor compatibility with asphalt although it has generally performed well in the field, while mixes containing aggregate C showed good moisture resistance in the field. Two binders, AR4000 and PBA-6a, were included in the test. AR4000 binder (AASHTO MP1 designation PG64-16) is an unmodified asphalt widely used in California. PBA-6a is a polymer-modified binder with added elastomeric components (AASHTO MP1 designation PG64-40). PBA-6a binder has been used as one of the design measures to mitigate moisture damage in asphalt concrete pavements in some districts in California. Hydrated lime was used as the anti-stripping additive at a ratio of 1.4% (by dry mass of aggregates). To exclude the confounding effect of the extra fines due to the added lime, the same mass of fines passing the 75- μm sieve was removed from the original aggregates so that the aggregate gradation in the mix remained nearly unchanged. A 2^3 full factorial experimental design was planned, including 2 (aggregates) \times 2 (binders) \times 2 (additive conditions) = 8 mixes. For each mix, four beams were fabricated, two tested in dry condition and the other two tested after moisture conditioning, for a total of 32 beams specimens.

Each beam specimen was 63.5 mm wide, 50.8 mm high and 381.0 mm long, and was cut from slabs compacted by a rolling wheel compactor. The air-void contents in the specimens were controlled between 6% and 8%, which is typical for newly constructed pavements in the field.

Preconditioning of Specimens

Moisture Content

Moisture content may have a significant effect on the test results. In the laboratory, vacuum is applied to accelerate the rate of moisture ingress into specimens. It is necessary to determine an appropriate moisture content, or saturation level, in the specimen and the corresponding vacuum intensity and duration to achieve this moisture content.

The moisture content of specimens in the laboratory should be consistent with the actual level common in the field pavements. To measure the field moisture content is difficult and there are few historical data available. As an approximation in the laboratory, one may assume that the maximum moisture content in the field can be estimated by the amount of moisture entering specimens that are submerged in water. A small-scale experiment was conducted to determine this moisture content. Beam and core specimens with different air-void contents were soaked in a water bath at 25°C and 50°C for about four months and their masses in water were measured periodically. The amount of moisture entering the beam specimens at 25°C at different periods is illustrated in Fig. 1. It can be seen that moisture penetrated into the specimens quickly in the first two weeks, then moved at a much slower rate. An exponential function was fitted to the moisture absorption curves to calculate the ultimate moisture content that would enter the specimens. The ultimate moisture content and the corresponding saturation level in each beam, along with the results from core specimens, are shown in Fig. 2. As can be seen in the figure, the ultimate moisture content is proportional to the air-void content, but the saturation level does not change significantly with the air voids. For specimens soaked in a 25°C water bath, the ultimate saturation level is generally between 40% and 60%.

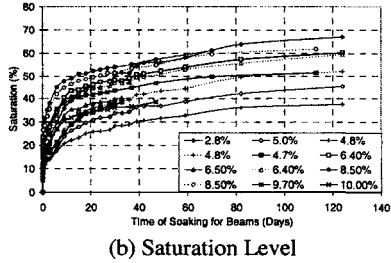
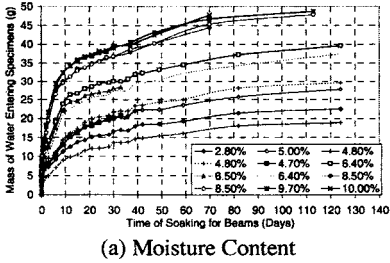


FIG. 1. Moisture absorption curves of beams at different air-void contents

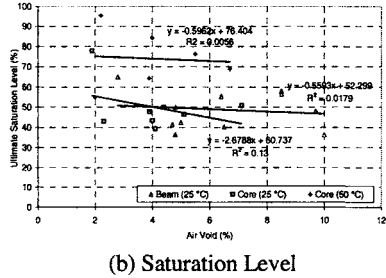
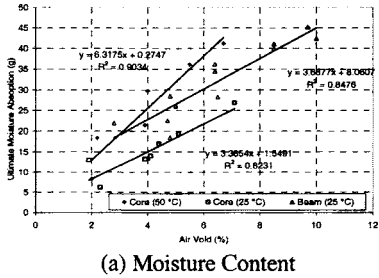


FIG. 2. Estimated ultimate moisture absorption at different air-void contents

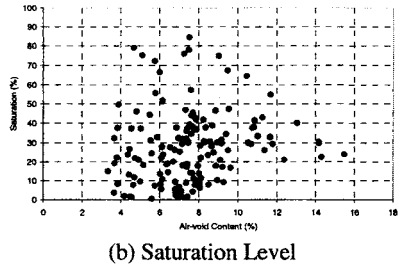
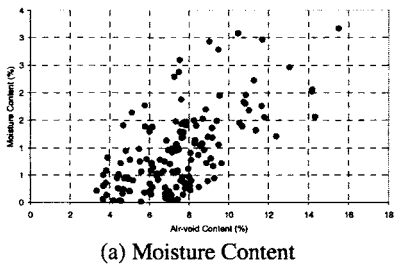


FIG. 3. In-situ moisture absorption in pavements

At the late stage of this study, dry cores were taken from about thirty asphalt pavements in California between June and September, which provided a direct measurement of the in-situ moisture content. Fig. 3 shows the moisture contents and saturation levels of cores obtained from the field. As can be seen, the moisture content of HMA pavements is proportional to its air-void content, while the saturation level has no clear correlation with the air-void content. These findings are consistent with the

laboratory soaking results. Moreover, most mixes in the field had a saturation level less than 50%. Note that most cores were taken in the summer (dry) season when there was little rain (California has distinct dry and wet seasons). It is expected that the in-situ moisture content will become higher in the raining season.

Based upon the above observations, it seemed that it was appropriate to specify a saturation level of about 50%-70% as the high moisture level in the specimens. Because the same air-void content range (6-8%) was specified for all specimens, it would make little difference whether to specify a uniform saturation level or to use a fixed vacuum level and duration during the vacuum saturation process. The latter approach was adopted in the experiment since it is easier to conduct, and it is fair for comparison by subjecting different mixes to the same procedure.

The soaking test showed that it took several months for a specimen to reach a saturation level of 60%. Special equipment was developed to saturate the specimens under vacuum. The relationship between saturation level, vacuum intensity, and duration was explored and it was found that thirty minutes application of 635 mm-Hg vacuum resulted in a saturation level of about 50%-70%.

Preconditioning Temperature and Period

The conditioning temperature and duration of beams before the fatigue test will have significant effect on the test results. To choose the appropriate preconditioning temperature and duration, it is necessary to quantify the effects of different temperature and duration combinations. Eight beams of the same mix (Aggregate W, AR4000 binder without treatment) were tested after different preconditioning combinations of three factors: moisture content (Low, High), preconditioning temperature (25°C, 60°C), and preconditioning period (1 day, 10 days). Another beam was tested in dry to provide a benchmark for the results. All beams were tested at a 200 μ e strain level at 20°C.

An analysis of variance (ANOVA) excluding the interaction terms based on Daniel's half normal plot, using either initial stiffness or fatigue life as the dependent variable, revealed that the preconditioning temperature affected the fatigue properties significantly, while the moisture content and conditioning period had only marginal effect. Here the initial stiffness is defined as the flexural complex modulus after 50 load repetitions and the fatigue life as the load repetitions to 50 percent reduction in stiffness.

For the mix used in this experiment, the fatigue life was reduced to less than 10 percent of the benchmark when the specimen was preconditioned in the 60°C water bath, even for only one day. This is believed to be severe and may not be typical in the field, and furthermore, may mask the difference in fatigue performance of different mixes. Therefore, it is preferred to use 25°C in the preconditioning process. Because the pre-conditioning duration (1 day versus 10 days) has an insignificant effect on the test results, it was decided to precondition the beam specimen for one day to keep the test duration short.

As a summary, the preconditioning process was determined as follows: saturate the specimen at 635 mm-Hg vacuum for 30 minutes and then place it in a 25°C water bath for 24 hours. After preconditioning, the beam was wrapped with Parafilm M[®], a moisture-resistant, thermoplastic flexible plastic sheet, to retain its internal moisture. The mechanical effect of Parafilm M[®] on the test results is negligible due to its high flexibility and thin thickness, so no Parafilm M[®] was applied on dry specimens.

Test Parameters

The normal temperature range used in the beam fatigue test is from 10 to 30°C. At a temperature higher than 30°C, the test is difficult to conduct, and the failure mode may not be fatigue cracking. The temperature of 20°C was chosen in the experiment. This is also supported by the fact that in California, the rainy season is from November to March, when the air temperature is relatively low.

For a typical pavement structure, 400 $\mu\epsilon$ is usually the upper limit of the actual strain level at the bottom of asphalt concrete layer containing the AR4000 binder, while 200 $\mu\epsilon$ is around the average value. Therefore, it was decided to use 200 $\mu\epsilon$ for mixes containing the AR4000 binder and 400 $\mu\epsilon$ for mixes containing the PBA-6a binder since the latter has a much lower stiffness.

TEST RESULTS

The average fatigue test results are summarized in Table 1. The fatigue responses of mixes containing two different binders are quite distinct from each other, as illustrated in Fig. 4. Mixes containing the AR4000 binder showed a continuous decrease of stiffness until the specimen cracked, while mixes containing the PBA-6a binder initially showed a quick reduction in stiffness, but then the stiffness deterioration became trivial after about one million repetitions. For the PBA-6a mixes, an excessive long time would be needed to reach 50 percent stiffness reduction, so the test was terminated at three million repetitions. The extrapolated fatigue lives of the PBA-6a mixes were unreasonably large, so they were discarded in the analysis and not shown in Table 1.

TABLE 1. Average Fatigue Test Results

Mix Type ^a (1)	Moisture Condition (2)	Initial Stiffness (MPa) (3)	Fatigue Life (4)
WAN	DRY	9,657	154,065
	WET	8,141	80,662
WAM	DRY	12,206	220,874
	WET	10,700	308,747
WPN	DRY	1,107	>3,000,000
	WET	938	>3,000,000
WPM	DRY	1,098	>3,000,000
	WET	1,094	>3,000,000
CAN	DRY	9,353	288,791
	WET	7,942	332,275
CAM	DRY	11,498	325,073
	WET	11,830	418,394
CPN	DRY	843	>3,000,000
	WET	793	>3,000,000
CPM	DRY	942	>3,000,000
	WET	957	>3,000,000

^aFirst letter represents aggregate (W, C); second letter represents binder (A-AR4000, P-PBA-6a); third letter represents additive (N-Nil, M-Hydrated Lime)

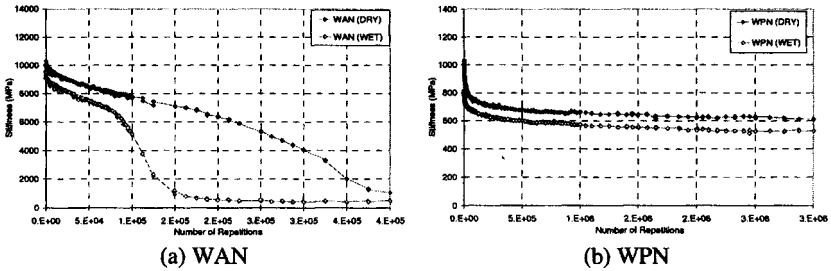


FIG. 4. Stiffness deterioration curves of mixes containing different binders

The following linear model was used to fit the test data:

$$y = \mu + \sum_{i=1}^4 \beta_i X_i + \sum_{j,k=1, k>j}^4 \beta_{jk} X_{jk} + \varepsilon \quad (1)$$

where y is the response variable, μ is the overall mean, β_i and β_{jk} are the parameters to be estimated, X_i is the difference of two indicator functions. Specifically, $X_1 = ind(\text{Aggregate C}) - ind(\text{Aggregate W})$, $X_2 = ind(\text{AR4000}) - ind(\text{PBA-6a})$, $X_3 = ind(\text{Hydrated Lime}) - ind(\text{No Treatment})$, and $X_4 = ind(\text{Dry}) - ind(\text{Wet})$, in which $ind(\cdot)$ is an indicator function, 1 if the level of a factor is equal to the value in the parentheses, 0 otherwise. X_{jk} is the product of X_j and X_k , $X_{jk} = X_j X_k$. ε is a random error term, assumed to have independent normal distribution, $\varepsilon \sim N(0, \sigma^2)$. Third or higher order interaction terms were not included in the model due to their insignificance from a preliminary analysis.

Table 2 shows the model estimation results when the initial stiffness was used as the response variable. It can be seen that the initial stiffness is significantly affected by the binder type, use of additive and moisture condition, but not by aggregate type. Specifically, mixes containing the PBA-6a binder have much lower stiffness than mixes containing the AR4000 binder; adding hydrated lime increases the mix stiffness while moisture generally reduces the stiffness. The reduction in stiffness due to moisture indicates that the cohesion in the binder and/or the adhesion between the binder and the aggregates are disrupted to some extent by moisture. The interactions between moisture condition and aggregate, binder, or additive are all significant. The signs of these interactions indicate that the stiffness reduction due to moisture is more dramatic in the mixes containing aggregate W than in the mixes containing aggregate C, less in the mixes containing PBA-6a binder than in the mixes containing AR4000 binder, and less in the mixes treated with hydrated lime than in the untreated mixes. These results are consistent with field experience that mixes containing the aggregate C, PBA-6a binder, or hydrated lime are more resistant to moisture damage than mixes containing the aggregate W, AR4000 binder, or no treatment.

TABLE 2. Parameter Estimation Using Initial stiffness as the Dependant Variable ($R^2=0.9964$)

Factor (1)	Parameter Estimate (MPa) (2)	t-statistic (3)	P-value (4)
Overall Mean (μ)	5568.7	89.7427	<0.0001
Aggregate (β_1)	-49.0	-0.7902	0.4383
Binder (β_2)	4597.2	74.0855	<0.0001
Treatment (β_3)	721.8	11.6329	<0.0001
Condition (β_4)	269.4	4.3416	0.0003
Aggregate:Binder (β_{12})	38.8	0.6250	0.5387
Aggregate:Treatment (β_{13})	65.0	1.0470	0.3070
Aggregate:Condition (β_{14})	-130.0	-2.0945	0.0485
Binder:Treatment (β_{23})	670.7	10.8080	<0.0001
Binder:Condition (β_{24})	243.3	3.9216	0.0008
Treatment:Condition (β_{34})	-123.8	-1.9958	0.0591

When fatigue life was used as the response variable, the linear model (1) was not applicable because the data for mixes containing the PBA-6a binder were truncated. A direct examination of the fatigue life ratio (FLR) (Table 3), defined as the ratio of fatigue life from a wet specimen to that from the corresponding dry specimen, showed that except the mix WAN, moisture generally extended the fatigue life of mixes containing the AR4000 binder. The relative rank of mixes based upon the FLR is still reasonable. Mix WAN has a FLR about 0.52, much less than that of other mixes, which is consistent with the fact that mix WAN is very sensitive to moisture. The mix containing aggregate C (CAN) has higher FLR than the mix containing aggregate W (WAN), and mixes treated with hydrated lime (WAM and CAM) have higher FLR than untreated mixes (WAN and CAN). The improvement of FLR due to hydrated lime is more significant in the WAN than in CAN because aggregate C is more compatible with asphalt than aggregate W. For mixes containing the PBA-6a binder, a direct examination of the stiffness deterioration curves revealed that except for mix WPN, moisture showed little influence on the stiffness deterioration process of the PBA-6a mixes. For the mix WPN, moisture slightly shifted downward the stiffness deterioration curves (Fig. 4).

Results from the CTM 371 test and the HWTD test are also shown in Table 3. A check of the TSR values revealed the following: (1) mixes containing aggregate C have significantly higher TSR value than mixes containing aggregate W; (2) mixes containing the PBA-6a binder have significantly higher TSR value than mixes containing the AR4000 binder; (3) mixes treated with hydrated lime have significantly higher TSR value than untreated mixes; (4) hydrated lime improves TSR value more in mixes containing aggregate W than in mixes containing aggregate C. These results are generally consistent with the results from the flexural beam fatigue test, especially when the initial stiffness is used as the response variable.

TABLE 3. Normalized Fatigue Test Results and TSR, HWTD Test Results

Mix Type	Stiffness Ratio	Fatigue Life Ratio	TSR (%)	Stripping Inflection Point	Stripping Slope ($\mu\text{m}/\text{pass}$)	Rut Depth After 20,000 Wheel Passes (mm)
(1)	(2)	(3)	(4)	(5)	(6)	(7)
WAN	0.843	0.524	29	13000	0.30	7.2
WAM	0.877	1.398	85	>20000	-	5.3
WPN	0.847	-	47	3950	2.30	42.3
WPM	0.996	-	86	8150	0.45	10.9
CAN	0.849	1.151	52	>20000	-	6.0
CAM	1.029	1.287	91	>20000	-	5.5
CPN	0.941	-	85	5500	3.25	56.4
CPM	1.016	-	100	12000	0.80	13.9

The last column of Table 3 is the rut depth after 20,000 wheel passes in the HWTD test. The values greater than 25 mm were obtained by extrapolation from test data since the test was terminated when the rut depth reached 25 mm. Other response variables, including stripping inflection point and stripping slope, are also included in the table. For the four mixes containing the AR4000 binder, the final rut depths were all very small. In fact, no stripping inflection point had occurred in the test for these mixes except WAN, which showed a very small stripping slope. On the other hand, the four mixes containing PBA-6a binder all showed large rut depth in the test and their stripping inflection points occurred early. These results may be attributed to the fact that the mixes containing PBA-6a binder have much lower stiffness than the mixes containing AR4000 binder, and may not be much related to their moisture sensitivity. Hydrated lime is very effective in reducing the permanent deformation (rut depth) of HMA, especially for the mixes containing the PBA-6a binder.

DISCUSSION

The test results indicate that the controlled strain flexural beam fatigue test has potential use in evaluating moisture sensitivity of asphalt concrete mixtures. The initial stiffness ratio produced a similar trend to that of the TSR test and field experience in terms of the relative ranking of various mixes. The relative ranking of mixes based upon the fatigue life ratio were generally reasonable in terms of aggregate type and treatment type. An unexpected observation from the fatigue test is that for mixes with relatively good field performance the fatigue life was increased instead of decreased when moisture existed in the mixes. Several reasons might contribute to this result. First, the increased specimen flexibility due to moisture, as reflected by the lower initial stiffness, led to a lower stress level in the controlled strain test. Second, since the fatigue life was defined as the number of repetitions to 50 percent reduction of the initial stiffness, a lower initial stiffness also led to a lower final stiffness as the stopping point of the test, which corresponded to more repetitions. Third, for the mixes treated with hydrated lime, lime might further react with asphalt and aggregate and form a stronger bond among the mix components during the preconditioning. Whether the extension of fatigue life due to moisture can occur in the field is unknown. For the same

mix in the pavement, a lower stiffness will lead to a higher stress level under the same wheel load, which may counteract the beneficial effect of moisture. As a retrospect, the preconditioning parameters used in this study, determined on the basis of mix WAN whose properties are very sensitive to moisture influence, tended to be mild – at a mild temperature and for a short duration. Field mixes may be exposed to moisture at high temperatures or for long periods, which may result in different fatigue response. Further studies using a harsher preconditioning procedure (e.g., a higher conditioning temperature or a freeze-thaw cycle) and/or modified definition of fatigue life (e.g., use initial stiffness of dry specimens as reference for calculating the fatigue life of wet specimens) may produce better results.

The fatigue test results are inconsistent with the HWTD test results, except that both tests revealed the beneficial effect of hydrated lime on moisture resistance of HMA. In the HWTD test, the binder type tended to dominate the test results, in which mixes containing the PBA-6a binder generally showed poor performance while mixes containing the AR4000 binder generally showed good performance. This is inconsistent with field experience.

CONCLUSIONS

This study developed a procedure to use the flexural beam fatigue test to evaluate the moisture sensitivity of hot mix asphalt, which focused on the interaction of repeated loading and moisture in a mild condition (mild temperature and short period). Experiment including eight mixes showed that moisture sensitivity evaluated by the fatigue test using the developed procedure was consistent with the field experience and the TSR test, but inconsistent with the HWTD test. For mixes with relatively good performance, extension of fatigue life due to moisture was discovered in this test procedure. Further refinement is needed to include the evaluation of moisture effect in harsher conditions.

ACKNOWLEDGEMENT

This work was undertaken with funding from the California Partnered Pavement Research Program for the California Department of Transportation (Caltrans). The opinions and conclusions expressed in this paper are those of the authors and do not necessarily represent those of Caltrans.

REFERENCES

- Collins, R., Johnson, A., Wu, Y., and Lai, J. (1997). "Evaluation of moisture susceptibility of compacted asphalt mixture by asphalt pavement analyzer." *Compendium of Papers at 76th Annual Meeting*, Transportation Research Board, Washington D. C.
- Pan, C., White, T. (1999). "Conditions for stripping using accelerated testing." *Research Report FHWA/IN/JTRP-97/13*, School of Civil Engineering, Purdue University, West Lafayette, Indiana.
- Rand, D.A. (2002). "HMA moisture sensitivity: past, present & future, TxDOT experiences." *Moisture Damage Symposium*, Western Research Institute, Laramie, Wyoming.

RESPONSE OF AN ASPHALT PAVEMENT MIXTURE UNDER A SLOW MOVING TRUCK

Elie Y. Hajj¹, Peter E. Sebaaly², P.E., Raj V. Siddharthan³, P.E.

ABSTRACT: In this paper, the responses of two different pavement structures (10 and 20 cm HMA layer), were analyzed under the steering, driving and trailer axles of an eighteen-wheeler truck during braking on a 6% downhill grade. The response of the asphalt pavement to the decelerated truck during the braking period was estimated at three different traveling speeds: 64, 32, and 3.2 km/h using the computer code 3D-Moving Load Analysis (3D-MOVE). Significant load redistribution, which occurs between the truck axles under deceleration, has been accounted for in the analysis. The time dependent behavior of the HMA layer as the truck approaches the stopping point is incorporated by using the complex shear modulus and the internal damping as a function of loading frequency. The base course and subgrade layers are treated as linear elastic materials with an internal damping assumed to be 5%. The non-uniform stress distributions at the tire-pavement interface were interpolated from measured contact stress distributions at various speeds made with the Kistler MODULAS Quartz Sensor Array by the Nevada Automotive Test Center (NATC). Braking forces at each tire were included as interface shear stresses with a distribution that was estimated by multiplying the vertical stress distribution by the calculated coefficient of friction between each tire and the pavement surface. The study reveals that rutting in the HMA layer is more prone under the steering single tire while shoving is mainly caused by the dual tandems driving tires.

INTRODUCTION

Permanent Deformation is a major failure mode of flexible pavements, consisting of both rutting and shoving of the hot mix asphalt (HMA) mixture. Typically, a rutting failure alone occurs under traffic loads moving at highway speed, while both rutting

¹ Graduate Research Assistant, Pavements/Materials Program, Department of Civil and Environmental Engineering, University of Nevada, Reno, NV 89557, hajj@unr.nevada.edu.

² Professor and Director, Pavements/Materials Program, Department of Civil and Environmental Engineering, University of Nevada, Reno, NV 89557, Ph.: 775-784-6565, sebaaly@unr.nevada.edu

³ Professor, Department of Civil and Environmental Engineering, University of Nevada, Reno, NV 89557, Ph.: 775-784-1411, Fax: 775-784-1390, siddhart@unr.edu

and shoving failures may occur under traffic loads at intersections. In many instances, the same HMA mixture that has a history of good performance in rutting did not perform well at the intersection. This behavior can be related to two basic phenomena: a) slow and/or stopped traffic at intersections subjects the pavement to higher stresses and b) the HMA mixture behaves weaker as it is subjected to slow moving or stopped vehicular loads.

Rutting may be described as a permanent deformation that occurs in the pavement's wheel path under the action of repeated traffic loads. There are four general types of rutting, each related to a different cause: consolidation, surface wear, plastic flow, and mechanical deformation (Marker 1981; Asphalt Institute). On the other hand, shoving is a common type of distress particularly confined to intersections and braking areas (traffic coming to a stop sign). It is defined as the horizontal displacement of an asphalt mixture and is caused either by shear flow of the mixture or slippage between the layers (Roberts et al. 1996; Kandhal et al. 1998).

The slower loads are not the only reason that intersections are more prone to rutting and shoving. Braking, accelerating and turning movements that occur at intersections impose different stress conditions on the pavement surface layer. The intersection must be able to sustain the interface friction forces caused by braking and accelerating of heavy loaded trucks (e.g., the eighteen-wheeler trucks).

Therefore, because of the difference in the rate of loading and the applied stresses at and near intersections, a different type of HMA mixture may be required at intersections other than the one used on the main line. In order to be able to design and recommend asphalt mixtures for intersections, mixture responses to slow moving loads during braking of an eighteen-wheeler truck have been estimated using the computer code 3D-Moving Load Analysis (3D-MOVE) developed by Siddharthan et al. (1998).

3D-MOVE PROGRAM

The 3D-MOVE program formulation is based on continuum-based "finite-layer" and it is capable of evaluating the response of a layered medium subjected to a moving surface load. The pavement system is characterized through a combination of viscoelastic or elastic horizontal layers with each layer characterized using a set of uniform properties. The finite-layer approach treats each pavement layer as a continuum and uses the Fourier transform technique to handle complex surface loadings in all three directions. This allows the 3D-MOVE model to handle multiple loads, nonuniform tire-pavement normal contact stress distributions and nonuniform interface shear stresses caused by braking. In addition, rate-dependent material properties (viscoelastic) can be accommodated, thus pavement response as a function of vehicle speed can be studied (Siddharthan et al. 1998).

A detailed verification of this approach using existing analytical solutions (ELSYM5) and laboratory test results has shown that the 3D-Move program is capable of simulating correctly the static circular loads applied to a layered system (Siddharthan et al. 1998). In addition, the 3D-Move also has undergone field verification in which responses of two full-scale road tests were used to validate the application of the program (Siddharthan et al. 2002).

LOAD DISTRIBUTION DURING BRAKING OF AN 18-WHEELER TRUCK

Braking decelerates the vehicle, which causes load to transfer to the front of the vehicle. The resulting axle load can be higher or lower than the initial static load, depending on the location of the axle. Fig. 1 shows the major forces acting on an eighteen-wheeler tractor-semitrailer during braking on a downward sloping pavement. Since Brakes are the primary source of braking deceleration, the aerodynamic drag and rolling resistance are neglected in this study. The various axles include: the tractor steering axle, the tractor tandem axle (i.e. driving axle), and the semitrailer tandem axle (i.e. trailer axle). In this study, the tandem axles of the tractor and the semitrailer are considered without equalization, implying that an interaxle load transfer will take place between the rear and the front axle of the tandem group during the braking period of the truck (Wong 1993).

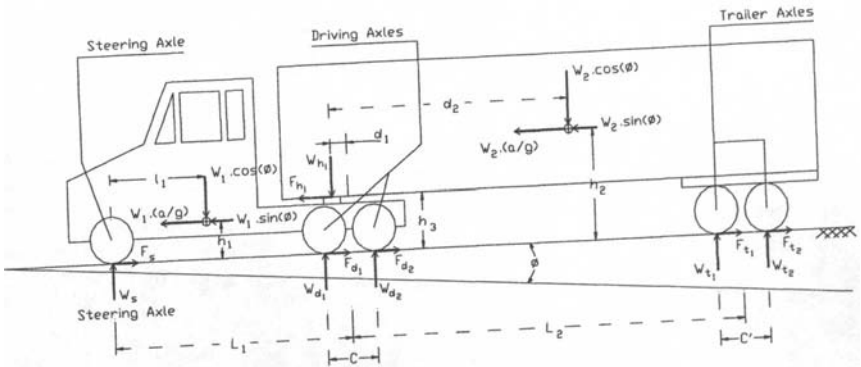


FIG. 1 Forces acting on a tractor-semitrailer during braking on a downward slope

Here W_{h_i} and F_{h_i} are respectively the vertical and horizontal loads at the tractor-semitrailer articulation; “ a ” is the linear deceleration of the truck along the longitudinal axis; g is the deceleration due to gravity; W_1 and W_2 are respectively the tractor and semitrailer total weights; and ϕ is the angle of the slope with the horizontal. W_s , W_{d1} , W_{d2} , W_{t1} and W_{t2} , are the tires normal loads. F_s , F_{d1} , F_{d2} , F_{t1} and F_{t2} , are the braking forces that originate from the brake system and developed on the tire-road interface.

In order to calculate the normal load on each axle, the tractor and the semitrailer are considered as free bodies separately and combined. The vertical, horizontal, and moment equilibrium equations for the tractor, semitrailer unit, and tractor-semitrailer combination can be written as a function of truck loads and geometry (Hajj 2005).

The extent to which vertical load is transferred during braking from the rear tandem tires to the front tandem tires is called the dynamic load transfer coefficient, α and defined as follows (Gillespie and Balderas 1987):

$$\alpha = \frac{W_{t_1} - W_{t_2}}{2(F_{t_1} + F_{t_2})} = \frac{W_{d_1} - W_{d_2}}{2(F_{d_1} + F_{d_2})} \quad (1)$$

The load transfer coefficient has a value of 0.0 when the loads on the front and rear tandem tires are equal (i.e. $W_{t_1} = W_{t_2}$; $W_{d_1} = W_{d_2}$).

By solving the system of equilibrium equations, the normal loads on the various axles during braking on a downward slope can be expressed as a function of W_1 , W_2 , a , ϕ , braking forces, and truck geometry. The full formulation and solutions are presented by Hajj (2005).

The dynamic normal loads on the various axles of an eighteen-wheeler truck were verified against the National Highway Traffic Safety Administration (NHTSA) data (Gillespie and Balderas 1987) for the case of a leveled road (slope, $\phi = 0$). The calculated dynamic normal loads and friction utilizations (ratio of the longitudinal force to the vertical load) on each axle developed in this study matched very well with the ones generated by the NHTSA study. Based on the comparison, it was concluded that the force equations developed in this study can be used to predict the load distributions on an eighteen-wheeler tractor-semitrailer vehicle on sloped and leveled roads.

TIRE LOADS DISTRIBUTION DURING A DOWNWARD BRAKING

The dimensional parameters used to describe the vehicle in this analysis are summarized in Table 1. Axle and group spacings are chosen according to ASTM E1572-93 standard (2001). The weight limits on each axle satisfy the Nevada Department of Transportation (NDOT) legal load limits.

The Goodyear G159A 295/75R22.5 with a radius of 52 cm was assumed to be used at all positions on the tractor and the semitrailer. Tire loads distribution were determined for an eighteen-wheeler braking on a 6% downward sloping pavement (slope angle, $\phi = 4^\circ$).

A constant deceleration of 0.54g is used in this study. This deceleration is the rate that is required for a truck running at 64 km/h to come to a complete stop in a distance of 30 meters. Resulting vertical and longitudinal loads on all truck tires are shown in Table 2.

It may be noted that the braking phenomenon resulted in a vertical load on the steering axle (37.7 kN/tire) exceeding the allowable tire load (27 kN/tire) by about 40 percent, whereas the vertical load on the rear tire (12.7 kN/tire) of the trailer-tandem axle configuration was 33 percent lower than the corresponding allowable tire load (19 kN/tire).

Table 1. Summary of Tractor and Semitrailer Sizes and Weights

Tractor Properties	
Center of gravity height, h_1 (m)	0.82
Center of gravity to steering axle distance, l_1 (m)	2.15
Wheelbase distance, L_1 (m)	5.70
Tandem axles spacing, c (m)	1.20
Tractor total weight, W_1 (kN)	71.0
Static steering axle load, W_s (kN)	54.0
Static driving axle load, W_d (kN)	152.0
Semitrailer Properties	
Center of gravity height, h_2 (m)	1.93
Center of gravity to front articulation distance, d_2 (m)	5.20
Wheelbase distance, L_2 (m)	9.40
Tandem axles spacing, c' (m)	1.20
Semitrailer total weight (fully loaded), W_2 (kN)	285.0
Static trailer axle load, W_t (kN)	152.0
General Properties	
Articulation height, h_3 (m)	1.25
articulation offset, d_1 (m)	39.0
Vehicle total Weight, W (kN)	356.0

Table 2. Vertical and Longitudinal Load Distribution during Braking at 0.54g

Tractor-Semitrailer Axles (1)	Vertical Load/ Tire (kN) (2)	Longitudinal Load/ Tire (kN) (3)	Friction Utilization, μ (4)	
Steering	37.7	9.6	0.255	
Driving	Front Axle	22.8	13.2	0.579
	Rear Axle	14.9	13.2	0.888
Trailer	Front Axle	19.5	11.4	0.583
	Rear Axle	12.7	11.4	0.896

CONTACT STRESS DISTRIBUTIONS

Numerous previous studies (Sebaaly 1992; de Beer and Fisher 1997; Myers et al. 1999) showed that the stress distribution of the tire-pavement interface is not uniform, and influences the HMA pavement resistance to rutting and fatigue failures (de Beer and Fisher 1997; Weissman 1999; Monismith et al. 2000).

In the last decade, a series of sophisticated measuring systems have been developed to measure the stress distribution at the tire-pavement interface. This study utilized measurements made with the Kistler MODULAS Quartz Sensor Array by the Nevada

Automotive Test Center (NATC). The device measures the vertical stress as the tire moves over a measuring pad. The loading of the MODULAS sensors was accomplished by driving a truck with a single trailer at a preset speed. The test tire was mounted on the trailer. Fig. 2 shows the vertical contact stress distribution reported by NATC for a Goodyear G159A 295/75R22.5 tire subjected to a 25 kN load and 827 kPa inflation pressure, and rolling over the measuring device at 36 km/h. Note that the maximum measured vertical stress of 1320 kPa is about 60 percent higher than the tire inflation pressure. The Kistler device does not measure the horizontal interface shear stresses.

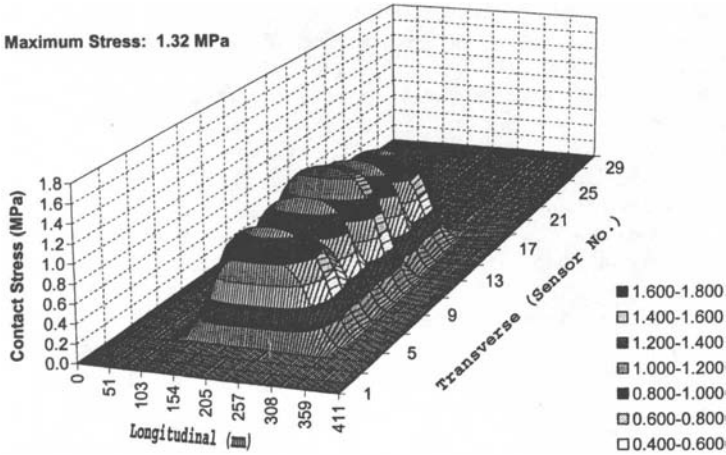


FIG. 2 Vertical contact stress distribution for a Goodyear G159A 295/75R22.5 tire subjected to a 25 kN load and 827 kPa pressure at 32 km/h.

This study used the stress distributions under the Goodyear G159A 295/75R22.5 tire measured by the Kistler device, for an inflation pressure of 827 kPa, and subjected to 36 kN, 31 kN, 25 kN, and 4.45-kN loads moving at 64, 32 and 3.2 km/h.

Since the 3D-MOVE program can only simulate moving loads at a constant speed, the response of the asphalt pavement to the decelerated truck during the braking period was estimated at three different speeds: 64, 32, and 3.2 km/h. The truck was assumed to be rolling at a speed of 64 km/h before it starts braking as it approaches the intersection. The brake-free rolling speed of 64 km/h is more typical of a truck taking an exit from a freeway and coming to a stop light, or a truck coming to an intersection on a city street in urbanized areas.

The contact stress distributions at the tire-pavement interface for each of the vertical loads corresponding to the truck braking on a 6% downward grade have been interpolated from the measured contact pressure distributions at various speeds (64, 32 and 3.2 km/h). Horizontal braking forces were included in the analysis as interface shear stresses in the longitudinal direction that were estimated by

multiplying the predicted nonuniform vertical stress distribution by the coefficient of friction utilization (Table 2) between each tire and the pavement.

MATERIAL PROPERTIES CHARACTERIZATION

The frequency-dependent properties of the HMA layer were used to characterize the rate dependent behavior of the HMA mixture under the slow moving truck. The HMA layer analyzed in this research consisted of a NDOT type 2C dense graded mixture manufactured with a PG76-22NV binder. This type of mixture is commonly used in southern Nevada and is fully described by Hajj (2005). The NDOT type 2C mix has shown excellent rutting resistance under normal highway traffic while its resistance to shoving and rutting at intersections under Las Vegas hot environment has been questionable.

The shear frequency sweep at constant height (FSCH) test was used to measure the mixture's stiffness as a function of the frequency at a temperature of 50°C in accordance with AASHTO T320-03 (2004) procedure. The test specimen has a diameter of 150 mm and a height of 50 mm and compacted to 7% air voids. The shear frequency sweep test is performed by applying a repeated sinusoidal shear strain of 0.0001 mm/mm (0.01 percent) to the specimen at each of the following frequencies and in the following order: 10, 5, 2, 1, 0.5, 0.2, 0.1, 0.05, 0.02, and 0.01 Hz.

The variation in the complex shear modulus of the HMA mixture at 50°C as a function of the loading frequency is shown in Fig. 3. The data shows that the shear modulus of the HMA mixture increases with an increase in loading frequency.

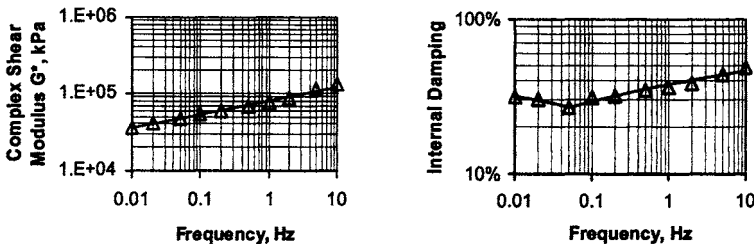


FIG. 3 Mixture stiffness and internal damping determined by the FSCH at 50°C.

The internal damping for the HMA layer is estimated as a function of the loading frequency as shown in Fig. 3. The internal damping of the HMA material is included in the analysis by writing the modulus in its complex form as follows (Rosset 1980; Sousa and Monismith 1987):

$$G^* = G(1 + 2i\zeta_{AC}) = G_1 + iG_2 \quad (2)$$

in which G^* = complex dynamic shear modulus; and ζ_{AC} = measure of internal damping of the HMA, and G_1 and G_2 = real and imaginary shear modulus components, respectively. $|G^*|$, G_1 and G_2 are experimentally determined by the FSCH test as a function of loading frequency, and are subsequently used to calculate ζ_{AC} .

The base course and subgrade layers are treated in this study as linear elastic materials with a shear modulus of 8.6×10^4 kPa and 2.5×10^4 kPa, respectively. The internal damping of the unbound layers is assumed to be 5%. The Poisson's ratio was assumed to be 0.4 for all three layers. The physical material properties of the base and subgrade are summarized in Table 3. Two pavement structures were used in the analysis with different HMA layer thicknesses (10 cm and 20 cm). The thickness of the base layer was kept constant since the primary focus was to study rutting and shoving in the HMA layer. For simplicity, the pavement structure is called "Thin" for the 10 cm HMA layer, and "Thick" for the 20 cm HMA layer.

Table 3 Properties of Pavement Layers

Layer (1)	Thickness (m) (2)	Unit Weight, (kN/m ³) (3)	Shear Modulus, (kPa) (4)	Damping Ratio (5)	Poisson's ratio, ν (6)
HMA	0.1 & 0.2	23.8	Variable	Variable	0.40
Base	0.2	18.0	8.6×10^4	5.0%	0.40
Subgrade	6.0	17.0	2.5×10^4	5.0%	0.40

STRUCTURAL ANALYSIS

The research analyzed the two pavement structures; thin (HMA, 10 cm) and thick (HMA, 20 cm) subjected to a tractor-semitrailer combination (Fig. 1) moving on a 6% downhill with and without braking. The steering axle consisted of a single axle configuration with single tire, whereas the driving and trailer axles consisted of a tandem axle configuration with dual tires. Table 1 and 2 show the axle loads used in the analysis.

The longitudinal direction X represents the travel direction, Y the transverse direction, and Z the vertical direction measured from the top surface of the pavement. Because of the symmetry about the longitudinal centerline of the truck, only one-half of the vehicle was modeled. Fig. 4 shows a pavement layer system (infinite in the horizontal direction) subjected to loads from a tractor-semitrailer. Pavement responses such as stresses, strains, and displacements were computed as a function of time. As the truck rolls over, the pavement response history will consist of a loading, unloading, and a rest period that are a function of the truck speed, tire load configuration, and pavement structure.

Epps et al. (1999) have correlated HMA rutting to shear stress and shear strain in the HMA layer. Additionally, Monismith et al. (2000) demonstrated that the accumulation of permanent deformation in the HMA layer is very sensitive to the

layer's resistance to shape distortion (i.e. shear) and relatively insensitive to volume change. Consequently, the parameter used in this study for the estimation of rutting is the shear strain component γ_{yz} which acts in the transverse YZ-plane perpendicular to the travel direction. The shear strain γ_{xz} that acts in the longitudinal XZ-plane is used for shoving estimation (Hajj 2005).

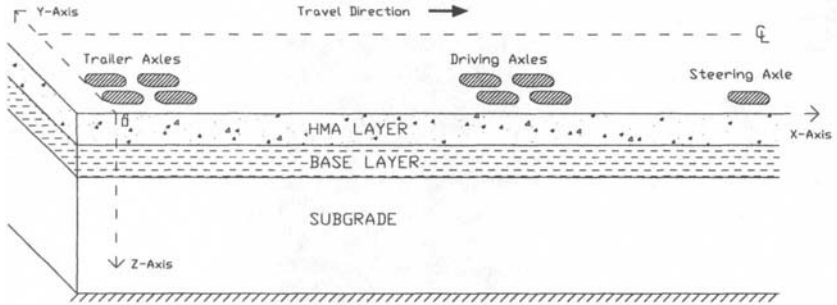


FIG. 4 Axle configuration used in the 3D-Move program.

The locations at which to compute pavement responses are inputted to the program 3D-Move. A total of 90 output locations were included in this study. These locations were distributed within and outside the loaded areas, forming a grid in the plane parallel to the transverse YZ-plane. Since this study is only interested in the rutting and shoving developed in the HMA layer, only the responses within the HMA layer were determined.

Though the program can compute the shear strains at every output location as a function of loading time, only the maximum shear strains developed within the thin and thick HMA layers are presented in this paper and are summarized in Fig. 5 and 6 for the steering, driving and trailer tires configurations during braking and free rolling at various speeds. It should be mentioned that the presented maximum shear strains do not occur at the same time.

As seen in Fig. 5, the transverse shear strain γ_{yz} , in both thin and thick HMA layers, starts from zero at the pavement surface (since shear stress $\tau_{yz} = 0$ at surface) and increase with depth to reach a maximum value at a depth between 6 and 12 mm from the top of the surface. As a result of the braking eighteen-wheeler truck, the maximum transverse shear strain $(\gamma_{yz})_{max}$ developed in the HMA layer occurs under the steering tire at 3.2 km/h. In this case, maximum shear strains $(\gamma_{yz})_{max}$ of 4553 microns and 4503 microns were computed at a depth ratio of 0.06 in the thin and thick HMA layers, respectively. The depth ratio of 0.06 corresponds to the depths of 0.6 and 1.2 cm from the top of the thin and thick HMA layers surface, respectively. Additionally, as was expected the transverse shear strain (γ_{yz}) at various depth was higher in the thin HMA layer when compared to the transverse shear strain at the same depth of the thick HMA layer.

On the other hand, Fig. 6 shows that the longitudinal shear strain γ_{xz} starts from zero only under free rolling tires (no braking) where interface shear stresses τ_{xz} are zero.

As a result of braking, the maximum longitudinal shear strain $(\gamma_{xz})_{max}$ was at the surface and at a traveling speed of 3.2 km/h. The computed $(\gamma_{xz})_{max}$ was about 4250 microns and 11500 microns under the steering tire and the driving tires, respectively. It should be noted that the maximum longitudinal shear strain $(\gamma_{xz})_{max}$ at the pavement surface is the same for both thin and thick pavements due to the fact that the same interface shear stresses (same braking forces) are applied in both cases. Additionally, Fig. 6 shows that under the free rolling eighteen-wheeler truck, the maximum longitudinal shear strain $(\gamma_{xz})_{max}$ in both thin and thick HMA layers occurs at a depth of 5 cm from the top surface.

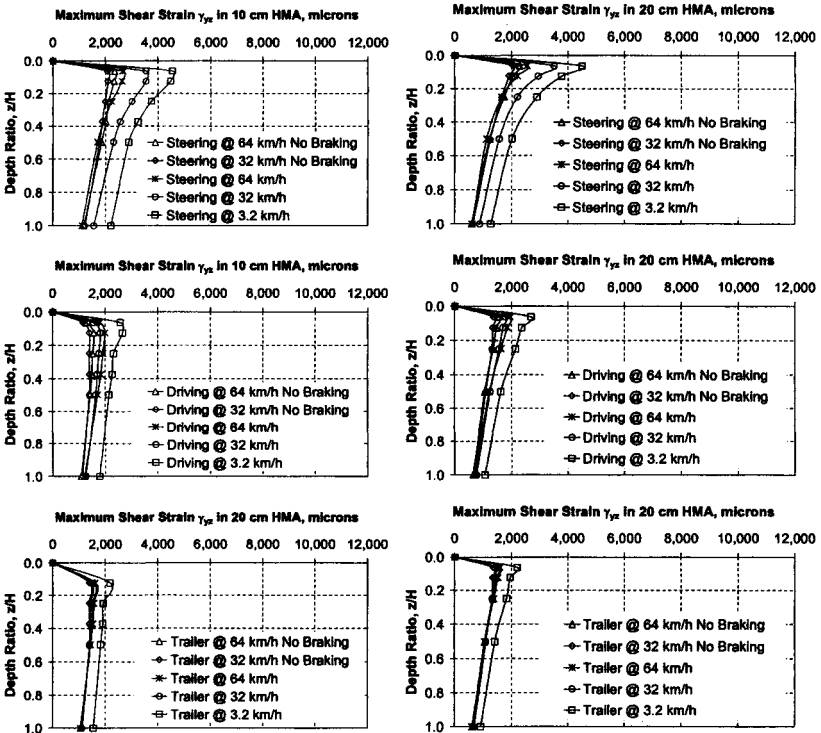


FIG. 5 Distribution of maximum shear strain $(\gamma_{yz})_{max}$ in HMA layer under the eighteen-wheeler truck - Rutting.

CONCLUSION

The calculated pavement responses show that the HMA layer will be subjected to the highest shear strains when the truck is braking while traveling at 3.2 km/h. This

result was expected since asphalt material has a higher resistance to rapidly applied loads compared to slowly applied loads. Additionally, under the braking truck at slow speed (3.2 km/h), it was found that rutting is more prone under the steering single tire while shoving is mainly caused by the dual tandems driving tires. This result could be explained by the fact that under the braking truck, the vertical load on the steering single tire is about 65% greater than the vertical load on the front tire of the driving axles, resulting in higher strains in the transverse direction under the steering axle. On the other hand, the longitudinal braking force applied on the tire of the dual tandem driving axles was about 37% greater than the longitudinal braking force on the steering tire. A direct result of this load redistribution leads to a higher shear strain in the longitudinal direction in the pavement layer.

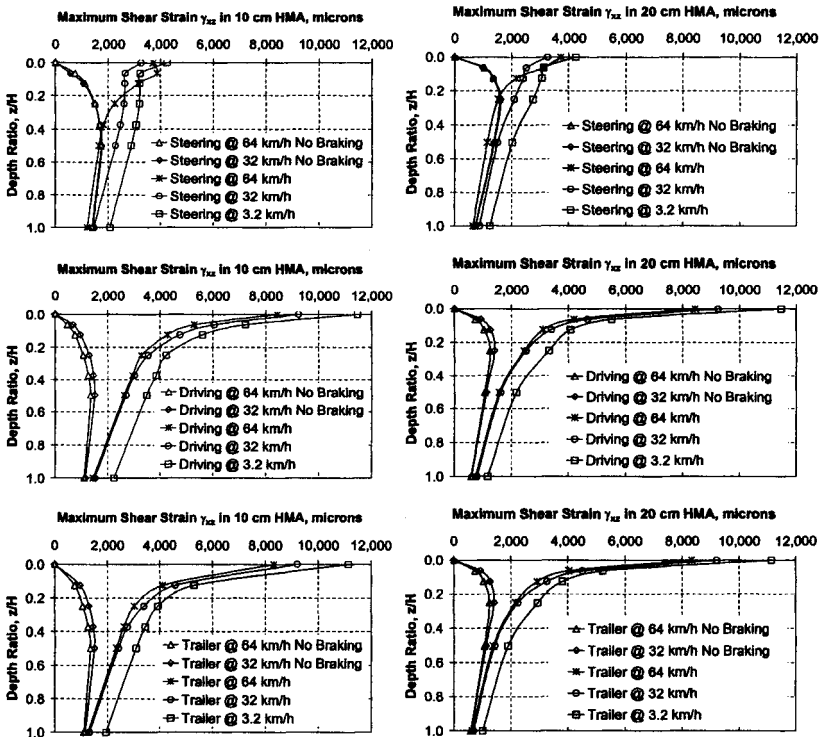


FIG. 6 Distribution of maximum shear strain ($\gamma_{xz})_{max}$ in HMA layer under the eighteen-wheeler truck - Shoving.

Furthermore, the maximum transverse shear strain ($\gamma_{yz})_{max}$ under the braking steering tire traveling at 3.2 km/h was higher by about 93% (thin HMA) and 97% (thick HMA) when compared to the maximum strain developed under the free rolling steering tire at 64 km/h. Additionally the maximum longitudinal shear strain ($\gamma_{xz})_{max}$

under the braking driving and trailer axles was significantly higher than the longitudinal shear strains developed under the free rolling tires.

Therefore, during the braking period, the HMA mixture should be capable to, first, resist transverse shear strains (rutting parameter) that are about double the strains developed in the same HMA layer but away from intersection (no braking), and second, to resist the longitudinal shear strains (shoving parameter) that are of the same order or higher than the transverse shear strains developed during braking.

REFERENCES

- Asphalt Institute. "High performance hot mix asphalt intersection strategy." Executive Offices and Research Center, Lexington, Kentucky.
- Annual Book of ASTM Standards (2001). "Classifying highway vehicles from known axle count and Spacing." *American Society for Testing and Materials*, Method E1572-93, Vol. 04-03.
- De Beer, M., and Fisher, C. (1997). "Contact stresses of pneumatic tires measured with the vehicle-road surface pressure transducer array (VRSPTA) system for the University of California at Berkeley (UCB) and the Nevada automotive test center (NATC)." *CSIR Report CR-97/053*, Council for Sc. and Ind. Res., Pretoria, South Africa.
- Epps, J. A., Leahy, R. B., Mitchell, T., Ashmore, C., Seeds, S., Alavi, S., and Monismith, C. L. (1999). "Westrack - the road to performance-related specifications." *International Conference on Accelerated Pavement Testing, Reno, Nevada*.
- Gillespie, T. D., and Balderas L. (1987). "An analytical comparison of the dynamic performance of a European heavy vehicle and a generic U.S. heavy vehicle." *Research Report UMTRI-87-17*, Univ. of Michigan Transp. Res. Inst.
- Hajj, E. Y. (2005). "Hot mix asphalt mixtures for Nevada's intersections." Ph.D. Dissertation, UNR, Reno.
- Kandhal, P. S., Mallick, R. B., and Brown E. R. (1998). "Hot mix asphalt for intersections in hot climates." National Center for Asphalt Technology, NATC Report No. 98-6, Auburn University, Alabama.
- Marker, V. (1981). "Problems with asphalt pavements." *Presented at the Asphalt State-of-the-Art Conference*, Woodbridge, NJ, U.S.
- Monismith, C. L., Harvey, J. T., Long, F., Weissman, S. (2000). "Tests to evaluate the stiffness and permanent deformation characteristics of asphalt/binder-aggregate mixes - a critical discussion." *Technical Memorandum TM-UCB-PRC-2000-1*, Pavement Research Center, CAL/APT Prog., Inst. of Trans. Studies, Univ. of Calif., Berkeley.
- Myers, L., Roque, R., Ruth, B., and Drakos, C. (1999). "Measurement of contact stresses for different truck tire types to evaluate their influence on near-surface cracking and rutting." *Trans. Res. Rec.*, Transportation Research Board, Washington, D.C., Vol. 1655, 175-184.

- Roberts, F. L., Kandhal, P. S., Brown, E. R., Lee, D. Y., and Kennedy, T. W. (1996). "Hot mix asphalt materials, mixture design, and construction." Second Edition. NAPA Education Foundation, Lanham, Maryland.
- Rosset, J. M. (1980). "Dynamic and damping coefficients of foundations." *Proc., ASCE National Convention on Dynamic Response of Pile Foundations: Analytical Aspects*, M. W. O'Neal and k. Dobry, eds., ASCE, New York, 1-30.
- Sebaaly, P. E. (1992). "Dynamic forces on pavements: summary of tire testing data." *Rep. on FHWA Project DTFH 61-90-C-00084*.
- Siddharthan, R. V., Yao, J., and Sebaaly, P. E. (1998). "Pavement strain from moving dynamic 3D load distribution." *J. Trans. Engrg*, ASCE, 124(6), 557-566.
- Siddharthan, R. V., Krishnamenon, N., El-Mously, M., and Sebaaly, P. E. (2002). "Validation of a pavement response model using full-scale field tests." *Inter. J. of Pav. Engrg*, Vol. 3 (2), 85-93.
- Sousa, J. B., and Monismith, C. L. (1987). "Dynamic response of paving materials." *Trans. Res. Rec.*, Transportation Research Board, Washington, D.C., Vol. 1136, 57-68.
- Standard Specifications for Transportation Materials and Methods of Sampling and Testing (2004). "Standard method of test for determining the permanent shear and stiffness of asphalt mixtures using the superpave shear tester (SST)." *American Association of State Highway and Transportation Officials*, T320-03, 24th edition.
- Weissman, S. L. (1999). "Influence of tire-pavement contact stress distribution on development of distress mechanisms in pavements." *Trans. Res. Rec.*, Transportation Research Board, Washington, D.C., Vol. 1655, 161-167.
- Wong, J. Y. (1993). "Theory of ground vehicles." Second Edition Textbook, ISBN 0-471-52496-4, 1993. Dept. of Mech. and Aerospace Engrg., Carleton University, Ottawa, Canada.

Subject Index

Page number refers to the first page of paper

- Aggregates, 12, 21
- Aging, 103
- Algorithms, 61
- Anisotropy, 44
- Asphalt concrete, 29, 53, 61
- Asphalt pavements, 44, 134
- Asphalts, 1, 12, 21, 73, 83, 95, 124
- Beams, 124
- Case reports, 115
- Coefficients, 115
- Compression, 21
- Computer models, 53
- Constitutive models, 61
- Cracking, 115
- Creep, 115
- Cyclic loads, 53
- Damage, 61, 83
- Deflection, 83
- Deformation, 44, 95, 134
- Discrete elements, 1
- Energy dissipation, 83
- Fatigue, 29, 83, 103, 124
- Finite element method, 21
- Finite elements, 12, 44, 53
- Fractures, 103
- Heterogeneity, 29
- Intersections, 134
- Laboratory tests, 95
- Lateral pressure, 95
- Micromechanics, 1, 12, 21
- Microstructure, 21, 29, 44
- Mixtures, 1, 12, 21, 44, 73, 95, 103, 124, 134
- Pavement design, 115
- Pavements, 53, 61, 103, 124
- Plasticity, 53
- Radiography, 29
- Rheological properties, 73
- Sand, 95
- Shear stress, 134
- Simulation, 1
- Stiffness, 73, 83
- Stress distribution, 29
- Stripping, 124
- Temperature effects, 21
- Tensile strength, 115, 124
- Thermal factors, 115
- Triaxial tests, 95
- Trucks, 134
- Viscoelasticity, 12, 61, 73

This page intentionally left blank

Author Index

Page number refers to the first page of paper

- Abbas, A. R., 1
- Chehab, Ghassan R., 115
Chowdary, Venkaiah, 95
Cleveland, Gregory, 103
- Dai, Qingli, 12, 21
Dessouky, Samer H., 44
- Glover, Charles, 103
Gurung, Bardan, 21
- Hajj, Elie Y., 134
Harvey, John T., 124
- Jung, Sung Hoon, 103
- Krishnan, J. Murali, 95
- Liu, Xueyan, 53
Lu, Qing, 124
Lytton, Robert L., 103
- Martin, Amy Epps, 103
- Masad, Eyad A., 1, 44
- Panneerselvam, Dinesh, 61
Panoskaltis, Vassilis P., 61
Papagiannakis, A. T., 1
Pronk, Adriaan C., 73, 83
- Rengaraju, V. R., 95
- Sadd, Martin H., 12
Scarpas, Tom, 53
Sebaaly, Peter E., 134
Siddharthan, Raj V., 134
Stoffels, Shelley M., 115
Swart, Edwin, 53
Tumay, Mehment T., 29
- Walubita, Lubinda F., 103
Wang, Linbing, 29
- Yin, Hao, 115
You, Zhanping, 12, 21
- Zhang, Bing, 29